INFRARED ELECTRO-THERMO-OPTICAL DEVICES BASED ON THE PHASE TRANSITION OF VANADIUM DIOXIDE

by

Noraica Dávila Meléndez

A DISSERTATION

Submitted to
Michigan State University
in partial fulfillment of the requirements
for the degree of

Electrical Engineering - Doctor of Philosophy

2015

ABSTRACT

INFRARED ELECTRO-THERMO-OPTICAL DEVICES BASED ON THE PHASE TRANSITION OF VANADIUM DIOXIDE

by

Noraica Dávila Meléndez

In this work, electro-thermo-optical devices were developed for near-infrared (NIR) wavelengths by exploiting the optical properties of vanadium dioxide (VO_2). VO_2 undergoes into an insulator-to-metal transition (IMT) in which its optical, electrical, and structural properties change abruptly as a function of its temperature. The changes in these properties show hysteretic behavior.

Sol-gel deposition process was investigated for growing VO_2 thin films on SiO_2 and Si/SiO_2 substrates. Its composition and crystallization were characterized by X-ray diffraction and Raman spectroscopy. Atomic force microscopy and a 3-D surface contact profilometer were used to analyze the surface topography of the films. These thin films were compared with VO_2 thin films deposited by pulsed laser deposited (PLD). VO_2 thin films deposited by PLD were used to develop the devices presented in this work.

In the present work, the IMT is induced thermally, using photo- or electro-thermal techniques. Two devices were developed: 1) a NIR image projector and 2) a fully electronic variable optical attenuator (VOA) to operate in the NIR region. The first device uses the inherent hysteresis in the optical properties of VO_2 across its phase transition, which allowed for the programming of patterns onto the VO_2 thin film. The second device emerged from the optical transition in VO_2, in which the electro-optical changes in the film were induced electro-thermally (i.e. a "thermo-electro-optical device"). The strong correlation between the electrical and optical properties in VO_2 enabled the implementation of a self-sensing technique, which reduced the optical hysteretic behavior and simplified the modeling and control of the attenuation.

To those who inspired or supported me,
but will not read it.

ACKNOWLEDGMENTS

I want to thank to my thesis advisor Nelson Sepúlveda for accepting me in his group, his help, support and guidance during these years. I enjoyed and learned a lot working in his group. My committee members: Tim Hogan for his technical support, assistance and thoughtful discussions about experiments and material characterization techniques; Andre Lee for all his help with the sol-gel deposition process development, recommendations and helpful insights; Prem Chahal for thougful discussions about my project and experiments.

Also I would like to thank my colleague Rafmag Cabrera for his help and guidance with technical experiments and career advise. It was a pleasure working with him through these years. To my colleague and husband Emmanuelle Merced for being there always life coaching me in times of struggles and successes.

To my family and friends who reminded me what really matters in life and provided me emotional support during my struggles. They filled this journey with great memories that I will carry.

TABLE OF CONTENTS

LIST OF TABLES

LIST OF FIGURES

CHAPTER 1

INTRODUCTION

Vanadium dioxide VO_2 exhibits a solid-to-solid phase transition in which the crystallographic structure of the material changes from monoclinic (M) to rutile (R). This transition in VO_2, also referred to as an insulator-to-metal transition (IMT), can be induced thermally, in which case occurs at a temperature of around 68 °C [1]. The optical, electrical, and mechanical properties of VO_2 change simultaneously during the IMT. The multifunctionality of VO_2 across its IMT has enabled the use of this material in many specific devices, including temperature and optical sensors [2, 3], micro-electro-mechanical systems (MEMS) actuators [4, 5] and optical active components, such as modulators [6] and shutters [7].

The optical transmittance of VO_2 decreases from near to mid infrared (IR) wavelengths (900 nm to 2500 nm) across the IMT [8, 9]. The magnitude of this change increases with wavelength until terahertz frequencies around 1 THz [10]. The transmittance of VO_2 changes abruptly showing the hysteretic behavior across its phase transition for wavelengths around 1550 nm as shown in **Figure** 1.1. In this **Figure** 1.1 the transmission across a $\sim$ 300 nm VO_2 thin film on SiO_2 substrate was measured by a laser beam profiler. The film was heated at a constant rate of $\sim$0.4 °C/s waiting $\sim$3 s between sampling for temperature stabilization. The optical signal was normalized with respect to the VO_2 transmission at $\sim$25 °C to set a 100 % transmission for the VO_2's M phase. The R phase of the material corresponds to its transmission at 100 °C after the IMT. This signal was attenuated to $\sim$1 % from the initial transmission, which makes VO_2 desirable for optical applications.

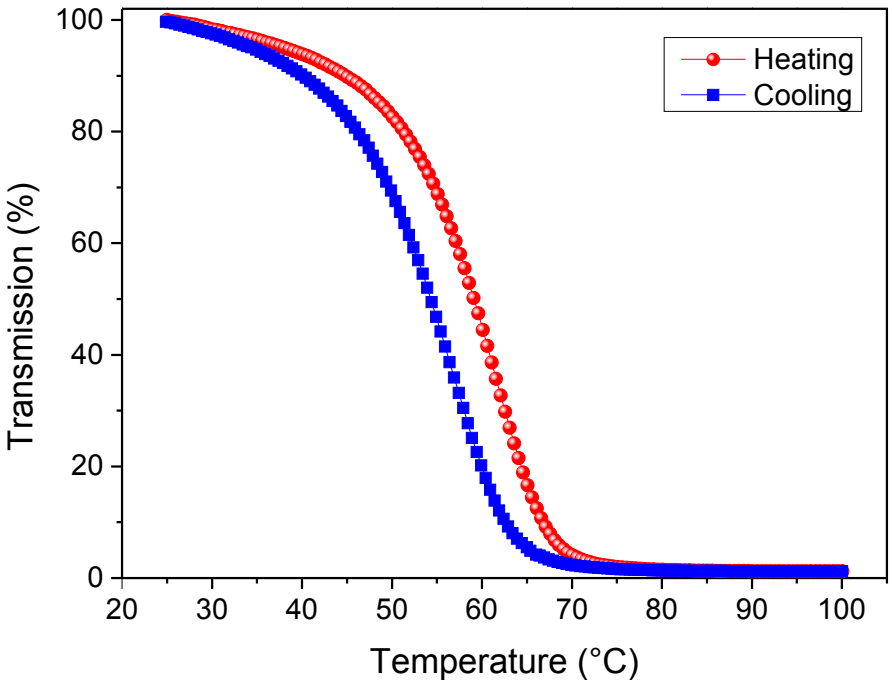

Figure 1.1: Optical transition in VO_2 for a wavelength of 1550 nm as a function of temperature for a heat rate of ~0.4 °C/s.

The electrical resistance in VO_2 drops from two to three orders of magnitude when the solid-to-solid phase transition is induced [11]. The magnitude and shape of this drop depends on many microstructural properties, but mainly on the film's stoichiometry, grain size and crystal orientation. The electrical transition for the same ~ 300 nm VO_2 thin film on SiO_2 substrate is shown in **Figure** 1.2. During this measurement the heat rate was ~0.4 °C/s. It reveals its hysteretic behavior, similar to the change in transmission shown in **Figure** 1.1.

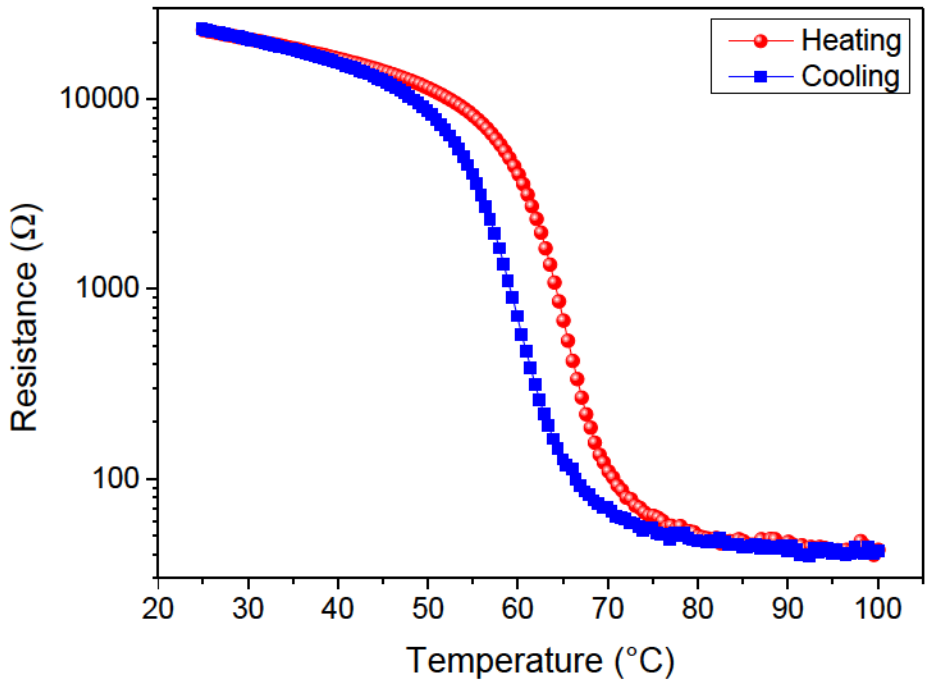

Figure 1.2: Electrical resistance change in VO_2 as the phase transition is thermally induced with a heat rate of $\sim$0.4 °C/s.

Although the change of individual properties shows hysteresis, the correlated nature of the optical and electrical properties changes across the phase change in VO_2 can be combined to significantly reduce the hysteresis. This strong correlation between the optical and electrical properties in VO_2 during the material's IMT allows for the implementation of a self-sensing mechanism that enables the development of electro-thermo-optical devices where the optical properties can be controlled by sensing the resistance of the VO_2 film.

1.1 Problem Description and Motivation

IR projectors are widely used for testing IR cameras, but they are also used to assists IR vision in military training, to provide deception to the reality for homeland security, and to simulate the operating environment for IR sensors. While the IR cameras technology

keeps growing, there is a need for IR projectors to match the current IR cameras technology demands, including stable images. Three different technologies have been used to develop IR projectors: thermal resistive arrays, modulation-based deformable micro-mirrors, and quantum photonics. These previous technologies exhibited issues such as large power consumption, high peak currents, complex and expensive fabrication methods, slow processing speeds and flickering images [12]. Stable IR images can be achieved integrating VO_2 thin films with a simple optical system and process.

Near-IR variable optical attenuators (VOAs) are used in optics to control the intensity of a transmitted optical signal. VOAs can provide discrete or continuous attenuation. Mechanical systems with motorized stages facilitate the switching among attenuation levels, but noise is introduced with the mechanical movement. Such devices have limited attenuation levels despite being continuous and are not offered with fully-electronic control. Electronic control of the optical IR transmittance through VO_2 can be achieved by the strong correlation between the material's optical and electrical properties.

The problems addressed in this thesis are:

- Study of a sol-gel process to deposit VO_2 thin films on large areas such as 4 inches wafers.
- Characterize VO_2 thin films grown by sol-gel process by X-ray diffraction, Raman spectroscopy, surface topography, electrical and optical behavior.
- Programing optical states in VO_2 thin films by localized heating, using the optical memory of VO_2 to achieve multiple optical states.
- Use the developed VO_2-based IR projector to store and project stable IR images.
- Characterize the speed, contrast and resolution of the developed IR image projector.
- Measured the optical and electrical VO_2 properties simultaneously to determine a model to accommodate transmission-to-resistance experimental data.

- Use self-sensing feedback techniques to electronically control the optical transmission of a designed and fabricated monolithic micro variable optical attenuator.
- Characterize the time response and attenuation parameters of the developed micro VOA.

1.2 Thesis Statement

This work presents the development of two optical devices suitable for IR wavelengths: 1. an IR image projector, and 2. a fully electronically controlled variable optical attenuator (VOA). Two different VOA designs were fabricated and actuated by conductive heating in two different ways: one by using an external Peltier heater and the other by using integrated resistive heaters.

Thesis Statement: *The development of an IR image projector is accomplished by exploiting the VO_2 optical memory capability, which improves current image projectors technology issues offering a simple optical system and process. A fully electronically variable optical attenuator, which uses the strong correlation between the electrical and optical properties in VO_2 can provide advantages in terms of simple fabrication and attenuation self-sensing control.*

1.3 Thesis Contributions

This thesis addressed the problems described in **Section 1.1**. The contributions of this thesis are: 1. the comparison of sol-gel deposition process and pulsed laser deposition for growing of VO_2 thin films, 2. the development of a near-infrared (NIR) image projector and 3. an electronically controlled VOA. Localized photo-thermal excitation was used to trigger the VO_2 phase transition, creating a pattern on the thin film which allowed for the

projection of an NIR image; self-sensing technique was implemented to reduce the hysteresis of the optical transmission across the VO_2 thin film during its phase transition.

1.4 Dissertation Outline

The remaining work is organized as followed: **Chapter 2** presents the background of VO_2 thin films properties and deposition processes, electro-thermo-optical devices including IR scene projectors and variable optical attenuators. The optical, electrical and structural properties of VO_2 are discussed. VO_2 deposition is discussed in **Chapter 3**. In **Chapter 4** a NIR image projection based on the optical memory of VO_2 is developed and discussed. A variable optical attenuator for NIR is presented in **Chapter 5**. A scaling study of micro size variable optical attenuator devices is presented in **Chapter 6**. Last **Chapter 7** shows the contributions of this work and the proposed work for further investigation.

CHAPTER 2

BACKGROUND

2.1 Optoelectronic Devices

Optoelectronic devices combine electrical and optical signals to detect or convert one signal into another signal. Nowadays, solar cells are the most commonly known optoelectronic devices. They use photons to create electron-hole pairs in a semiconductor, which generate an electric current [13]. Other optoelectronic devices use electrical signals to produce, detect, manipulate or control optical signals such as optical sources and detectors. Optical sources use electrical signals to produce optical radiation (e.g. photodiodes, LEDs, LASERS) [14, 15], while photodetectors detect optical radiation and convert it into electrical signals (e.g. cameras, charged-coupled devices (CDDs)) [16]. IR image projectors and electronically controlled variable optical attenuators (VOAs) are optoelectronic devices, which use electrical signals to manipulate optical signals. **Figure** 2.1 shows the classification of these two optoelectronic devices. Many other types of optoelectronic devices exist; but the emphasis is given to IR image projectors and VOA, since those are the devices developed in this thesis.

Optical attenuators reduce the intensity of optical signals. These components can be passive or active depending on the used technology and applications. Active optoelectronic devices require an external power source in order to be operated, while passive components do not.

Image projector technologies are based in optical sources combined with different physics and materials to drive these projection processes for visible and IR wavelengths. Projectors technologies use plasma displays, liquid crystal displays (LCD), and digital light projectors (DLPs) [17, 18, 19].

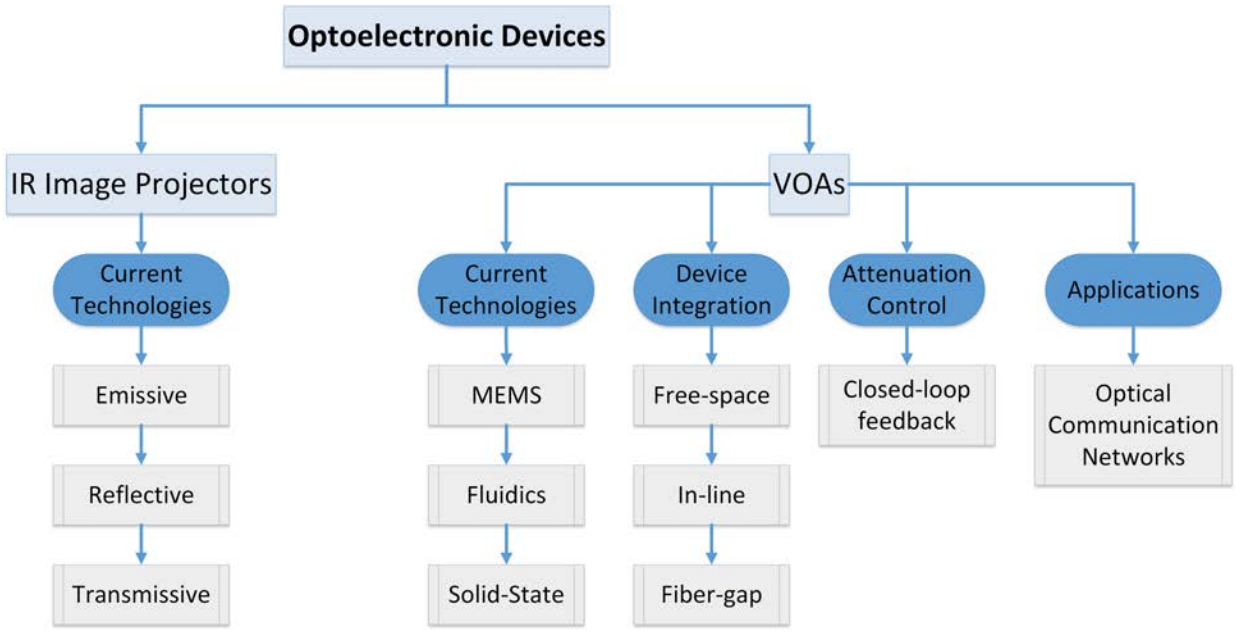

Figure 2.1: Classification of IR image projectors and VOAs optoelectronic devices.

2.2 Infrared Image Projectors

Infrared image projectors, also known as infrared scene projectors, have been developed since 1970's to test IR sensors [20]. A thermal source covered with a shadow mask was used as an emitting IR radiation to produce a static synthetic image. Soon after, demands for dynamic image projectors technologies emerged. In 1982 the Bly cell was reported as the first dynamic IR projector [21]. A visible light was converted to IR by using a Bly cell, which consisted of a suspended membrane (gold/cellulose nitrate) in vacuum. A visible image was projected into the cell, absorbed and emitted in the IR region by the membrane. Extensions to this technology emerged during the same decade with thermal resistor arrays and liquid crystal valve technologies [20]. These developed technologies for IR projectors can be divided in three categories: emissive, reflective and transmissive.

2.2.1 Current Technologies

2.2.1.1 Emissive IR projectors

Emissive IR projectors are based on devices emitting IR radiation by Joule heating. These optoelectronic devices can be formed by current-driven thin film resistors, suspended membrane resistors, silicon bridge resistors, Bly cells arrays, or laser diode arrays. Metals and SiGe are some of the materials used to fabricate emitting resistors [22]. Thermoelectric elements has been investigated for single pixels, which showed an emissivity of 0.95 at 130 °C [23]. They compared this performance with Si emitters having ∼0.1 emissivity at 140 °C. Previously described resistors arrays have been monolithically fabricated with CMOS integrated circuits to independently activate each resistor as a pixel to project an image [24, 22]. **Figure** 2.2 shows a micro-electro-mechanical (MEMS) suspended membrane resistors array. In this device the active emitter area (image pixel) is the isolated heating element.

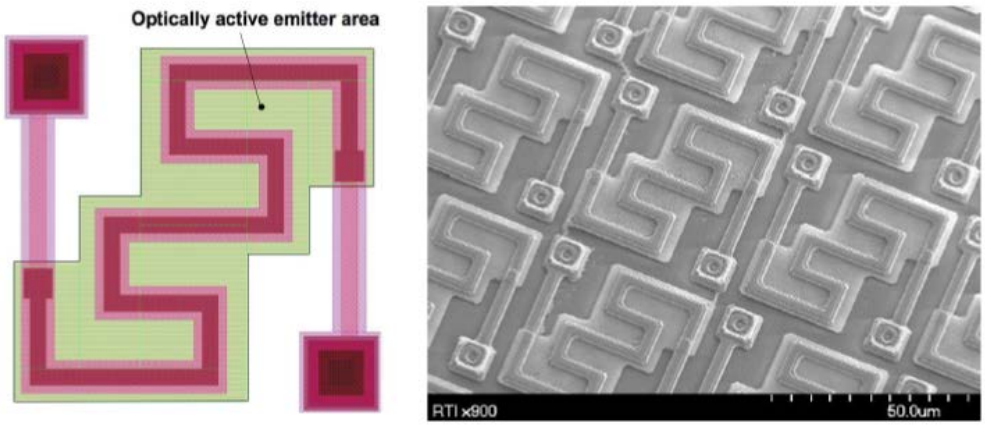

Figure 2.2: Suspended membrane resistors array used in emitter IR projectors [24].

IR laser diodes are part of this emission technology category. IR radiation from a current-driven laser diode arrays were programed to project an image as shown in **Figure** 2.3 [12].

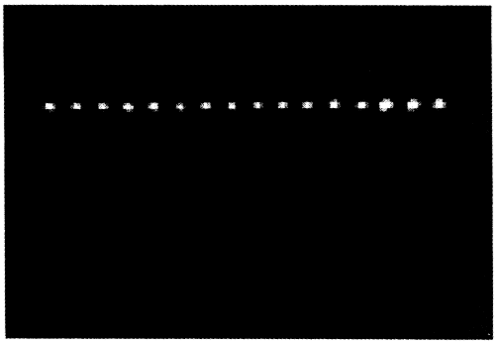

Figure 2.3: IR laser diode array used in emitter IR projector [12].

2.2.1.2 Reflective IR Projectors

Reflective IR projectors are based on materials or structures that reflect IR wavelengths and mechanisms to control the reflection direction. These modulation-based electro-optical devices, such as scanning lasers and micromirrors arrays. The intensity of an IR laser beam is modulated and steered vertically. A reflective scanning mirror is used to determine the horizontal direction projecting an image into an image plane (See **Figure** 2.4).

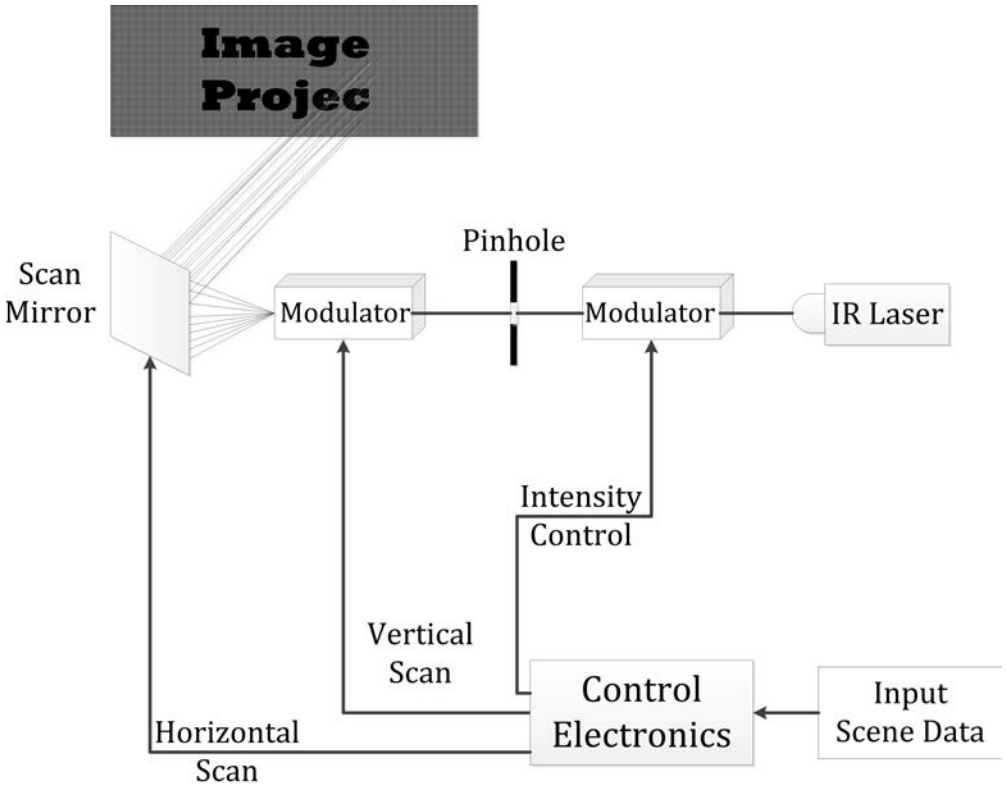

Figure 2.4: IR projector based on laser scanning technology [12].

Digital micromirror devices (DMD) modulate IR radiation by controlling individual IR reflecting mirrors electronically [25]. **Figure** 2.5 shows the optical setup for projecting an image with a micromirror array. An IR lamp irradiates into the micromirror array. These mirrors are electronically controlled to tilt ±20° into "ON" or "OFF" positions. One plane is projected as an IR image and the other is absorbed.

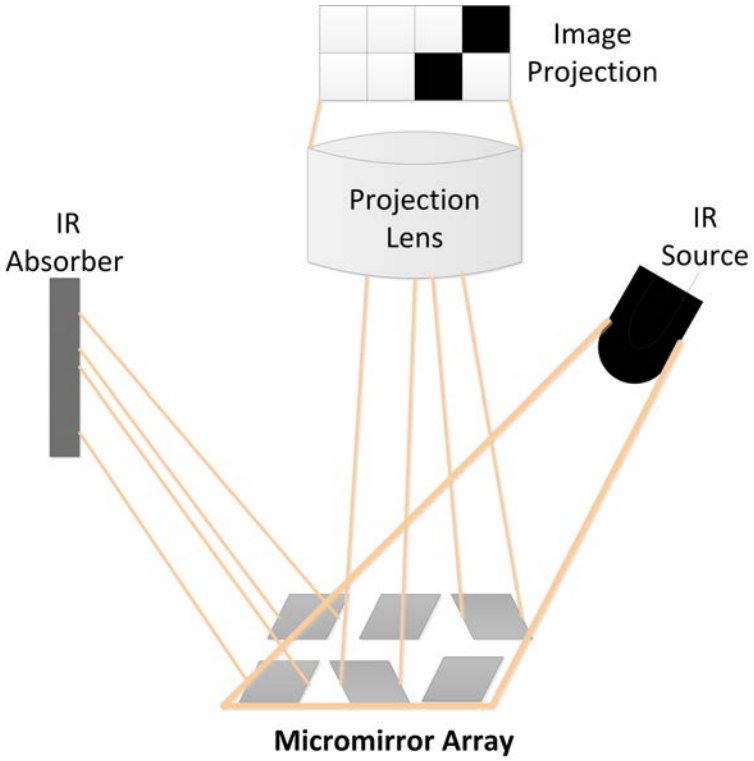

Figure 2.5: Projection setup with reflective IR micromirrors array [25].

2.2.1.3 Transmissive IR Projectors

Transmissive IR projectors are based on materials and systems that can modulate or control IR radiation passing through them. This category includes IR liquid crystal light valves (LCLVs) projectors and galvanic cells, which can modulate IR radiation. IR LCLV projectors converts visible wavelengths into IR wavelengths [26]. A visible image is projected to one side of the LCLV. The pattern is transferred to the liquid crystal (LC) causing a polarization

change due to molecular rearrangement. Polarized IR radiation is focused on the LC side and rotated by the polarized pattern [12]. **Figure** 2.6 shows the use of LCLVs as IR projectors.

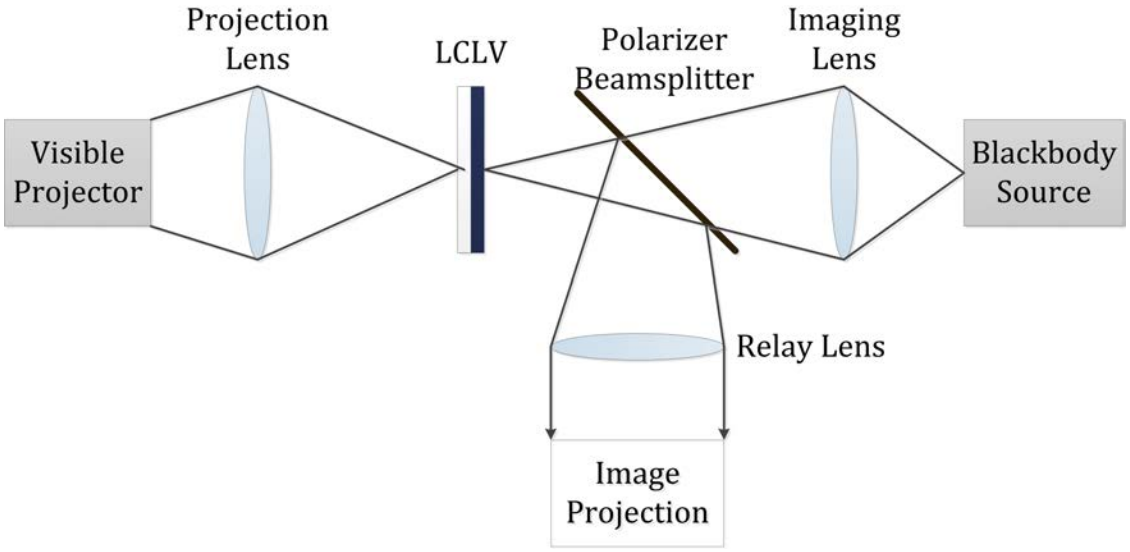

Figure 2.6: Transmissive IR projector using a liquid crystal light valve (LCLV) [12].

2.2.1.4 Other Technologies for IR Projectors

Other technologies for IR projectors have been explored, such as bulk silicon photonic (transmissive), plasma display (emissive) and electron-beam-addressed membrane light modulation (reflective) [27, 28, 29]. The bulk Si photonic projector is based on optical down-conversion technique, which uses the indirect band gap of Si to absorb short wavelengths ($\lambda \leq 1$ μm) and emit longer wavelengths in the IR thermal region [30]. Plasma displays are based on cavities structures filled with gas, which are electronically driven to produce plasma. Noble gases, CO and CO_2 can be used for IR wavelengths [28]. Membrane light modulation, also known as deformable mirrors spatial light modulation, was addressed by a scanning e^- beam gun [29]. An IR source irradiated the membrane which was used to modulate the IR reflection onto an image projection plane.

2.3 Variable Optical Attenuators (VOAs)

Variable optical attenuators (VOAs) are another key components in optical communication systems. Optical signals with fixed intensity are desired in these systems. However, since they travel long distances often are amplified throughout the transmission lines. When these signals reach the routing or modulation systems they have different intensities from which they were generated. VOAs are used to adjust these intensities with the equalization and synchronization of multiple optical signals and channels.

VOAs in visible and NIR wavelengths are widely used in optics, photonics and optical networks. The most commonly known attenuators are used in free space configuration, while more complex designs are combined with optical fibers in photonics and communication networks. They are commercially available for a single optical density (OD), meaning a single attenuation level. For multiple attenuation values, a step variable or continuous variable attenuator with manual control is used.

VOAs optoelectronic components are electronically driven and interact with optical signals without detecting or producing them, similar to optical filters, couplers, splitters, modulators, and wavelength-tunable optical filters.

In the last decade, electronically controlled VOAs have been developed to assist communication networks demands. Commercially available devices are based on optoceramic materials (PMN-PT and PLZT) [31]. MEMS-based VOAs that are compatible with optical fibers and electronically controlled have also been reported. Some of them use micromirrors and reflective materials [32, 33, 34], others are based on microfluidics, ferrofluidics [35, 36, 37], and others are assisted with piezoelectric materials [38]. Plasmonic-based VOAs have also been investigated using waveguides [39, 40, 41]. Liquid crystal cells for near-IR wavelengths have been explored in VOAs [42]. More recently, an electronically controlled VOA based on multilayered graphene operating at 785 nm was reported [43].

2.3.1 Current Technologies

2.3.1.1 Micro-electro-mechanical systems (MEMS) VOAs

MEMS-based VOAs control the attenuation by using planar reflection with deformable mirrors or by blocking the radiation with shutter-based devices using a knife edge to block part of the radiation passing through the optical path [44]. **Figure** 2.7 shows a diagram of a VOA having an electronically controlled mechanical shutter.

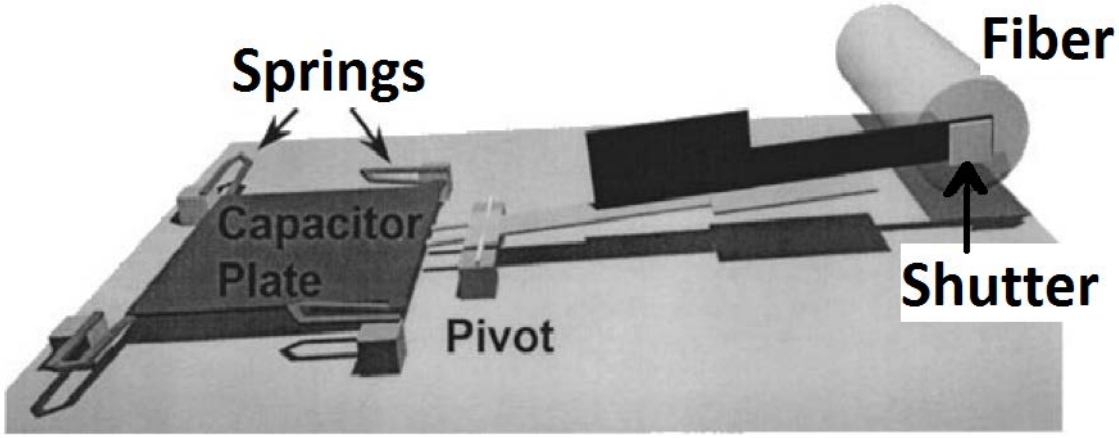

Figure 2.7: MEMS-based VOA with optical shutter [45].

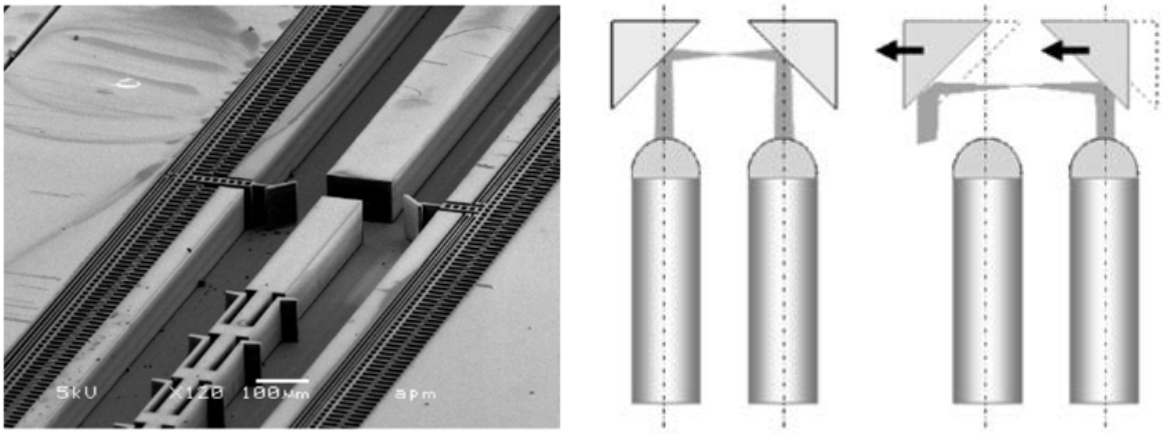

(a) (b)

Figure 2.8: MEMS variable optical attenuator by retro-reflection of IR light (a) device SEM image, (b) working principle: initial state (left) attenuation state (rigth) [34].

Several devices emerged from the technology that uses reflection to control the attenua-

tion of an optical signal. **Figure** 2.8 shows two reflective MEMS mirrors placed within an optical path to control its attenuation. In this case, electronically controlled folded-beam springs move the mirrors [34]. Piezoelectric materials were used to move reflective mirror in MEMS VOAs [38], **Figure** 2.9 and **Figure** 2.10 show a reflective plate and an elliptical mirror MEMS-based VOA, respectively. This device uses reflection to block the optical path [32].

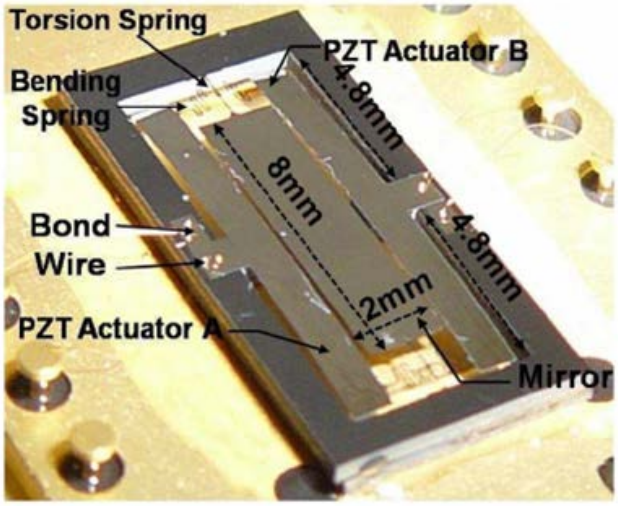

Figure 2.9: Reflective mirror MEMS variable optical attenuator [38].

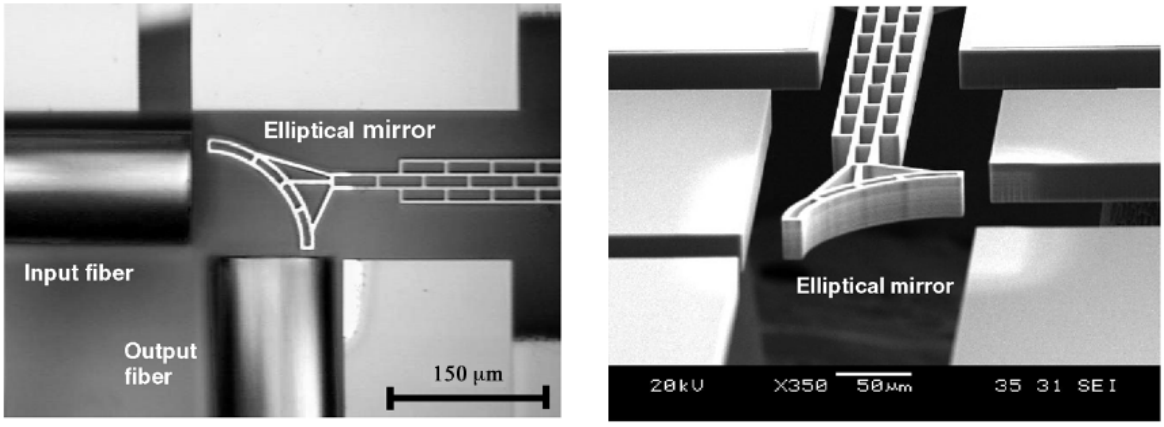

(a) (b)

Figure 2.10: Elliptical mirror variable optical attenuator (a) top view, (b) side view [32].

2.3.1.2 Microfluidics and Ferrofluidics VOAs

Microfluidic-based VOAs combine optics and fluids in micro devices without having moving parts. The fabrication of these devices is similar to those MEMS-based VOAs. Microfluidic VOAs started by placing a voltage controlled liquid lens in between an optical beam path [46]. The output of an optical fiber was aligned with this lens and coupled into a fiber. The liquid lens was formed at the interface of two different fluids. Its curvature was electronically controlled by electrowetting with an external applied voltage [47]. The beam is misaligned when the curvature of the lens changes, thus it is deflected from the fiber input. The schematic for this VOA application is shown in **Figure** 2.11

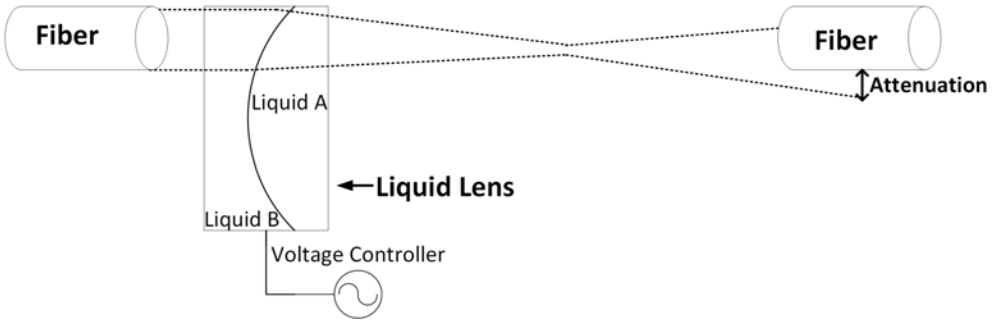

Figure 2.11: VOA device based on voltage controlled liquid lens [46].

An optofluidic tunable attenuator uses a liquid-core waveguide to change the transmission of a coupled fiber. The transmitted power changes by controlling the fluid rate of the waveguide, thus changing its core width [48]. The transmission decreases as the core width reduces. **Figure** 2.12 shows this working mechanism for this device.

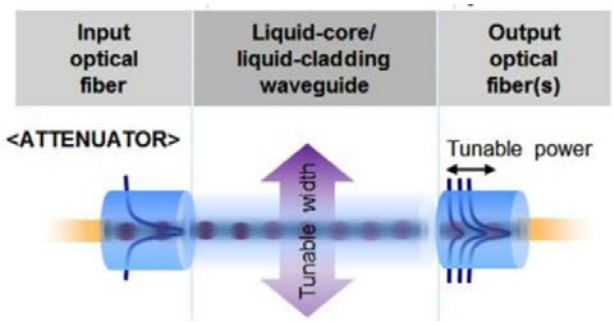

Figure 2.12: Optofluidic device with fluid rate tunable core width and attenuation [48].

A ferrofluid-based VOA shown in **Figure** 2.13 uses a fluidic shutter which is electronically controlled by an electro-magnet [37].

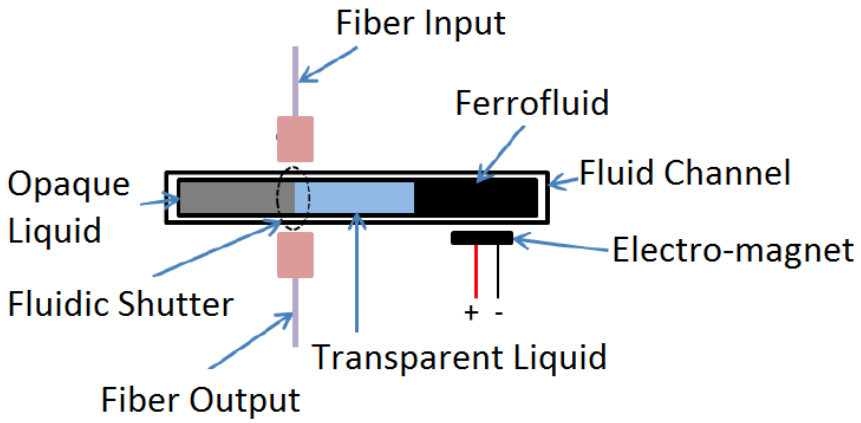

Figure 2.13: Ferrofluid based VOA [37].

A magnetic VOA was developed by using ferrofluid dispersed on a microchannel and with ferrofluid doped PDMS [49]. An optical fiber was aligned into a cantilever waveguide suspended inside this microchannel. This cantilever was actuated by applying an external magnetic field, thus deflecting the waveguide output. The fiber input gets attenuated by this deflection. Using a similar fabrication process a PDMS cantilever was doped with the same ferrofluid and actuated by an external magnet.

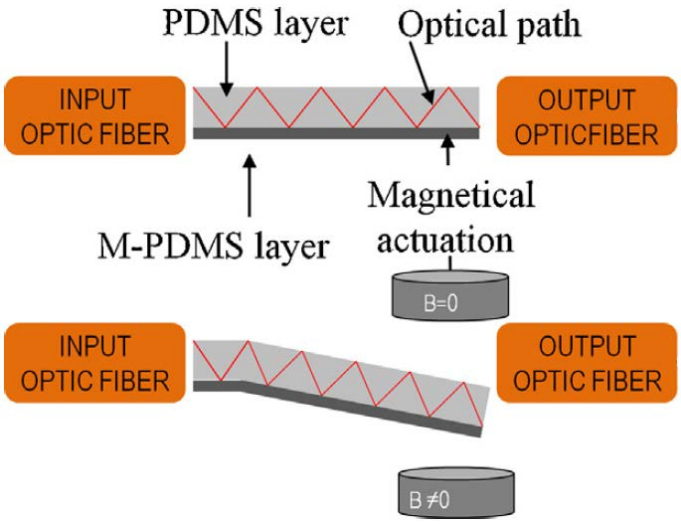

Figure 2.14: Ferrofluid doped PDMS cantilever waveguide actuated by electro magnets [49].

Figure 2.14 shows the attenuation of the laser beam with the cantilever deflection.

2.3.1.3 Solid-state VOAs

Solid-state VOAs, also known as electro-chromic VOAs (ECVOA) are based on electro-optic (EO) or electro-chromic (EC) materials. The optical properties of these EO or EC materials change when an electric field is applied. Some of these materials are polymer complexes, optoceramics, organic materials and materials oxides [50].

Redox electroactive polymers have been explored in VOAs devices, such as Poly(3,4-ethylenedioxythiophene) (PEDOT), Poly(3,4-alkylenedioxythiophene) (PADOT), and dual polymer layers: PDDA/Naph-SO_3Na [51, 52, 53]. These polymer-based VOAs operate in reflective mode as shown in **Figure** 2.15 with a switching speed between 1 to 5 s.

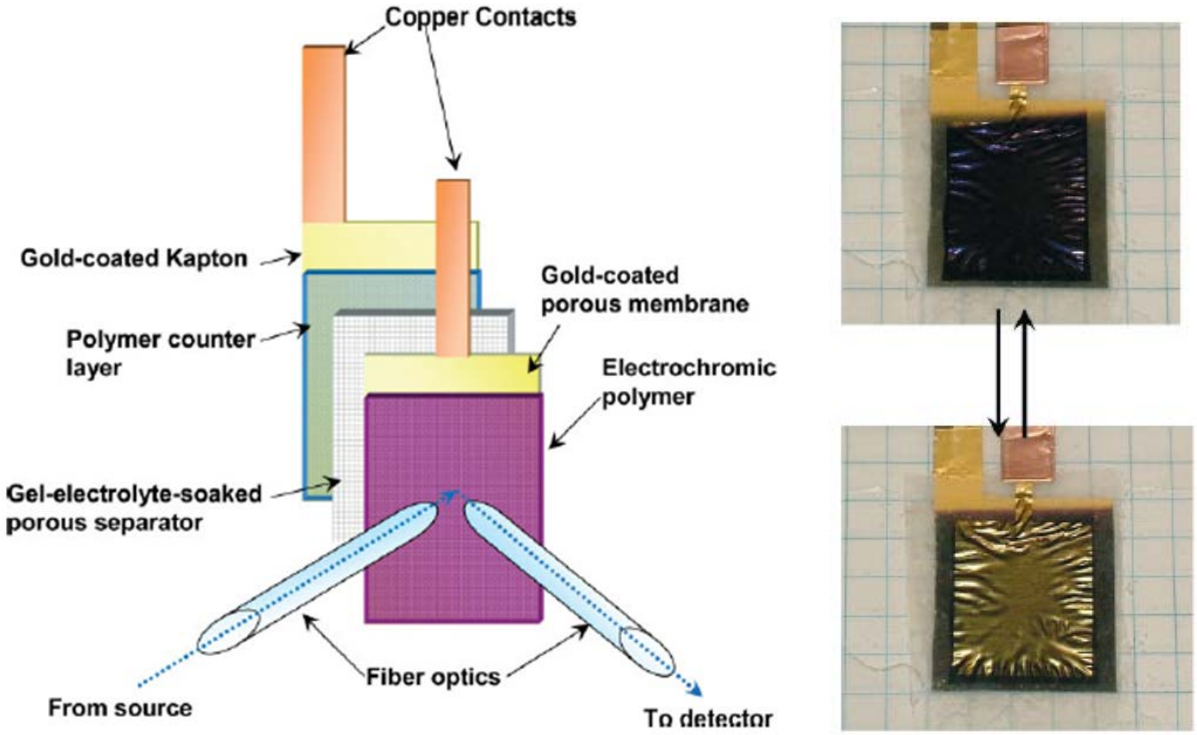

(a) (b)

Figure 2.15: Polymer-based electrochromic variable optical attenuator (a) device diagram, (b) device image in neutral (top) active (bottom) [52].

Optoceramics such as $Pb(Mg_{1/3}Nb_{2/3})O_3$-$PbTiO_3$ (PMN-PT), $Pb_{1-x}La_x(Zr_yTi_{1-y})_{1-x/4}O_3$

(PLZT) and $LiNbO_3$ have been used in commercially available VOAs operating in transmission mode [31]. Dinuclear molybdenum complex (oxo-Mo(V)) was used in an IR VOA with applied voltage of 1.5 V [54].

2.3.2 Device Configuration

VOAs can be implemented in free-space, in-line with optical fibers or in fiber-gap configuration [55, 45]. This configuration is based on how the propagating light interacts with the VOA. In free-space configuration the light propagates through air before and after the VOA device. In-line configuration accommodates bare fibers into the device as shown in **Figure** 2.16. Fiber-gap configuration uses a split bare fiber as shown in **Figure** 2.17. These split fibers can be collimated and conditioned before reaching the VOA by using external passive components. This type of configuration is in a way a compact form of free-space configuration since the light propagates through air after the fiber is split. Other fiber-gap configurations have a split fiber with no extra optics as shown in **Figures** 2.7 and 2.18. In general the free-space configuration can be adapted with bare fiber [56], dual fiber collimator [57], or fiber output/input collimator [58].

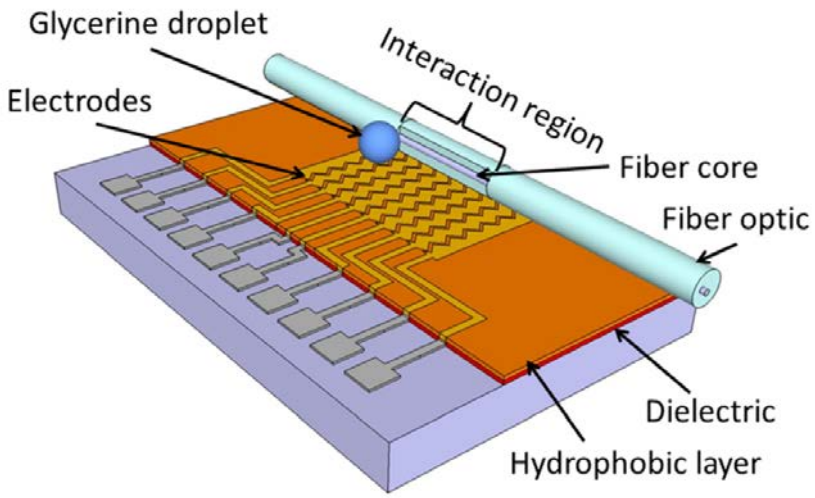

Figure 2.16: In-line VOA configuration [55].

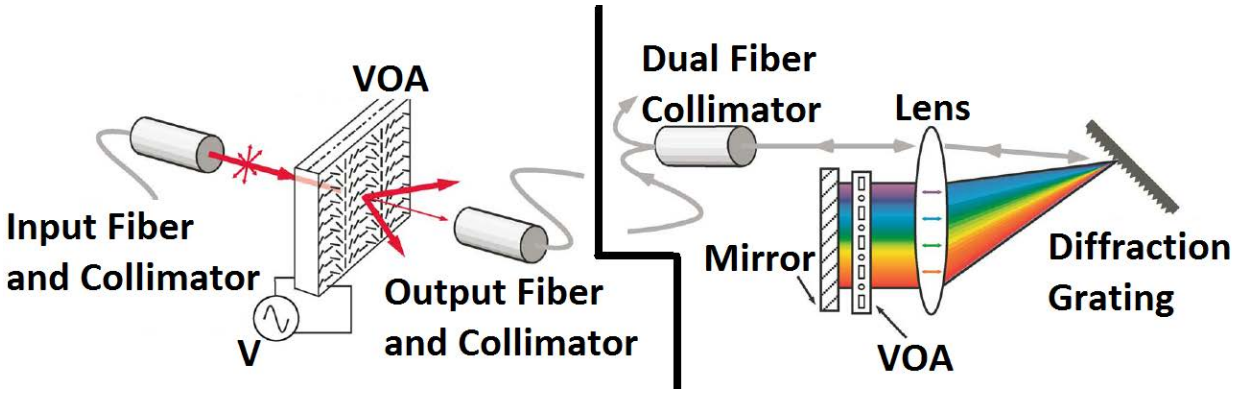

Figure 2.17: Fiber-gap VOA configurations with couplers (left), lens, dual collimator, mirror and diffraction grating (right) [59].

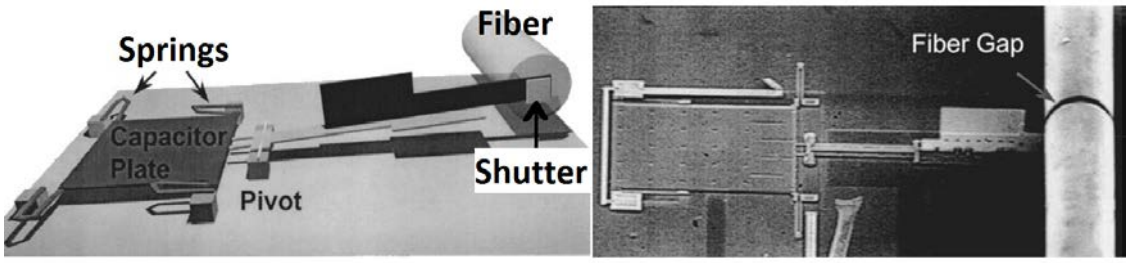

Figure 2.18: Fiber-gap VOA configuration with split fiber and no additional optical components [45].

2.3.3 Attenuation Control

Several optical systems with attenuation control using variable optical attenuators have been developed for MEMS and EO based VOAs [60, 61, 62]. The attenuation level is controlled by closed-loop feedback as shown in **Figure** 2.19. The output optical signal from the VOA is split into a photodetector and the output of the system. The photodetector signal is used for the feedback control.

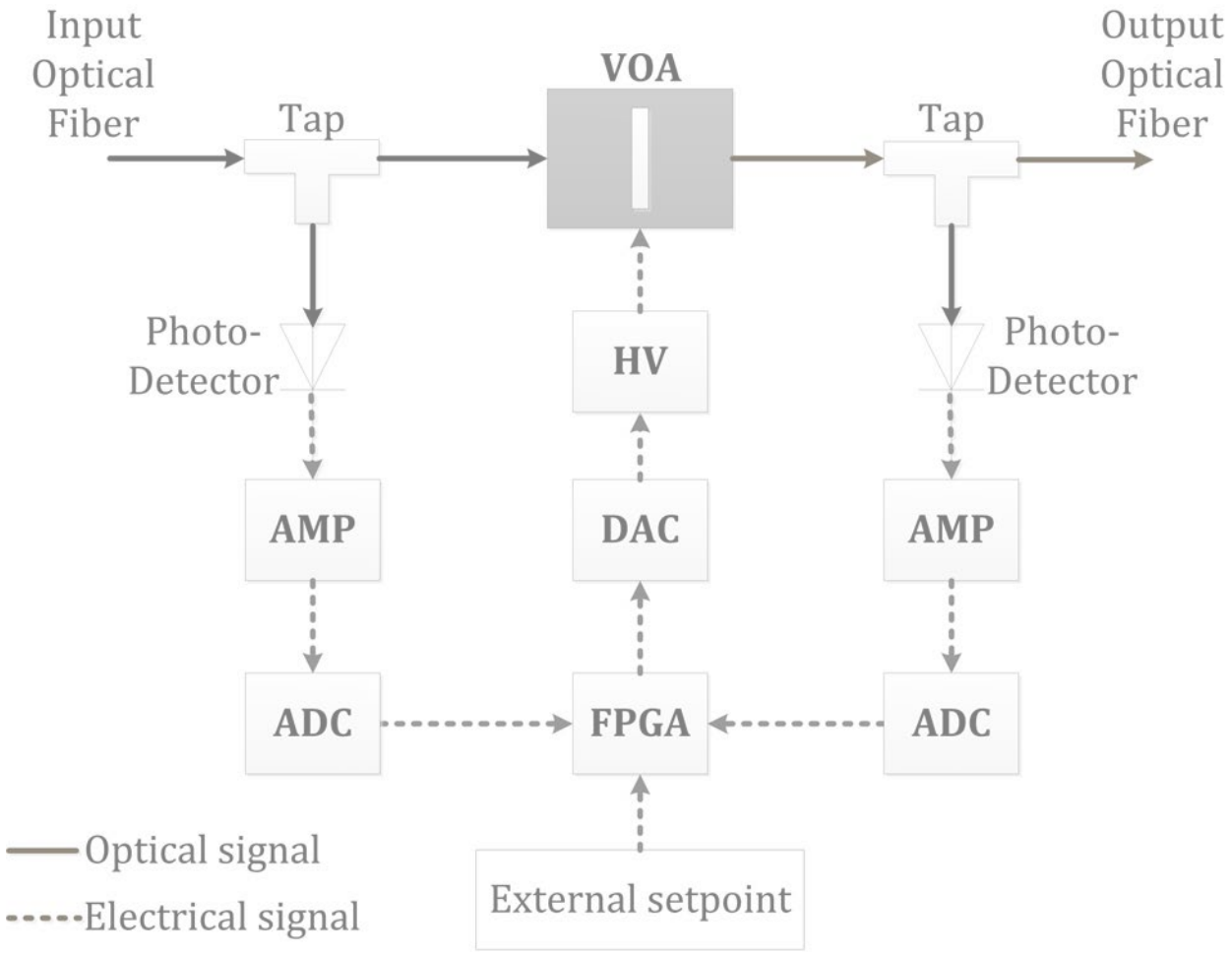

Figure 2.19: Closed-loop control system for a VOA [61].

2.3.4 Applications

2.3.4.1 Optical Communication Networks

Optical communications networks use advanced modulation systems to route signals throughout long distances. These modulation systems need to minimize signals crosstalk and regeneration . Dense wavelength division multiplexing (DWDM) systems are modulation systems widely use to pack and route optical signals. DWDM is a cost-effective solution for optical networking because it shares optical components for all the channels connected to it [63]. **Figure** 2.20 shows the basic optical network for DWDM. Optical signals with a limited wavelength window ($\lambda_1 \sim \lambda_n$) are packed by a multiplexer (MUX) into a transmission optical fiber. Signals are amplified as needed according to the transmission distance. An optical add-drop multiplexer (OADM) routes the signals by adding or removing them. These signals are packed again into an optical transmission fiber and recovered by a demultiplexer (DEMUX).

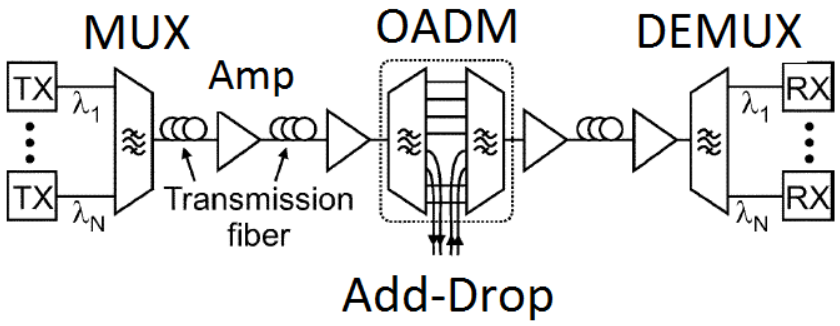

Figure 2.20: Optical network for dense wavelength division multiplexing (DWDM) [63].

OADMs, also known as reconfigurable optical add-drop multiplexers (ROADMs) are extensively used in DWDM [64]. All-optical ROADMs modulate optical signals without converting them into electrical signals by transmittance modulation [63].

ROADM technologies are based on polymer thermo-optic array, waveguide and Braggs grating, optical switches and variable optical attenuators (VOAs) [65, 66, 64, 67]. A monolithic ROADM configuration based on arrayed waveguide grating (AWG) and VOAs integra-

tion is shown in **Figure** 2.21. This 9-channels ROADM uses two AWGs and 4 VOAs. The packed input signal ($\lambda_1 - \lambda_9$) is recovered into nine signals by *AWG 1*. λ_1 goes to the output channel. Four channels ($\lambda_2 - \lambda_5$) are set to add or drop signals at the input of *AWG 1* and output of *AWG 2*. Four VOAs control the intensity for $\lambda_6 - \lambda_9$ and connect both AWGs. The output signals are multiplexed by *AWG 2* into four drop channels and one packed signal containing λ_1 and $\lambda_6 - \lambda_9$.

Electronic control of VOA arrays are required to control optical signals and to advance this ROADM technology.

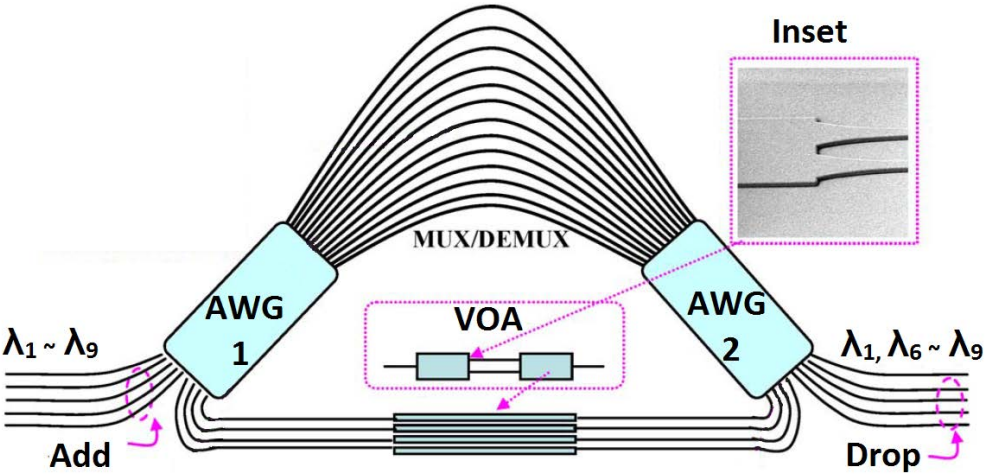

Figure 2.21: Arrayed waveguide grating and variable optical attenuator integration (AWG-VOA) [67].

2.4 Vanadium Dioxide

Vanadium dioxide (VO_2) is a transition metal oxide exhibiting an insulator-to-metal transition (IMT). The electrical, optical, mechanical and structural properties of VO_2 change during the IMT. The thermally-induced IMT transition occurs around ~68 °C [1, 8, 68, 69]. VO_2 is one of the stable phases of vanadium oxides, which exhibits a transition near room temperature [70]. **Figure** 2.22 shows the transition temperature for other vanadium oxides. Vanadium pentoxide (V_2O_5) also exhibits an IMT for a transition temperature of ~280 °C

[71]. Many research efforts have been put to investigate ways to manipulate this transition temperature in VO_2. The transition temperature of VO_2 could decrease or increase by substitutional doping with Cr, Ti, W, Fe, among other elements [72, 73, 74, 75].

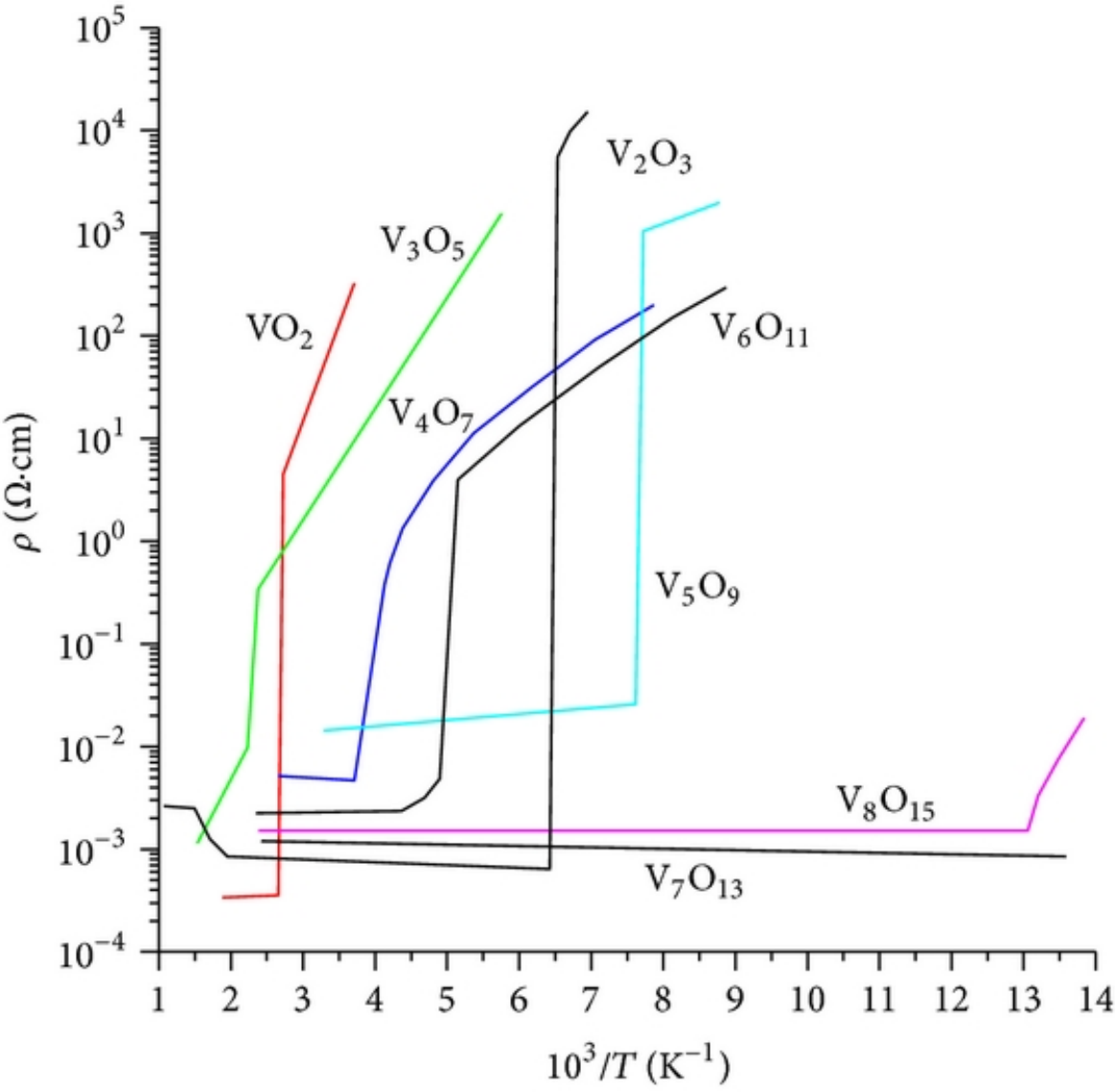

Figure 2.22: Insulator-to-metal transition in different vanadium oxides [70].

The driven mechanisms for this transition in VO_2 still under debate in the scientific community. Recently, the behavior described by Mott-Peierls transition was reported [76]. The Peierls mechanism (related to the atomic structure) and the Mott transition described as the

closure of the Mott band gap (around 0.7eV) have been extensively studied as independent mechanisms, but in the particular case of VO_2, both mechanisms are related [77, 78, 79, 80].

During this transition, VO_2 undergoes the insulator-to-metal transition (IMT) and a structural phase transition (SPT). The IMT is related to the film's change in electrical resistivity and the SPT is associated to the crystalline structure transition [1, 81, 82]. These transitions are strongly correlated since the change in the atomic structure causes a reduction in the energy bandgap of the material. This VO_2's transition is fully reversible and it occurs relatively fast (∼2 ns) when triggered by voltage pulses [83].

2.4.1 Structural Transition

The structural phase transition in VO_2 is solid-to-solid phase transition, in which the material crystal structure change from monoclinic (M_1) at room temperature to rutile (R) at higher temperatures. During the structural transition the interplanar distances a, b and c change as the crystal structure is reordered. The distances are a_m=5.75 Å, b_m=4.53 Å, c_m=5.38 Å and a_r=b_r=4.55 Å, c_r=2.85 Å for the monoclinic and rutile phase, respectively. The c_r direction contracts after the SPT transition [84]. The structure change is shown in **Figure** 2.23.

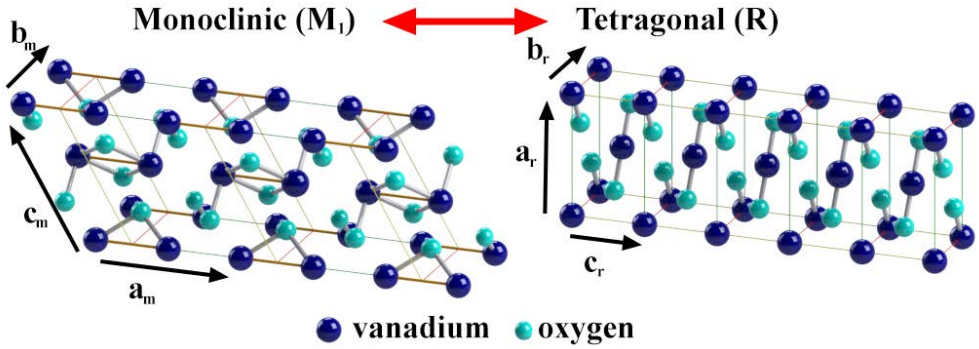

Figure 2.23: VO_2 structural transition representation of the unit cells [5].

Previously characterized VO_2 thin films grown PLD showed high orientation in the (011) monoclinic planes at room temperature with the c_r direction oriented parallel to the substrate

(SiO_2 and Si). During the transition, as the c_r contracts, stress is introduced on the film, changing the material's mechanical properties.

2.4.2 Electrical Transition

The insulator-to-metal (IMT) transition in VO_2 was initially described by crystal field theory [85]. It was described that the unusual properties in transition metal oxides were due to electronic reordering in the outer d orbitals [86].

The vanadium atoms occupy the octahedral interspaces between oxygen atoms in the tetragonal phase as shown in **Figure** 2.23. Hybrid molecular bands ($d_{||}$ and d_{π}) are formed by the oxygen 2p and vanadium 3d outer orbitals [87]. These two bands are near to the Fermi energy level and participate in the IMT [88]. The $d_{||}$ band split into valence (bonding, low energy) and conduction (anti-bonding) bands resulting in a bandgap of $\sim 0.7\,eV$ for the insulator state as shown in **Figure** 2.24. During the metallic phase, the d_{π} shift to lower energies and the $d_{||}$ bands merge closing the energy bandgap.

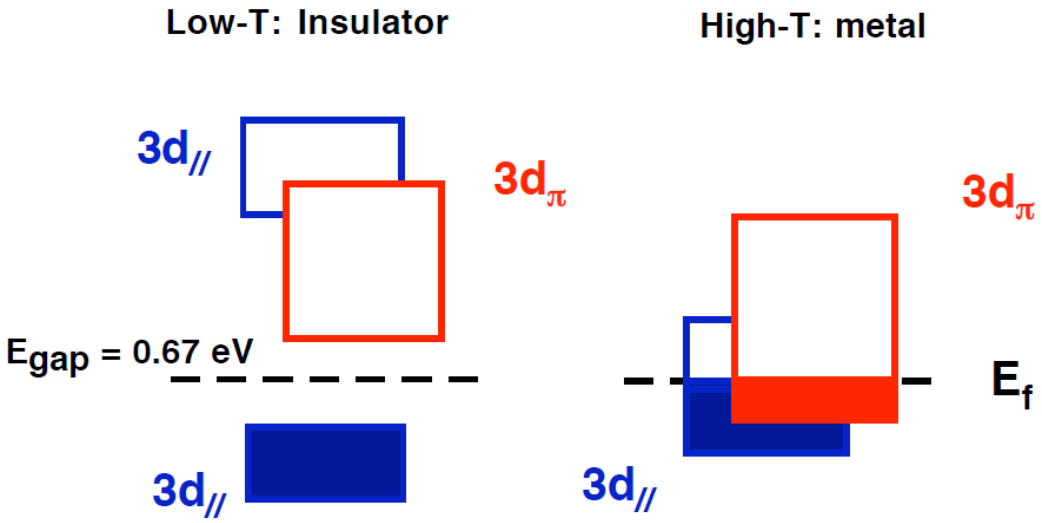

Figure 2.24: Band diagram of VO_2 insulator state (left), metal state (right) [88].

2.4.3 Optical Transition

During the VO_2's optical transition the transmission, reflection and absorption all change. Recent studies suggest this the change in the optical and electrical properties comes as the result of the first-order insulator-to-metal-transition (IMT) in VO_2, which is not driven by the structural phase transition (SPT) [68, 89].

The VO_2 transmission changes abruptly from 900 nm to 2500 nm wavelengths during the IMT [8]. The magnitude of this change increases with wavelength until terahertz frequencies (λ=300 µm) [10]. This optical switching capability of VO_2 has been explored for mid-IR to NIR image conversion and optical memory [90, 91]. **Figure** 1.1 shows the optical transition in VO_2 for λ=1550 nm.

2.4.4 Optical Memory

The optical transition in VO_2 exhibits a hysteretic behavior. The hysteresis in VO_2 thin films make it possible to use it as an optical memory. This memory capability has been investigated for multiple optical states programmed into a VO_2 thin film as as function of photo-thermal excitation (see **Figure** 2.25) [91].

Several technologies emerged from this optical memory in VO_2. Among the first devices, single crystal VO_2 was used to develop an IR optical modulator, which exhibited a very slow switching response due to the single-crystal thickness and a resistive heater used to induce the switching [6]. Later, the materialâĂŹs switching response was improved by using a VO_2 film and Joule heating through doped-Si heating resistors, and an IR shutter was developed [7]. More recently, a millimeter-size switchable IR filter array was developed using VO_2 as the thermochromic layer, diamond as a heat sink, chalcogenide glass for thermal insulation with the substrate, and Pt electrodes as resistive heaters [92].

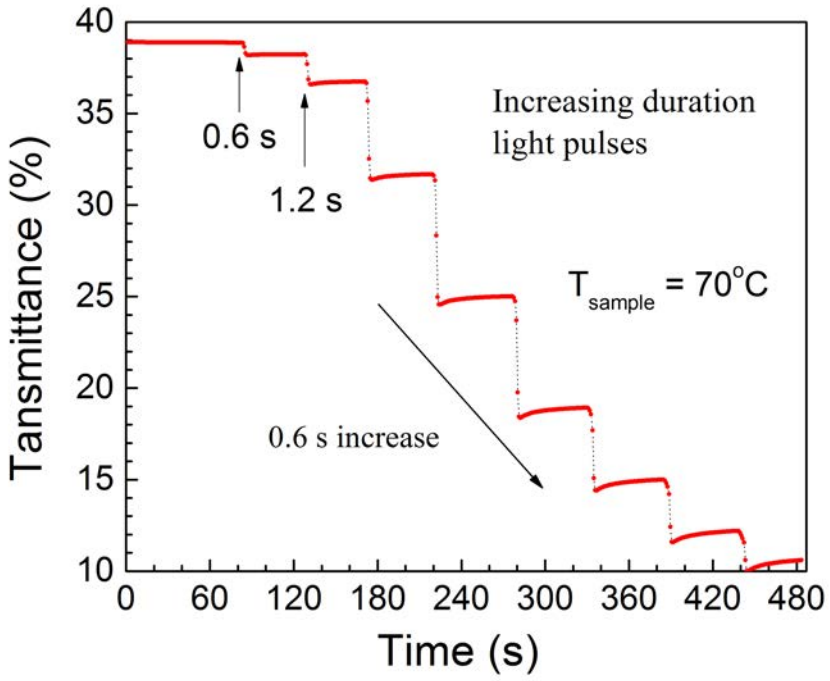

Figure 2.25: Multiple optical states in VO_2 programed by photothermal actuation [91].

2.4.4.1 Other Optical Memory Systems and Materials

Optical memory systems emerged in the 1970s with holographic data storage [93]. After decades of research compact disks (CDs) were released in 1983 [94]. These systems evolved to digital video discs (DVDs) and blue-ray discs. In these systems the data is stored as mechanical indents or pits (dark spots) onto a disk. These disks are optically read based on a readout laser reflection [95]. **Figure** 2.26 shows the diagram for the CDs optical readout system. A laser beam is collimated and polarized before passing through a quarter wave ($\lambda/4$) plate, which introduces a 90° phase difference. The circular polarized beam is reflected into a mirror and focused into the disk. The reflective coating on the CD reflects the beam back into the $\lambda/4$ plate changing its polarization again with a phase shift of 90°. The beam is reflected at the beam splitter interface towards the photodiode. The reading laser incident on the pits on the CD will not return to the readout system due to poor reflection and destructive interference [95]. The data storage capacity of CDs was increased by reducing

the pit size and the reading laser spot size in the optical readout system.

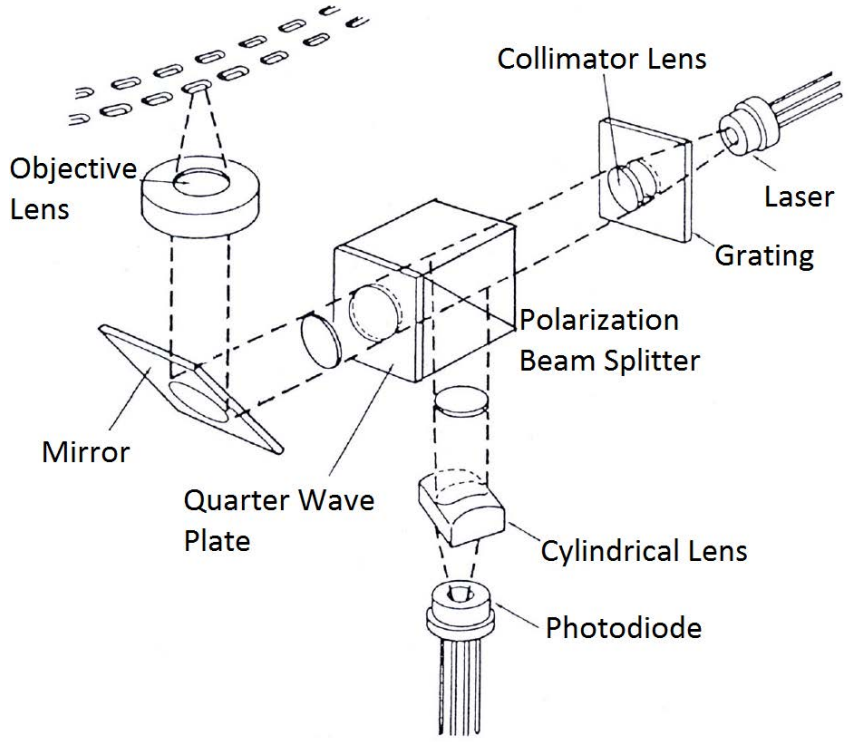

Figure 2.26: Optical readout system to retrieve stored data in CDs [94].

Other technologies have been explored for optical data storage, such as liquid crystals (LCs), photo-polymerization, photo-refractive crystals, photo-bleaching and 3-dimensional bits [96, 97]. Crystalline phase molecules are dispersed in a polymer to form LCs. These molecules are partially oriented at room temperature, known as its anisotropic phase. This orientation can be change to an isotropic phase by increasing the temperature above its glass temperature T_g or applying an external electrical field. Data is stored in LCs by localized laser heating. Similarly, data can be stored by photo-polymerization in a gel containing a monomer and a photosensitive material. Photo-induced localized polymerization changes the density of the material and consequently changes the material's refractive index. The stored optical pattern is based in this refraction index change.

Optical storage in photo-refractive crystals (e.g. Fe:$LiNbO_3$) is also based in the change of the material's refraction index. This index changes when an electric field is generated due to a space-charge in the material when a photon is absorbed and free electrons are generated.

Photo-bleaching is used for permanent data storage. A polymer block material containing a fluorophore is written by a focused high intensity laser ($\geq$ 1 mW), which decompose or bleach the flourophore preventing it to have further optical emission. A laser with less intensity ($\leq$ 1 mW) incident on the material will induce fluorescence in the areas not written.

3-dimensional bits or 3-D optical memories are based on layers of different materials. The data is stored in depth layer **Figure** 2.27 shows the schematic diagram for a 3D optical memory. Glass layers were used for permanent data storage similar to engraving [98]. Also photo-polymers, photo-refractive materials and transparent materials (glass) are used for these 3-D memories. A quantum optical data storage was reported by using a locking technique for quantum memory [99].

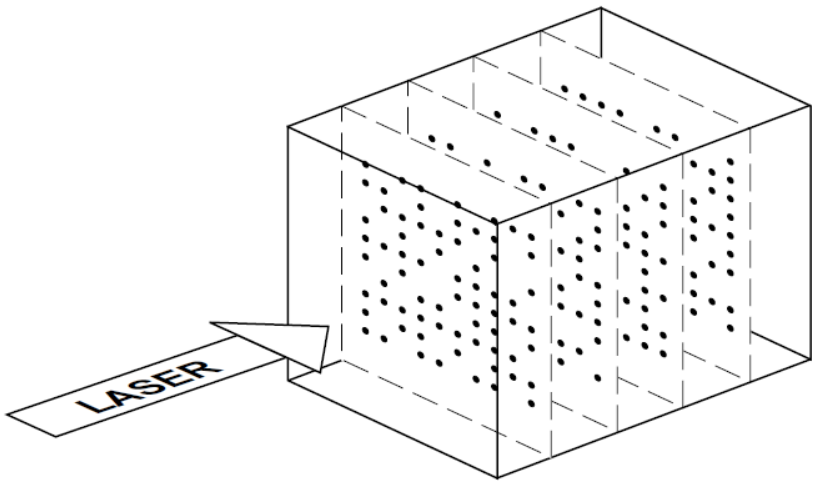

Figure 2.27: 3-dimensional memory [98].

Photochromic materials (fulgides) and electron trapping materials (Sm^{3+}-doped sulfides Ca(Sr)S and Y_2O_3) are used for optical memory [100, 101]. Moreover, chalcogenides alloys such as $Ge_2Sb_2Te_5$, Sb_xSe_{1-x}, $In_x(Sb_{70}Te_{30})_{1-x}$,$Ge_x(Sb_{70}Te_{30})_{1-x}$, $Ag_xIn_y(Sb_{70}Te_{30})_{1-x-y}$ are used as rewritable materials in phase change memories [102]. These doped $Sb_{70}Te_{30}$ alloys are commercially used materials in rewritable DVDs. $Ge_{10}Sb_{90}$ amorphous nanodots were investigated for a new generation of rewritable optical disk [103]. These $Ge_{10}Sb_{90}$ nanodots compared with $Ge_{10}Sb_{90}$ thin films reduce the thermal diffusion and show rapid

crystallization (ns range) increasing the optical memory speed. The material was written by laser-induce crystallization using 300 ps pulses. A high density memory was achieved by growing $Ge_{10}Sb_{90}$ nanodots structure. The optical memory of this phase-change material was stored in the amorphous phase to crystalline phase transition.

2.4.5 Self-sensing Feedback Technique

Self-sensing feedback technique is based on measurement and estimation of two different system parameters. One parameter is measured while another is estimated. This technique has been investigated for micro and nano manipulation using mainly in actuators for displacement and applied force control [104]. In conventional manipulation systems external sensors or embedded components are necessary to provide feedback for the control of the displacement. Manipulators and actuators displacement control can be simplified by using this self-sensing feedback technique eliminating the need for external components.

Several smart materials-based actuators have been used to implement the self-sensing technique. Actuators based on bi-layer cantilevers, piezo resistors, lead zirconate titanate (PZT), ion conducting polymer metal composite (IPMC), smart memory alloys (SMAs) and VO_2 were reported [105, 106, 107, 108, 109, 110]. This technique also named as self-sensing actuation (SSA) enables active control in these actuators by the estimation of the displacement based on a measured parameter. In the PZT based actuators the capacitance is measured, while in the other actuator the resistance is measured or sensed. **Figure** 2.28 shows the self-sensing technique used to estimate displacement in VO_2-based microactuators.

2.5 VO_2 Deposition Processes

VO_2 thin films can be deposited by chemical vapor deposition (CVP), sol-gel synthesis, atomic layer deposition (ALD) and physical vapor deposition (PVD) processes such as pulsed laser deposition (PLD), electron beam evaporation, and sputtering. The deposition condi-

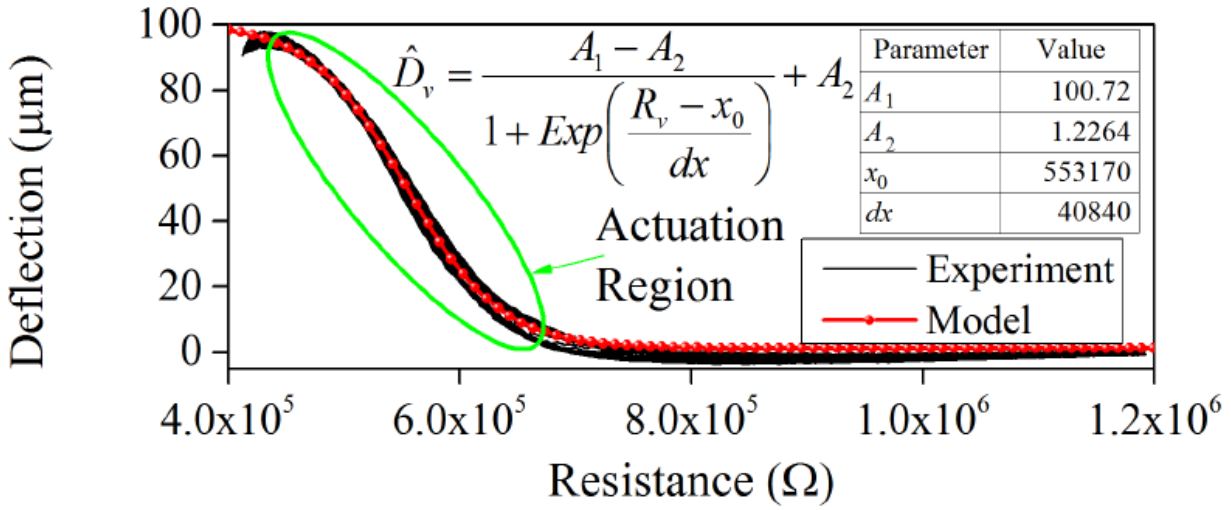

Figure 2.28: Self-sensing technique used in VO_2 to estimate deflection by sensing the resistance [111].

tions are crucial to obtain stoichiometry VO_2. It can be obtained for most deposition temperatures as shown in the vanadium oxides phase diagram in **Figure** 2.29. A mixing of the other stable vanadium oxides phases represent a challenge to grow stoichiometric VO_2.

The VO_2 thin film quality and IMT is influenced by these deposition process and the selected substrate [113]. VO_2 has been primarily deposited on sapphire (Al_2O_3), glass (Quartz, fused silica), and silicon (Si) substrates. Other substrates such as silicon nitride (Si_3N_4) [114], Germanium (Ge) [115], aluminum (Al) [116] and indium tin oxide (ITO) [117] have been investigated.

The characterization of these thin films in mainly presented by X-ray diffraction (XRD) for the 2θ angle and by Raman spectroscopy. VO_2 oriented in the 011 planes shows a strong peak around 28°. VO_2 Raman spectroscopy characteristic peaks are around 192, 224, 309, 389, 612 and 824 cm^{-1}.

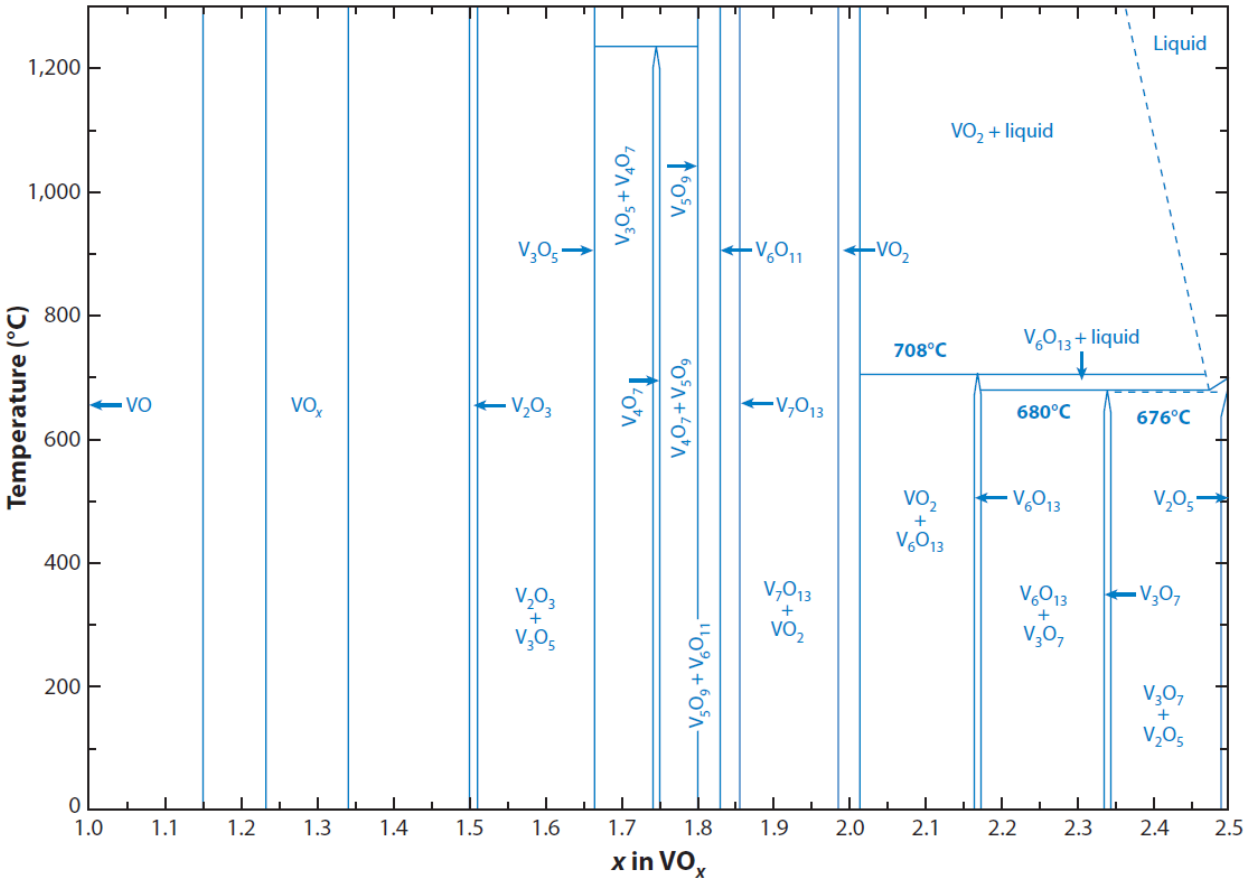

Figure 2.29: Vanadium-oxide phase diagram [112].

2.5.1 Chemical Vapor Depostion (CVD)

VO_2 thin films deposited by CVD and sol-gel synthesis involve a chemical reaction or decomposition process using a vanadium-based precursor. Similar precursors have been used for CVD and sol-gel synthesis in vapor or liquid state, respectively. Some of the used precursors are vanadium oxychloride ($VOCL_3$), vanadium acetylacetonate ($V(C_5H_7O_2)_4$) and vanadium tri-isopropoxide oxide ($VO(OC_3H_7)_3$) [118]. The deposition can be achieved at room temperature by hydrolysis followed by post annealing. CVD depositions at higher temperatures (~400 °C) often involve pyrolysis thermochemical decomposition to produce VO_2 thin films [119]. Low-pressure CVD (LPCVD), atmospheric pressure CVD (APCVD), and aerosol-assisted CVD (AACVD) have been investigated to produce these thin films [113]. **Figure** 2.30 shows XRD for VO_2 grown by CVD over Si (100) substrate. **Figure** 2.31 shows

the Raman spectra for VO_2 on glass grown by CVD.

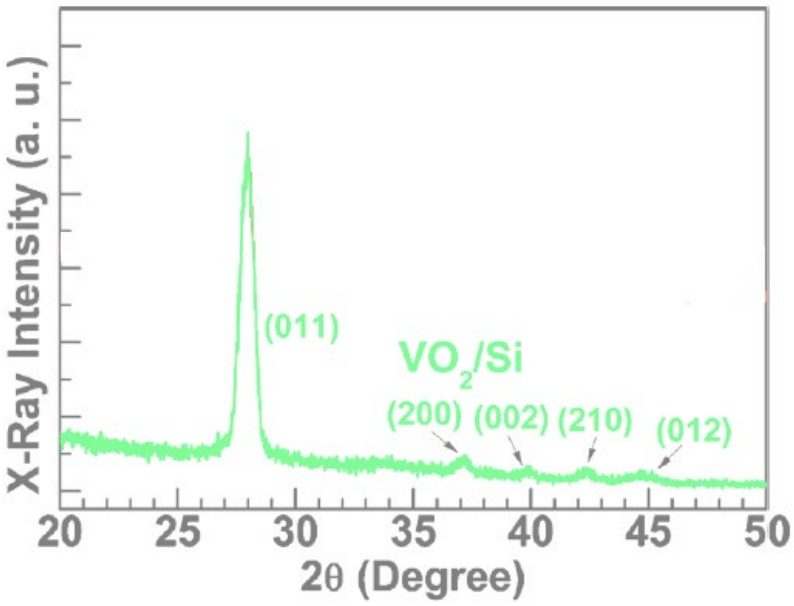

Figure 2.30: X-ray difraction for VO_2 grown by CVD over Si substrate [115].

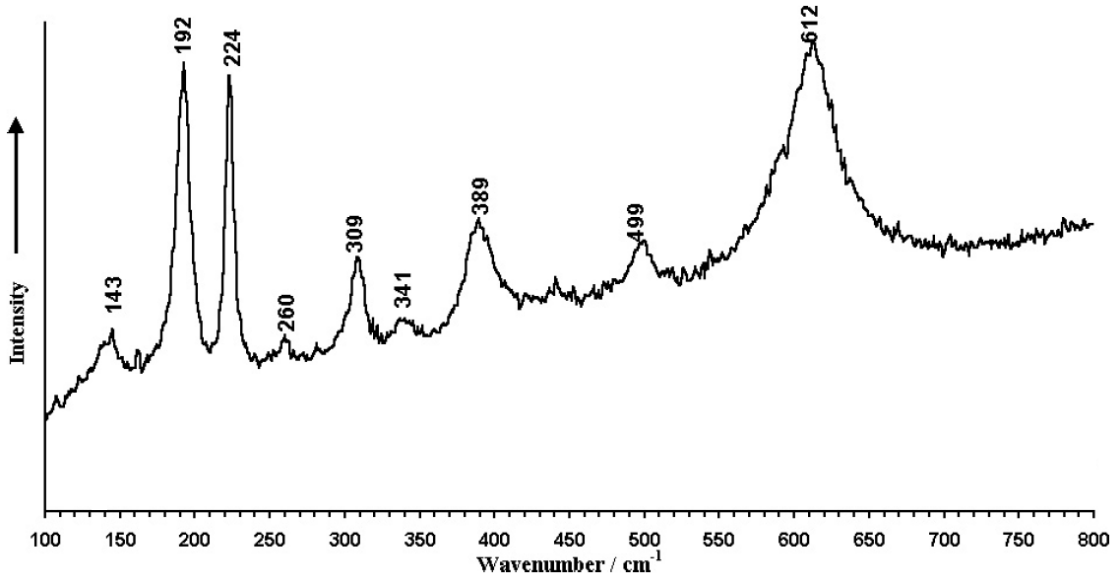

Figure 2.31: Raman spectrum for VO_2 grown by APCVD [118, 120].

2.5.2 Atomic Layer Deposition (ALD)

ALD is a surface reaction process with accurate thickness control. This process use reactant gases and vanadium-based precursors in gas or liquid state, similar to CVD. In some cases a post annealing is necessary to produce VO_2 thin films. ALD offers accurate thin film thickness control. However, this process is very sensitive to the used precursor and the deposition conditions. This makes it challenging to achieve stoichiometric VO_2 [121]. A mixing of vanadium oxide phases often occurs during these ALD depositions [122]. Also these systems are expensive compare to other deposition systems and require high maintenance.

XRD results for VO_2 deposited on glass at different temperatures are shown in **Figure** 2.32 [123]. Two different phases for VO_2 monoclinic (M and M') were observed at 400 °C. This VO_2 M' phase does not exhibit the IMT and disappears for VO_2 films deposited at higher temperature. Stoichiometric VO_2 was obtained at 475 °C using vanadium acetylacetonate as a precusor and oxygen as the reactant gas for the deposition.

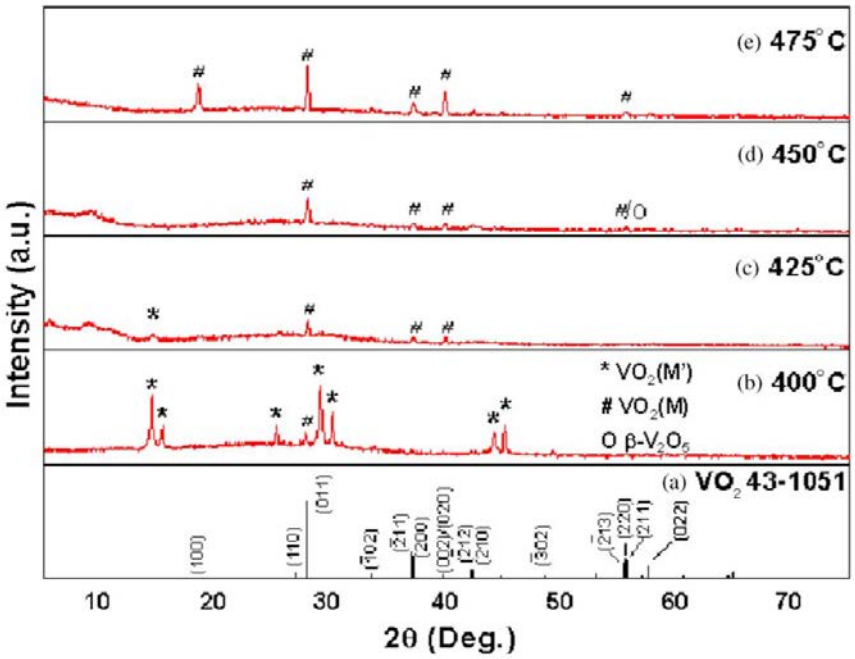

Figure 2.32: X-ray diffraction for VO_2 grown by ALD on glass substrate. VO_2 obtained at 475 °C [123].

2.5.3 Sputtering

Sputtering deposition processes include DC sputtering, radio frequency (RF) sputtering and magnetron sputtering. During this process, ionized gas hit a target removing material atoms from it. These atoms get deposited on a substrate. Magnetron sputtering can be implemented with magnetically-assisted DC or RF sputtering to improve the uniformity of the thin-film [118, 124].

Vanadium metal or vanadium oxide (VO_2, V_2O_5) target materials are used [125] with inert gas or a gas mixture (Ar-O_2) [124]. Stoichimetric VO_2 grown by this technique shows similar results as those presented for XRD, Raman spectroscopy and resistance drop.

2.5.4 Evaporation

Electron-beam and thermal evaporation processes are also used to grown VO_2 thin films. These PVD processes are very similar to sputtering. An electron beam is used to remove material from a VO_2 target or a vanadium target with Ar/O_2 gas [113, 126], while the substrate is maintained at room temperature.

Thermal evaporation deposition consists of a VO_2 thin films grown by thermal evaporation or e-beam evaporation. The substrate is maintained at room temperature during this deposition process, which is not widely used for VO_2 thin films [118]. VO_2 thin films deposited by this method show a resistance drop across the IMT of less than two orders of magnitude for Si and glass substrates [127].

2.5.5 Sol-gel Deposition

Sol-gel deposition is a wet chemical deposition process. Similarly to CVD and ALD processes it uses a vanadium-based precursors (sol) to produce VO_2 thin films.

Different V-precursors used to produce VO_2 thin films are commercially available in liquid phase such as triethoxyvanadyl, vanadium oxyacetylacetone, and vanadium isopropoxide

[128, 129, 130]. Others can be prepared with vanadium pentoxide (V_2O_5) or V powders dissolved in hydrogen peroxide (H_2O_2) to form the sol [131, 132]. Others were based on ammonium vanadate (NH_4VO_3) and vanadium tetrachloride (VCL_4) [133, 134, 135]. VO_2 thin films deposited by this process can be easily doped by adding metal powders into the precursor at its liquid state.

The V-precursor is diluted in a solvent and then synthesize to form a gel. Hydrolysis or polycondensation reactions occur during the synthesis when the V-precursor reacts with water or another metal hydroxide [136]. The synthesized gel is deposited into a substrate by dip coating, spray coating or spin coating. The substrate is heated after this deposition to remove remaining solvents from the substrate. Further thermal annealing is required to crystallize the film. This deposition method offers some advantages compare with other deposition processes: 1) low-cost, 2) relatively large area deposition 3) low deposition temperature, and feasible metal doping for VO_2 thin films [118].

This sol-gel process is sensitive to the annealing conditions. The temperature and time plays a crucial role in the crystallization process of VO_2. Several studies focused in the optimization of these annealing conditions to improve the VO_2 quality.

The XRD spectra for VO_2 thin films grown on Si (100) at different annealing temperatures are shown in Figures 2.33 and 2.34. In 2004 Pan *et al.* ([129]) reported the VO_2 crystallization starting at 550 °C on Si (100) substrates. The films were annealed for 30 min in N_2 atmosphere. Additional annealing at 600 °C for 5 min improves the VO_2 crystallization as shown in **Figure** 2.33.

Later on, Shi *et al.* ([137]) reported VO_2 crystallization at 500 °C also over Si (100) for a 150 nm thin films (See **Figure** 2.34). The annealing time was the same for all temperatures (1.5 hrs) in N_2 atmosphere with a heating rate 8 °C/min. The same year, Vinichenko *et al.* reported a study for Si and SiO_2 substrates using a layerwise spincoating method [128]. VO_2 thin films of 190 nm were grown for an annealing temperature 450 °C in Ar/H_2 atmosphere for 15 min. XRD results for this film are shown in **Figure** 2.35. VO_2 thin films with the

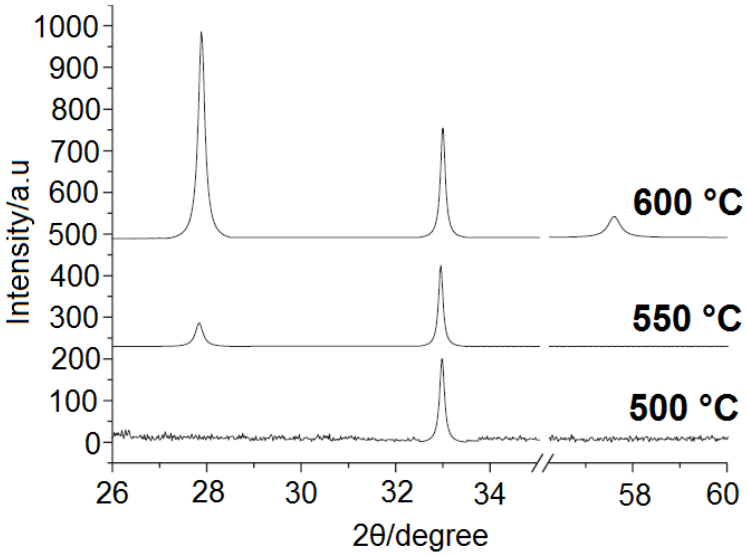

Figure 2.33: X-ray diffraction for VO_2 grown by sol-gel on Si (100) substrates at different annealing temperatures [129].

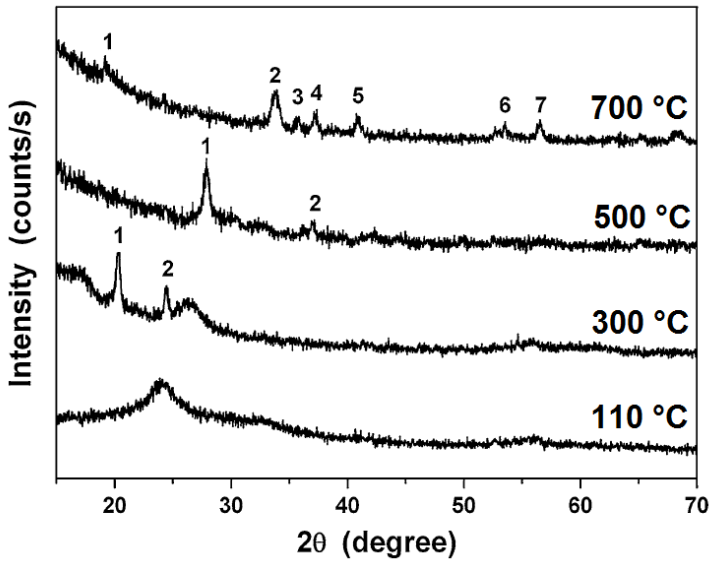

Figure 2.34: X-ray diffraction for VO_2 grown by sol-gel on Si (100) substrates at different annealing temperatures [137].

same thickness were deposited on SiO_2 by using the same process sol-gel process, annealing temperature and atmosphere. The annealing time was increased to 40 min to obtain the VO_2 stoichiometry. The results for SiO_2 films are shown in **Figure** 2.36.

Many optimized conditions are presented in the literature. However, these conditions

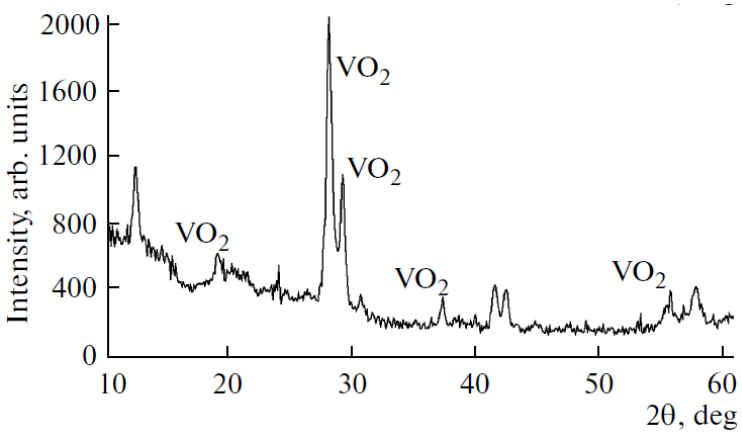

Figure 2.35: XRD results for a VO_2 thin films on Si for an annealing temperature of 450 °C for 15 min [128].

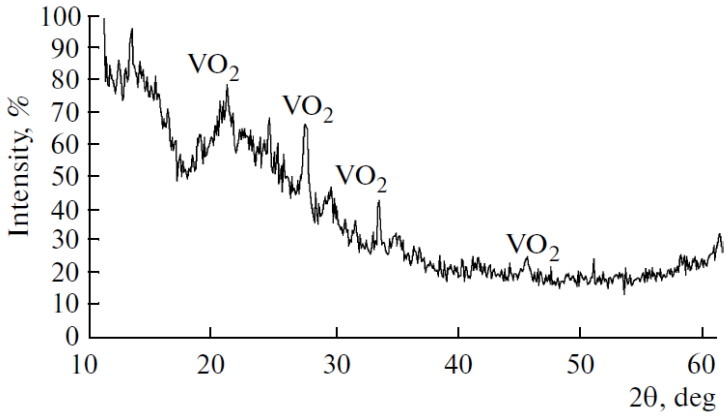

Figure 2.36: XRD results for a VO_2 thin films on SiO_2 for an annealing temperature of 450 °C for 40 min [128].

varied for each system and the selected substrate. These results demonstrate the importance to optimize the annealing conditions for when using sol-gel process.

VO_2 thin films grown by sol-gel are porous compare with other deposition methods. **Figure** 2.37 shows the topography for the VO_2 film of 2 x 2 μm area from Shi *et al.* results [137].

SEM is used to evaluate the thickness of these films [138]. **Figure** 2.38 shows a cross-section measurement of a VO_2 thin film. Profilometer is not the prefer method to measure sol-gel grown thin films due to the roughness and topography characteristic of these films.

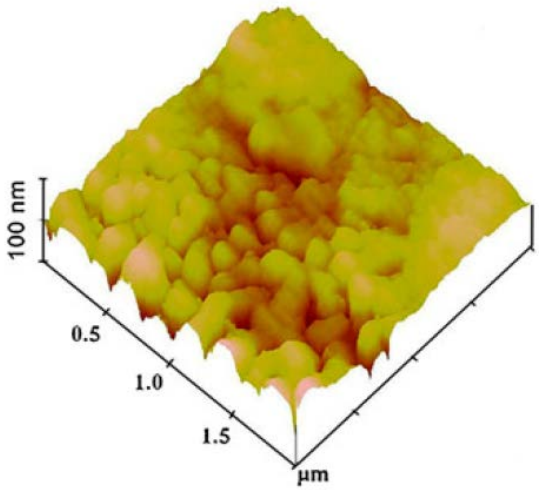

Figure 2.37: AFM topography of VO_2 thin films by sol-gel on Si (100) [137].

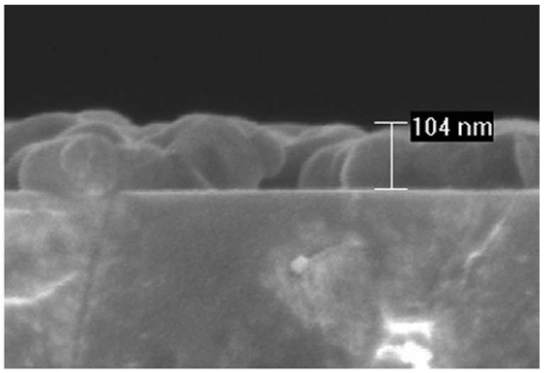

Figure 2.38: Thickness measurement of VO_2 thin films using SEM cross-sectional imaging [138].

2.5.6 Pulsed Laser Deposition (PLD)

Pulsed laser deposition (PLD) is another PVD process, which is suitable for oxides deposition[118]. This process is based on laser ablation, where an excimer laser (ArF,KrF,XeCl) is focused into a rotating target (V, V_2O_3) [139, 140, 141]. Material is remove from this target and deposited into a substrate located opposite to this target as shown in **Figure** 2.39. Ar/O_2 gas mixture or O_2 gas are used for this process. The substrate is maintained at a certain temperature during the deposition, usually at elevated temperatures [118]. Often this deposition is followed by a post annealing step to obtain stoichiometric VO_2.

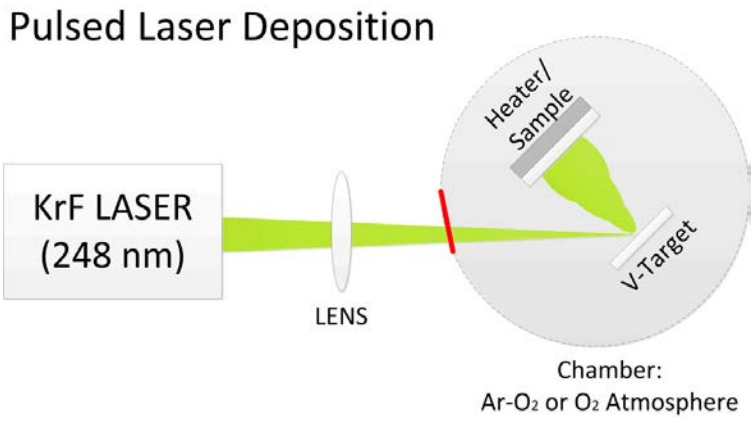

Figure 2.39: Schematic for a PLD system [118].

The substrate temperature for VO_2 thin films ranged from room temperature to ~630 °C [142, 143, 139]. VO_2 thin films were deposited at a substrate temperature of 520 °C with 90 mTorr of Ar/O_2 gas pressure. These conditions were used to deposit VO_2 thin films on Si, SiO_2 and Al_2O_3 substrates. **Figure** 2.40 shows the XRD spectra for these substrates.

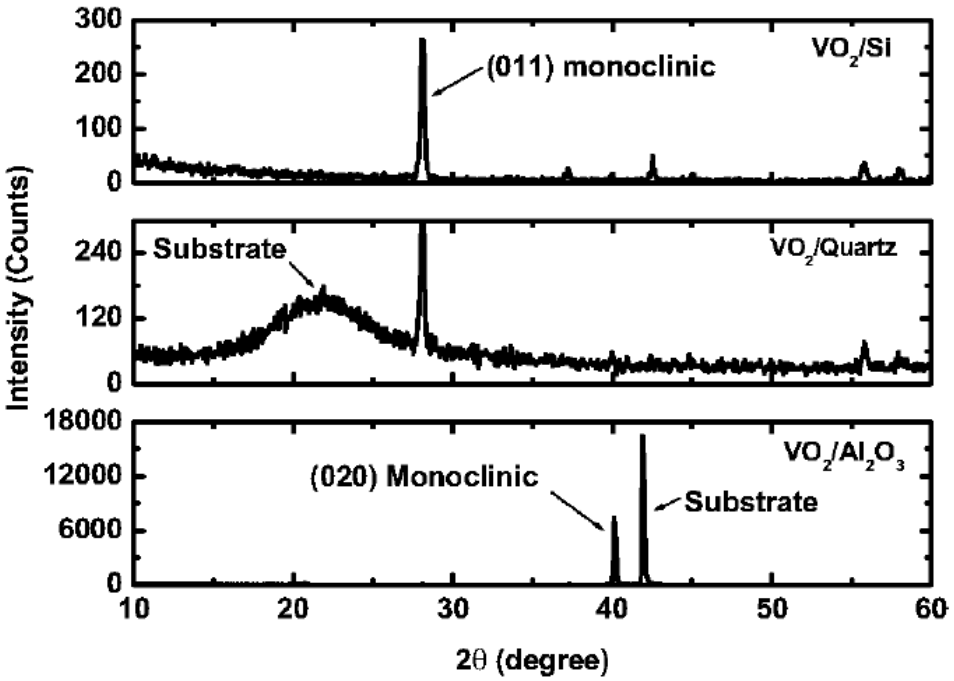

Figure 2.40: XRD spectra for VO_2 thin films over Si (100), SiO_2, and Al_2O_3 by PLD [141].

During this substrate study Soltani *et al.* found that the thermochromic properties of VO_2 were not affected by the selected substrate when using the same deposition conditions

[141]. Moreover, Kim *et al.* showed a resistance drop of 4^{+} orders of magnitude for VO_2 thin films growth on Al_2O_3. These thin films were deposited at 630 °C with 30 mTorr of O_2 pressure with no annealing [139].

Marvel *et al.* studied the influence of three deposition processes (including PLD) on different substrates: Si (100), SiO_2 and Al_2O_3 (0001) [113]. Amorphous VO_2 thin films were deposited on these substrates at room temperature with a pressure of 11 mTorr of O_2. These films were annealed at 450 °C with 25 mTorr of O_2 for time intervals of 2, 5, 10, 30, and 90 min. Highly oriented VO_2 thin films resulted after this crystallization/annealing step. Raman spectra for VO_2 films over Si (100) and SiO_2 are shown in **Figures** 2.41 and 2.42, respectively. VO_2 films start to crystallize on Si substrates after 5 min. It shows the strongest peak around 640 cm^{-1} for a 30 min annealing. A mixing of vanadium oxides phases occurs for SiO_2 substrate when deposited after 5 min. **Figure** 2.43 shows the optical transition of a VO_2 thin film over SiO_2 substrate annealed for 5 min [113].

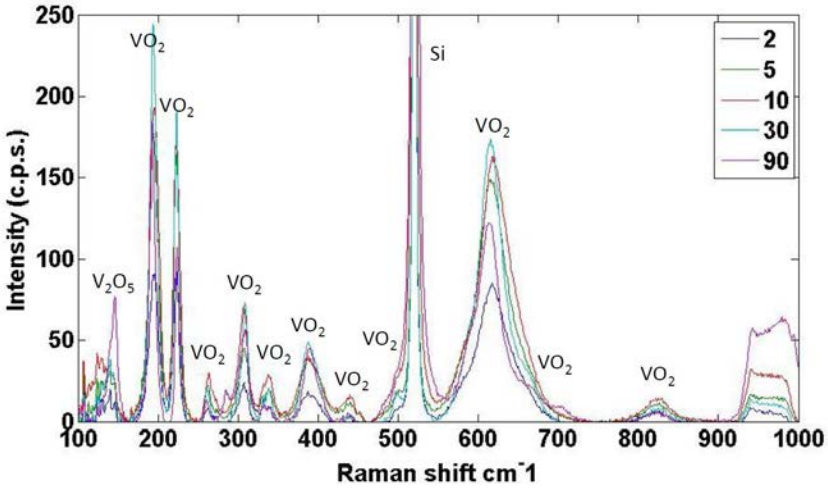

Figure 2.41: Raman spectra for VO_2 thin films on Si (100) substrate for different annealing times (2, 5, 10, 30, and 90 min). VO_2 strong peaks shown for the 30 min data [113].

These substrates were compared for its optical hysteresis contrast as a figure of merit for the study. **Figure** 2.44 shows how Al_2O_3 outperforms among Si and SiO_2 substrates.

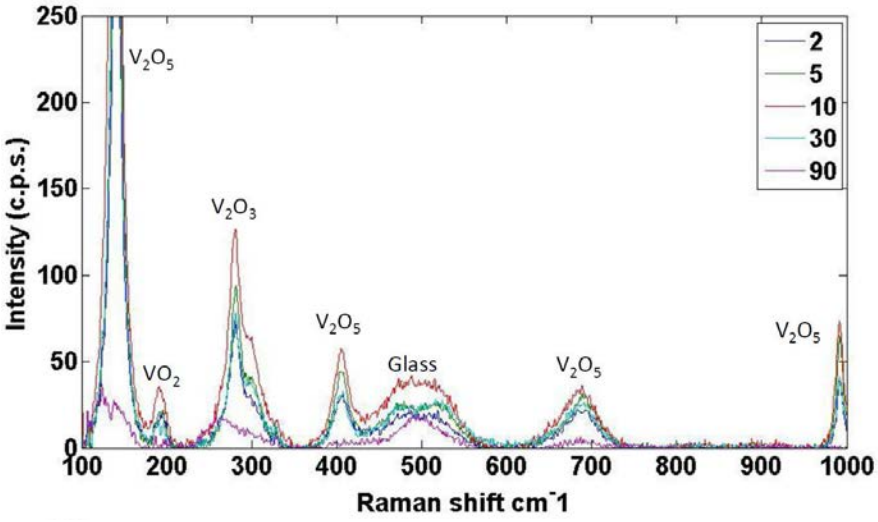

Figure 2.42: Raman spectra for vanadium oxides on SiO_2 substrate for different annealing times: 2, 5, 10, 30 and 90 min [113].

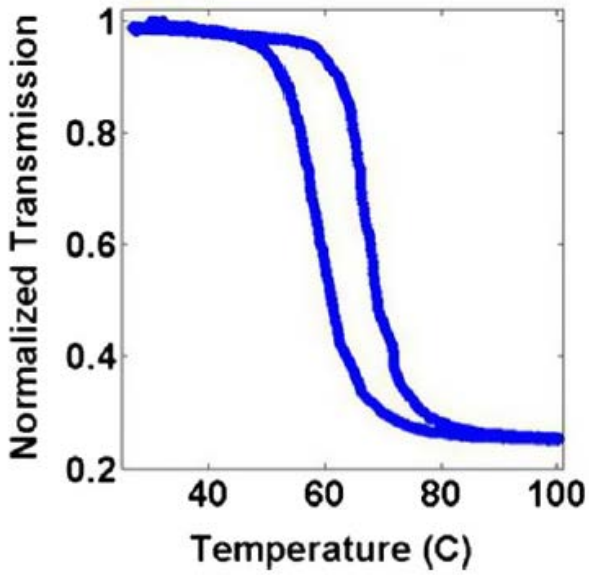

Figure 2.43: Optical transition of VO_2 over SiO_2 for 1550 nm [113].

2.6 Summary

In this chapter, a background on infrared image projectors, electronically controlled variable optical attenuators and VO_2 was presented. Electro-optical materials suitable for infrared

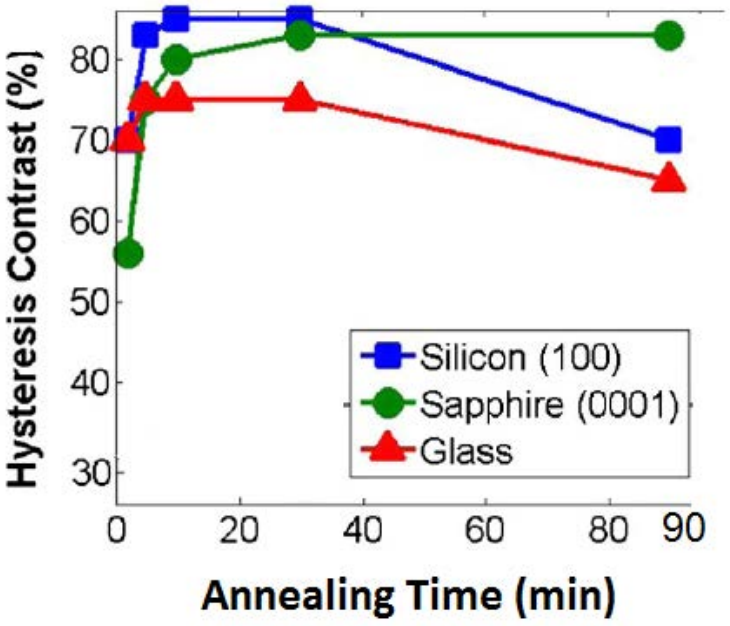

Figure 2.44: Hysteresis contrast for PLD deposited VO_2 thin films on Al_2O_3, Si and SiO_2 [113].

applications were discussed with the devices. Three operation technologies were discussed for images projectors (transmissive, reflective and emissive). Solid-state, MEMS and liquid crystal based devices were discussed as electronically variable optical attenuators. Attenuation control was discussed as a key parameter for optical system integration. The transition behavior for the electrical, structural and optical properties of VO_2 was discussed. A background on optical memory devices and some optical storage materials was provided. VO_2 thin film deposition processes were presented with emphasis in sol-gel synthesis and pulsed laser deposition (PLD). The following chapters present the VO_2 deposition processes; the optical memory of VO_2 and its application for infrared image projectors; and variable optical attenuator with self-sensing control based on the VO_2 electro-optical correlation.

CHAPTER 3

VO_2 THIN FILMS DEPOSITION

VO_2 thin films were grown by pulsed laser deposition (PLD) and sol-gel synthesis. PLD deposition system allows for depositions on substrates as large as 2 inches in diameter. Sol-gel process was investigated to deposit VO_2 in substrates as large as 4 inches in diameter. The investigated method minimized the precipitates formed during the sol-gel synthesis, thus reducing the film's cracks formation as the solvent evaporates. Different solvents, concentrations, substrates, dying methods, and annealing conditions were investigated. VO_2 was successfully grown on fused silica quartz $1.6\,cm^2$ square substrates (1 mm thick) and SiO_2/Si(100) (1/500 μm thick) 4 inches wafers. The VO_2 thin films were characterized by x-ray difraction (XRD), Raman spectroscopy, atomic force microscope (AFM), scanning electron microscope SEM, and a surface profilometer. The electrical and optical properties were investigated.

3.1 Sol-gel Deposition Process

Vanadium(V) triisopropoxide oxide precursor (VTOP, Alfa aesar 96 %, $VO(OC_3H_7)_3$) was used as the sol for this synthesis. Anhydrous methanol was added to the VTOP sol to help with the solubility of the solution and to control the viscosity of the gel. Distilled (DI) water was added as final catalyst component into the solution to induce the gelation process. The formed aqueous gel was spin coated into SiO_2 and SiO_2/Si substrates. The excess of solvent on the film was removed by a drying step on a hotplate. The samples were annealed at one step using a tube furnace to crystallize the V_2O_5 thin film and promote its reduction into VO_2. The overall reaction of this synthesis,

$$2\,VO(OC_3H_7)_3 + 3\,H_2O \longrightarrow V_2O_5 + 6\,OHC_3H_7$$

is based on hydrolysis reaction by adding H_2O. Amorphous V_2O_5 and solvents are the by products of this reaction. After removing the excess of solvent OHC_3H_7 with the drying step the remaining V_2O_5 is crystallized and reduced to VO_2.

$$V_2O_5 \longrightarrow 2\,VO_2 + \tfrac{1}{2}\,O_2$$

A diagram of the used process is shown in **Figure** 3.1.

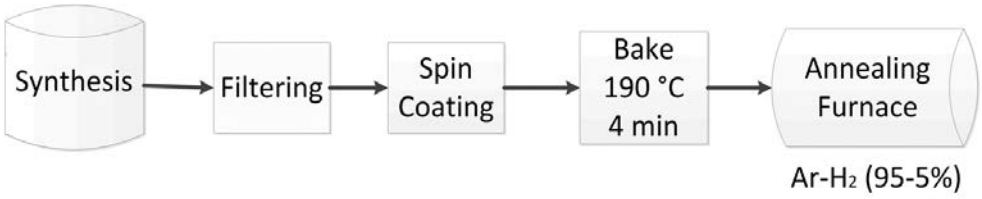

Figure 3.1: Summarized sol-gel process used to deposit VO_2 thin films.

3.1.1 Substrate

VO_2 thin films with thickness of approximately 100 nm were grown on 5 cm^2 and 4" substrates of SiO_2. Square fused silica quartz substrates with surface area of 0.5 x 0.5 inches and thickness of 1 mm were used to determine the process for growing VO_2. In order to make the process compatible with standard microfabrication process, 4" substrates were used. A 1 µm layer of SiO_2 was deposited by low thermal oxidation (LTO) process over a 4 inches diameter Si wafer (SiO_2/Si). These substrates were cleaned in acetone and methanol with ultrasonic bath. The 4" wafer was cut into four pieces to analyze the uniformity of the VO_2 thin film. **Figure** 3.2 shows the resulted films. Hereinafter, piece A, B, C and D of the SiO_2/Si substrate.

3.1.2 Synthesis

Different solvents were examined at the same concentration to consider the precipitates formed. The solvent was determined empirically based on the observed behavior of the solution. The solutions were prepared with 624 mg of VTOP, having a concentration of

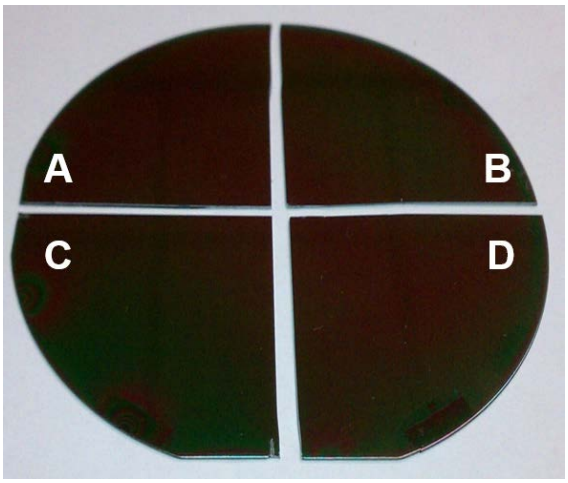

Figure 3.2: $VO_2/SiO_2/Si$ wafer cut into piece A, B, C and D for further characterization.

0.38M. The solvents were added at approximately the same rate to avoid stirring up the solution. Table 3.1 describes different solvent behavior. Anhydrous methanol was selected based on these experiments.

Table 3.1: Solvent effect on gel precipitates formation.

Solvent	Observed behavior
Isopropanol	Precipitates formed instantly. Solid layer formed.
Acetone	Highly viscous gel formed quickly, gel not suitable for spinning.
Ethanol	Precipitates were formed, non homogenous gel.
Methanol	Aqueous homogenous solution. Last for 1 h before a viscous gel formed.
Anhydrous methanol	Same homogeneity as methanol, repeatable results after the annealing process.

The gel viscosity varied with the solvent concentration. High solvent concentrations produced aqueous gel, a viscous gel was achieved by decreasing the concentration. Different anhydrous methanol concentrations were examined in order to have an aqueous gel that spread uniformly during the spin coating. The concentration of methanol was varied from 60, 65, 70, 75, and 80 % of the initial volume (4.3 mL). Precipitate-free solutions (to the naked eye) were achieved with 70 %.

3.1.3 Gel Deposition

The gel was filtered with a 0.45 µm and 5 µm pore size Millipore filters. The 0.45 µm filters were saturated due to a small output opening while covering a large area. 5 µm filters demonstrated to improve the uniformity of the film compared with no filtering, as seen under the microscope.

The gel was spin-coated on the substrates. The spinning process consisted of two steps: spreading the solution at low speed to cover uniformly the entire area, and spinning at higher speed to have a uniform thickness. The gel was spread for 5 s at 600 rpm, followed by a spinning at 2,000 rpm for 30 s.

3.1.4 Drying Treatment

A drying treatment followed the deposition to evaporate the solvents by-products of the synthesis reaction. Two methods were evaluated: IR drying and hot plate baking. In this step was important to determine if there is an effect on the film whether the film is heated from top or bottom. The temperature on the substrate was calibrated using the same thermocouple for both methods. Two samples were deposited and tested under the same heat treatment for 4 min at 190 °C. A custom-built IR dryer was used. This sample showed degradation and discontinuous spots. The rest of the experiments were carried using a hot plate to dry all the samples.

3.1.5 Annealing

The annealing conditions were studied initially for SiO_2 substrates. 0.5" x 0.5" samples were annealed in a tube furnace under reducing atmosphere with Ar-H_2 (95-5%) gas flux. The temperature heating rate was ∼10 °C/min for all the cases to avoid crack formation. The cooling rate was not controlled, and the heaters were turned off at the end of the annealing. The temperature was controlled using Labview software to ensure a repeatable process with

accurate annealing time. The substrate temperature was calibrated with respect to the controller temperature. The temperature presented is the substrate temperature.

A background pressure between $1x10^{-4}$ Torr and $7x10^{-5}$ Torr was reached before increasing the temperature. The annealing temperature, pressure, and time were studied.

Samples were annealed at 500 °C and 37 mTorr for 1, 1.5, 2, 3, and 4 hours. **Figure** 3.3 shows the resistance as a function of temperature curves using a heat rate of ∼0.4 °C/s for the measurable samples. The 4 hour annealing process degraded the sample. An annealing time of 2 hours was chosen as the optimum time for further processing. This sample showed hysteretic curve with a noticeable resistance drop from 383.6 kΩ to 13.8 kΩ, having ∼1.4 orders of magnitude drop.

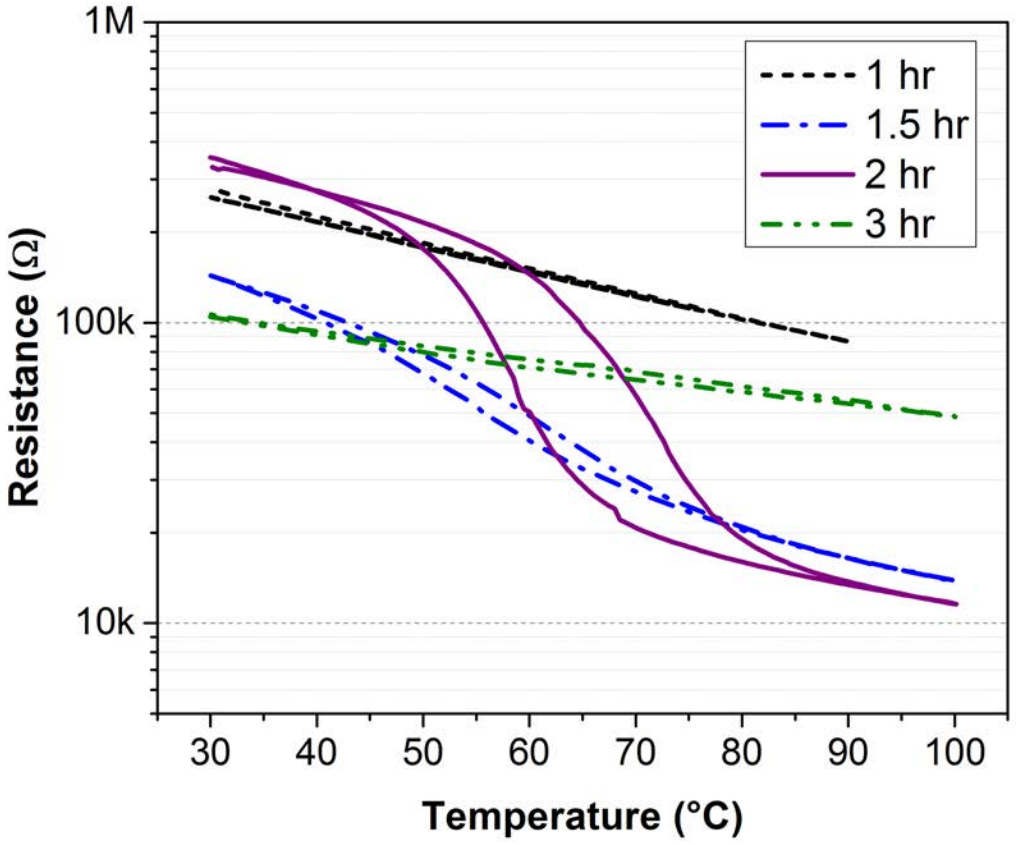

Figure 3.3: Annealing at 500 °C varying the annealing time.

Based on these results, the annealing temperature was studied for the same pressure (37 mTorr), but all with the same annealing time of 2 hours. The temperature range studied went from 336 °C to 558 °C. **Figure** 3.4 shows resistance curves from 400 °C to 558 °C. 400 °C sample is almost metallic. Approximately 2^{+} order resistance drop is observed for the sample annealed at 428 °C. The resistance drop decreases as the annealing temperature increases.

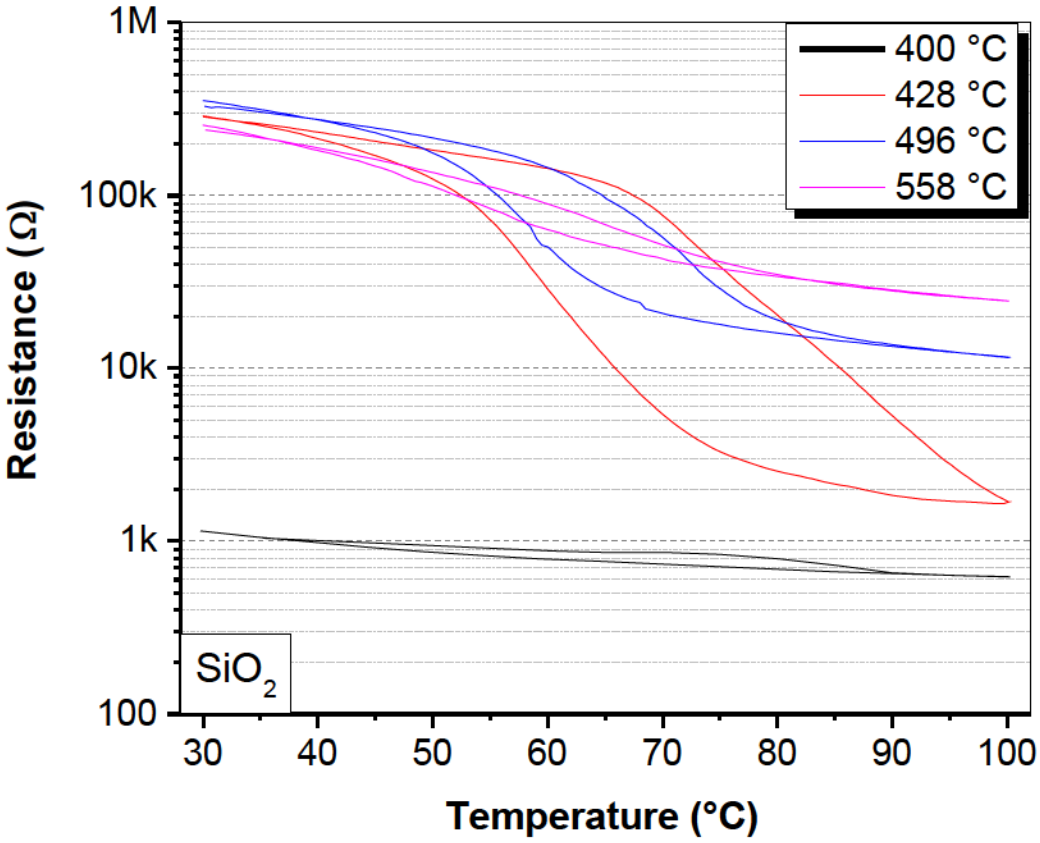

Figure 3.4: Annealing temperature study on SiO_2 from 400 °C to 558 °C.

Additional samples were annealed at temperatures near to 400 °C. The annealing temperature was studied from 417 °C to 496 °C. Thin films with a resistance drop of 1.5^{+} orders resulted for these films as shown in **Figure** 3.5. Not all curves considered during this study are shown in this figure, for clarity.

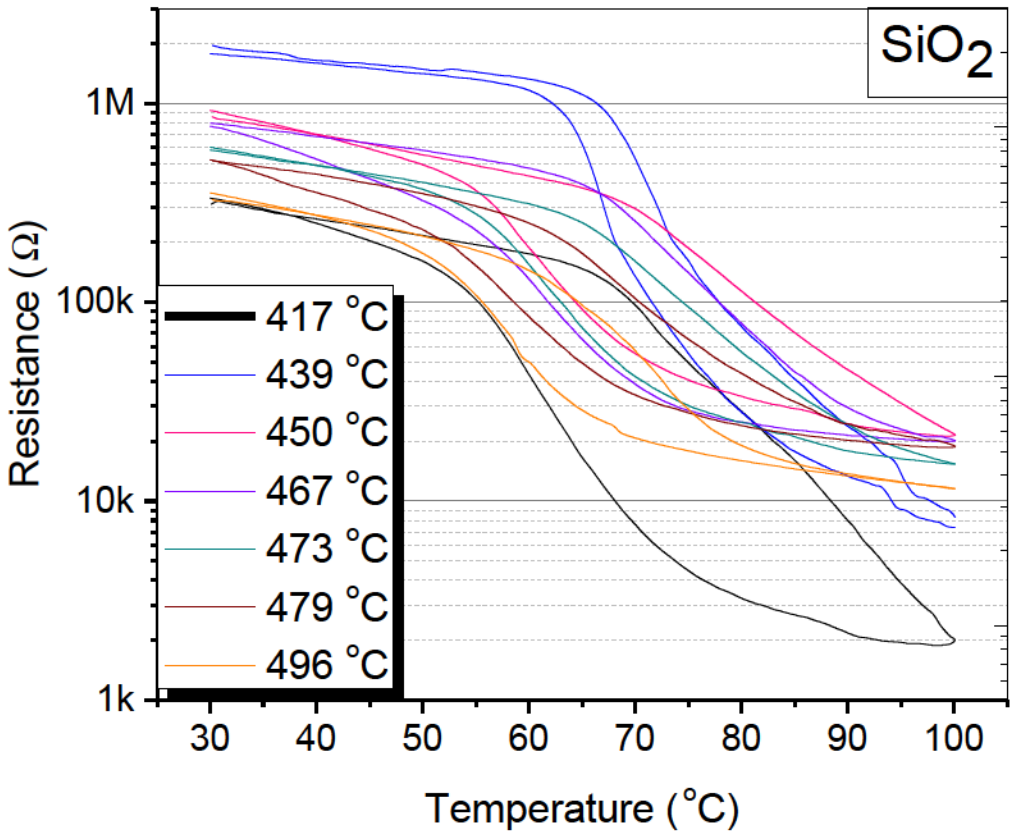

Figure 3.5: Annealing study on SiO_2 for a temperature range of 417 °C to 496 °C.

SiO_2/Si substrates were annealed with these conditions: 439 °C at 37 mTorr for 2 hrs. A temperature of 439 °C at the sample corresponds to 600 °C at the temperature controller. **Figure** 3.6 show the results for the study in SiO_2/Si. The annealing conditions were modified to accommodate this different substrate. The pressure was reduced to 15 mTorr and the temperature raised to 461 °C, thus requiring a stronger reducing environment with lower pressure and higher temperature compared to SiO_2 samples. Another Si/SiO_2 sample annealed at 473 °C showed metallic behavior.

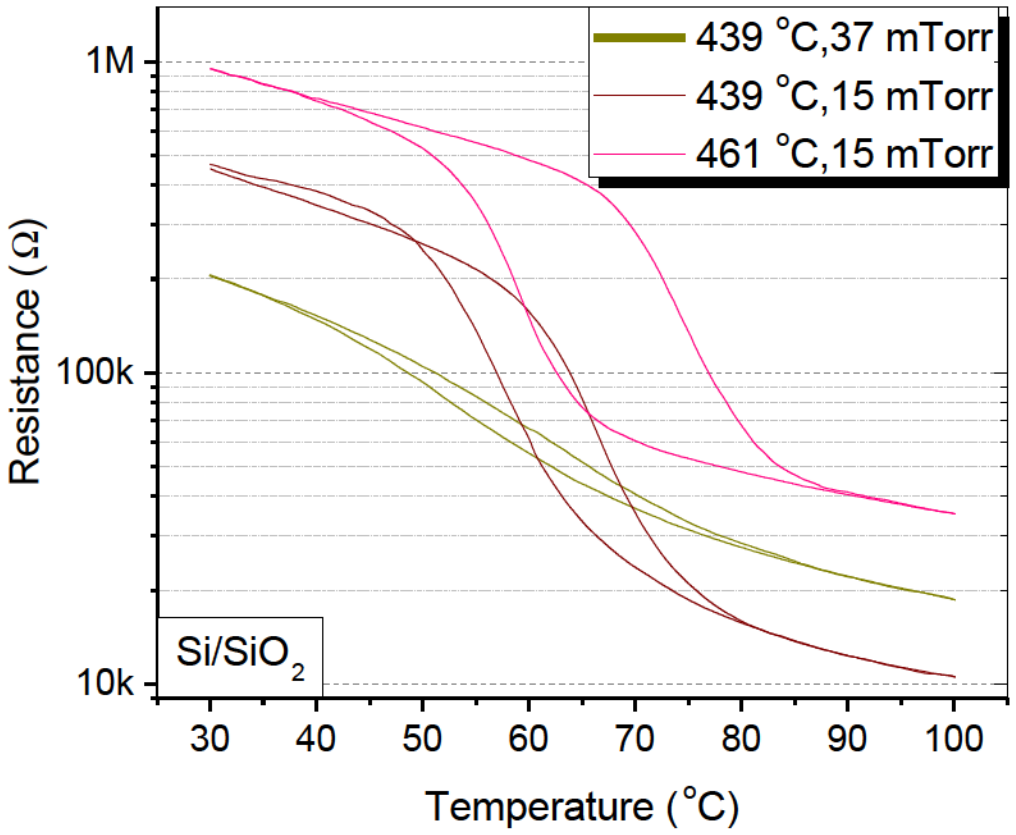

Figure 3.6: Annealing conditions variations in SiO_2/Si substrates.

Considering the results from the previous study, 4" wafers were annealed at 461 °C, 15 mTorr for 2 hours with repeatable results. **Figure** 3.7 shows resistance curves for VO_2/SiO_2/Si pieces A, B, C and D previously shown in **Figure** 3.2.

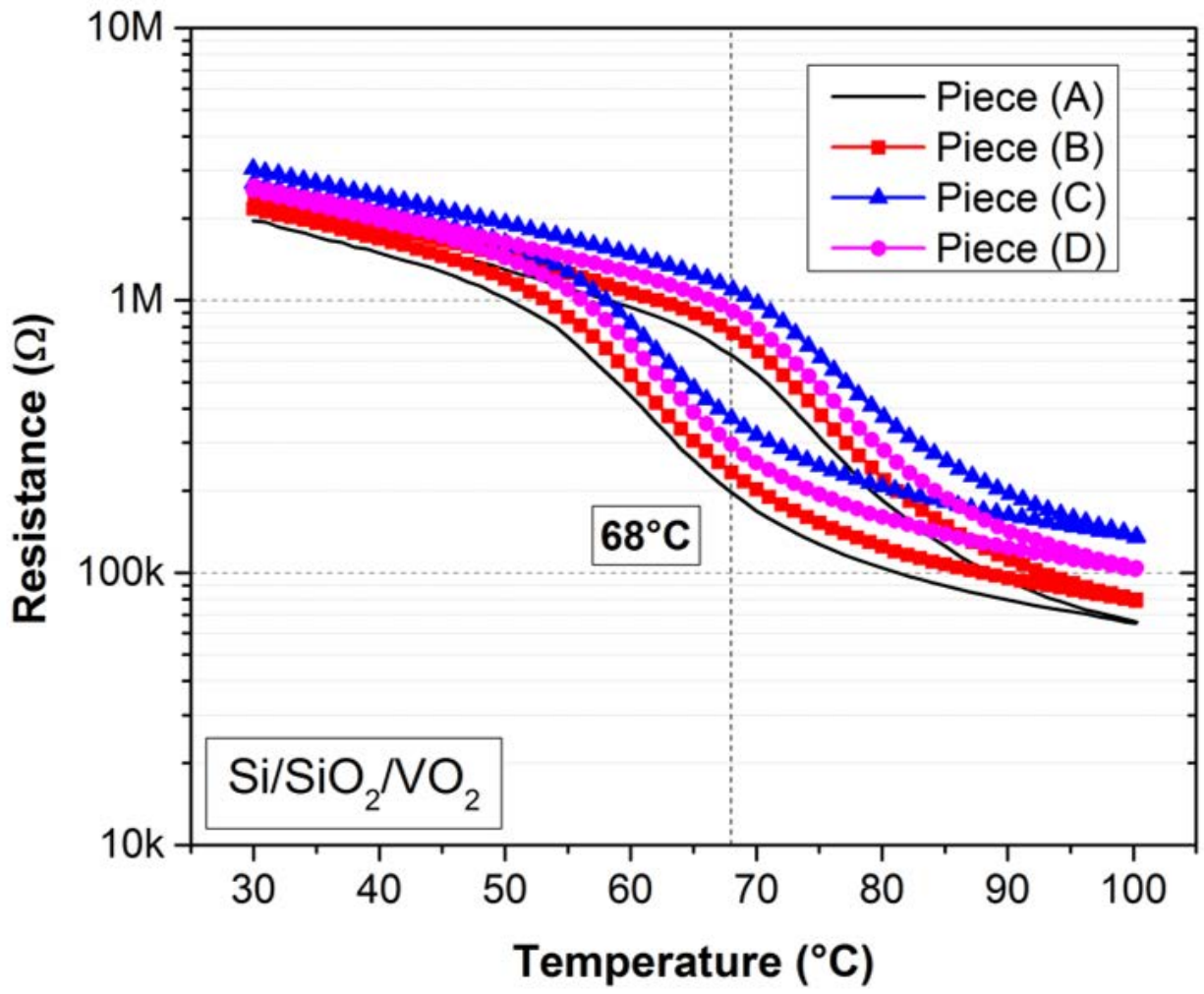

Figure 3.7: Electrical characterization of $VO_2/SiO_2/Si$ the wafer pieces A, B, C and D.

3.2 Characterization of VO_2 deposited by sol-gel

The VO_2 thin films grown by sol-gel method were characterized to investigate its composition, topography, uniformity, electrical transition, and optical transmission.

3.2.1 Electrical Transition

The phase transition was first characterized by the drop in electrical resistance. The results for this characterization at different annealing times was presented in the previous section.

The characteristic hysteretic behavior of VO_2 was observed as the temperature of the film was varied at ~0.4 °C/s across the phase transition temperature. The resistance drop around 68 °C and the typical hysteretic behavior are an indication of VO_2 film.

3.2.2 Composition

The composition and orientation of the VO_2 thin films were investigated by XRD and Raman spectroscopy. XRD measurements were performed using a Bruker-AXS High Resolution X-ray diffractometer. **Figure** 3.8 shows the spectra for the films deposited on Si and SiO_2/Si substrates. The substrate background was removed from the spectrum. The VO_2 characteristic peak around 28° is observed for both samples. These results demonstrate some level of crystallization in the sol-gel deposited VO_2 thin films.

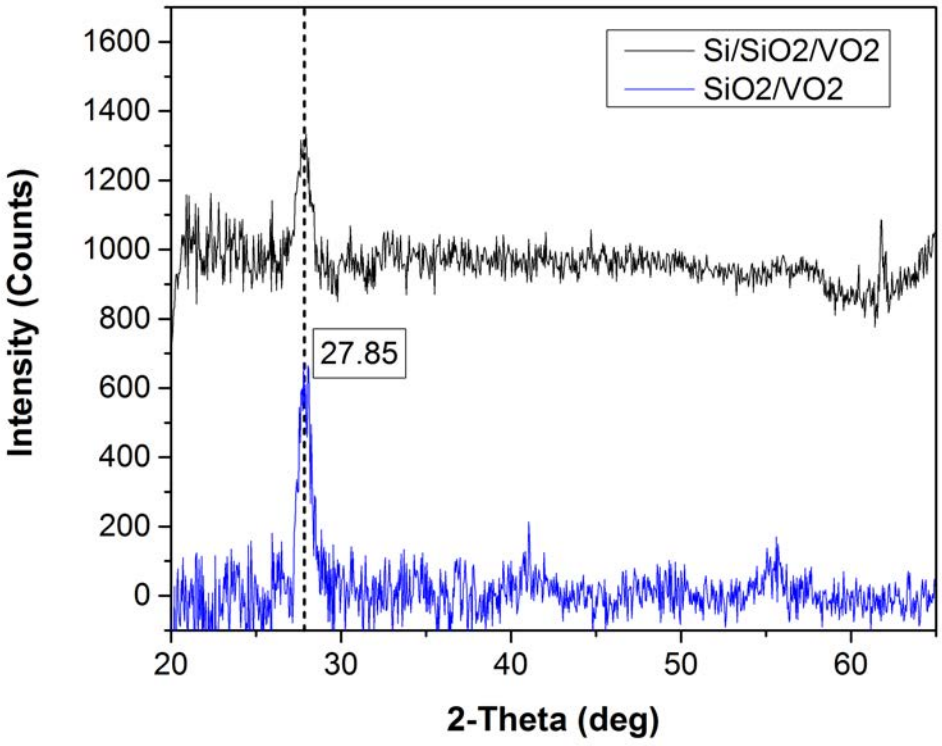

Figure 3.8: XRD characterization of VO_2/SiO_2 sample annealed at 428 °C for 2 hrs at 37 mTorr and VO_2/SiO_2/Si sample annealed at 461 °C for 2 hrs at 15 mTorr.

Raman spectroscopy was measured using with a wavelength of 532 nm. Thin films deposited on SiO_2 and annealed at 417 °C, 428 °C and 450 °C were evaluated. Also films deposited on SiO_2/Si substrates for 406 °C, 439 °C and 461 °C. VO_2 characteristic spectrum was obtained at 417 °C for SiO_2 substrates. A mixing of vanadium oxides phases appears as the temperature increases similar to those presented in **Chapter 2**. See **Appendix A: Composition study for VO_2 thin films by sol-gel** for these results.

For SiO_2/Si substrates, the VO_2 characteristic spectrum is showed at an annealing temperature of 461 °C for 2 hours and 15 mTorr. At temperatures higher than 461 °C VO_2 was observed to crack and degrade. Samples evaluated below this temperature showed a reduction from V_2O_5 phase as the annealing temperature increases. However, for SiO_2 substrates a mixing of V_2O_3 and V_2O_5 phases was observed as the annealing temperature increases. These results demonstrate the importance of surface conditioning and substrate selection during sol-gel processing. During the annealing process the thin film is reduced by the conditions (temperature, pressure, and purging gas) but it could recover oxygen at the interface with the substrate.

Figure 3.9 shows the VO_2 thin films Raman spectrum for SiO_2 (left) and Si/SiO_2 (right) substrates.

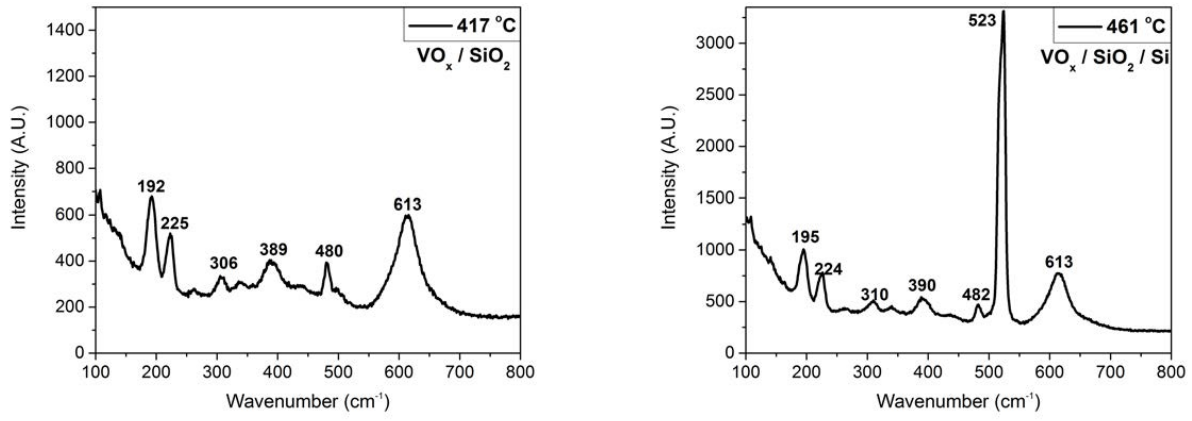

(a) (b)

Figure 3.9: Raman spectroscopy characterization of a) VO_2/SiO_2 sample and b) VO_2/SiO_2/Si sample.

3.2.3 Topography

The films topography was investigated by using a contact surface profilometer (NanoMap-500LS) for a 5 mm x 5 mm area. A stylus force of 25.68 mg was applied during the surface scanning. **Figure** 3.10 shows the topography for piece "A" of the SiO_2/Si wafer. Similar results were obtained for other pieces. The vertical resolution of the used contact surface profilometer is 0.1 nm for an ideal environment. AFM was considered to characterize these films at smaller scale.

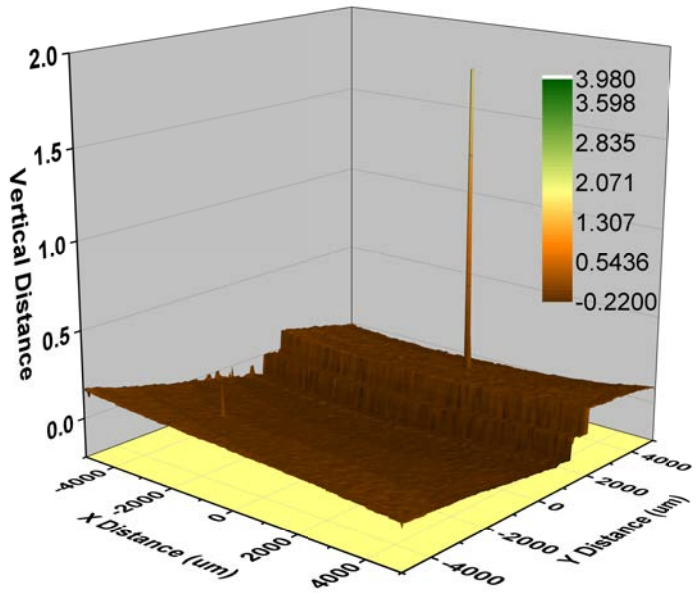

Figure 3.10: VO_2 thin film topography measured with the 3-D surface profilometer.

An AFM system was used to investigate the topography and roughness of VO_2 thin film for pieces A, B, C and D. A square area of 5 μm x 5 μm was measured at approximately the same radial distance. The average roughness for each piece were 27.2, 42.6, 33.57, and 32.8 nm, respectively. **Figure** 3.11 shows these measurements. A smaller area of 1 μm x 1 μm square region was investigated, see **Figure** 3.12.

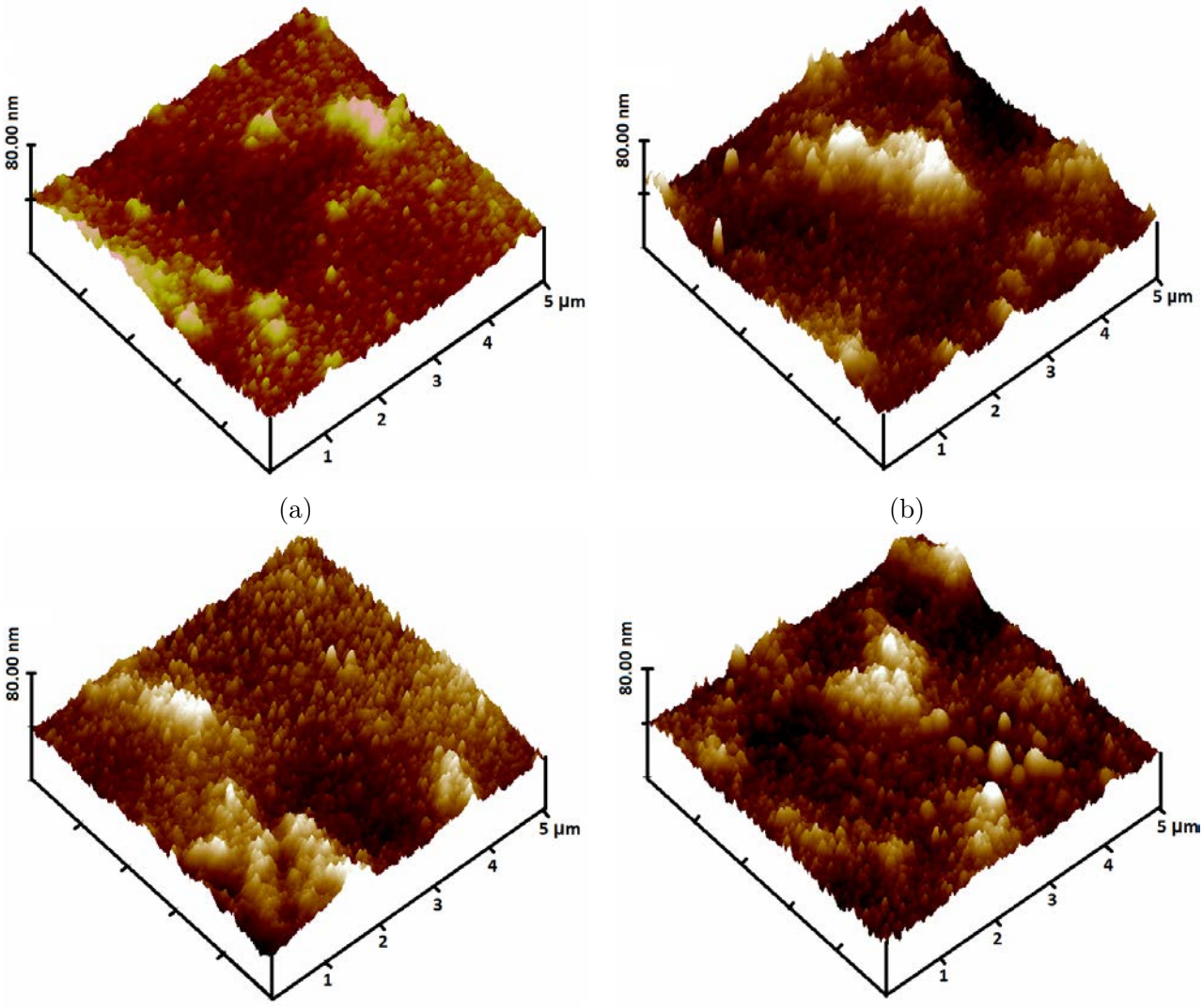

Figure 3.11: Atomic forced microscope (AFM) surface characterization for $VO_2/SiO_2/Si$.

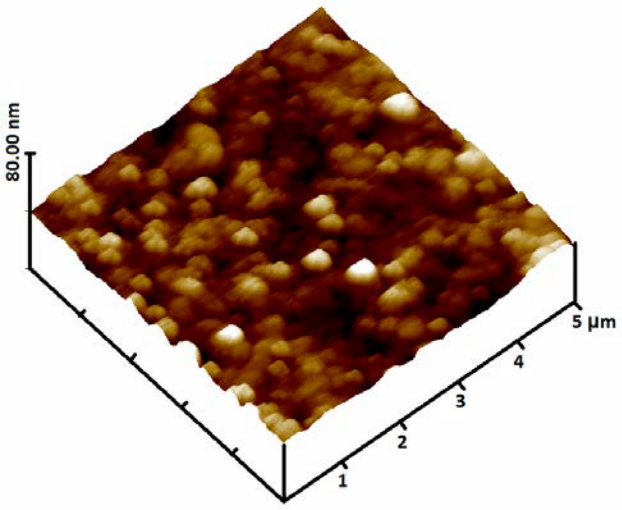

Figure 3.12: AFM surface topography for $VO_2/SiO_2/Si$ substrate measured in a 1 μm x 1 μm square area.

3.2.4 Thickness

Thickness of the film was measured by the surface profilometer (same described above) before annealing (amorphous V_2O_5). **Figure** 3.13 shows a ~200nm step. The thickness of this film slightly decreases after the annealing step. SEM was used to assist with this thickness measurement on the film after the annealing.

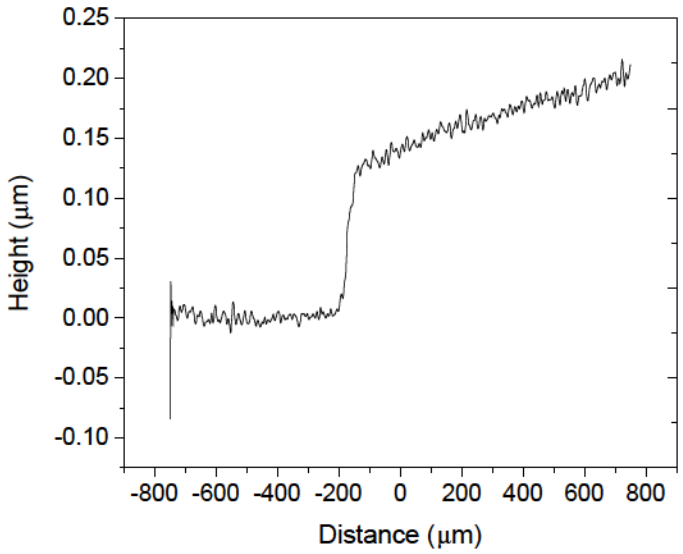

Figure 3.13: Thickness measurement.

SEM and focused ion beam (FIB) were used to measure the film's thickness after annealing. The thin film was cut into a trapezoidal shape to reduce material build-up at the edges as shown in **Figure** 3.14. Each piece of the 4" wafer was measured at the center of the piece. **Figure** 3.15 shows the results for all sections.

3.2.5 Optical Transition

The optical transmission of VO_2 films grown by sol-gel on SiO_2 was measured using the setup described in **Section 4.3**. The transmission was measured for λ=1550 nm. The results shown in **Figure** 3.16 were normalized with respect to its maximum transmission at room temperature. A 70 % transmission drop was observed.

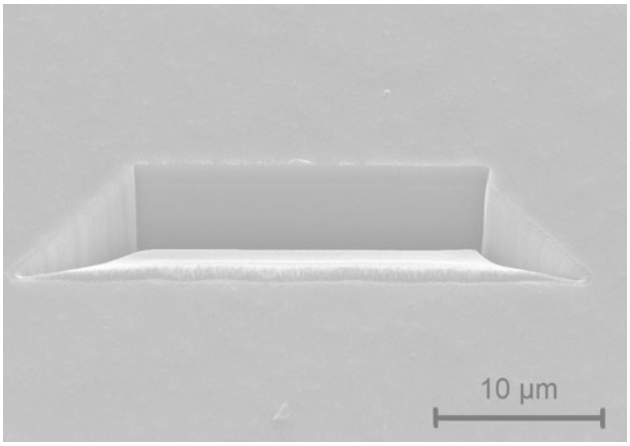

Figure 3.14: FIB trapezoidal cut for VO_2 thickness measurement.

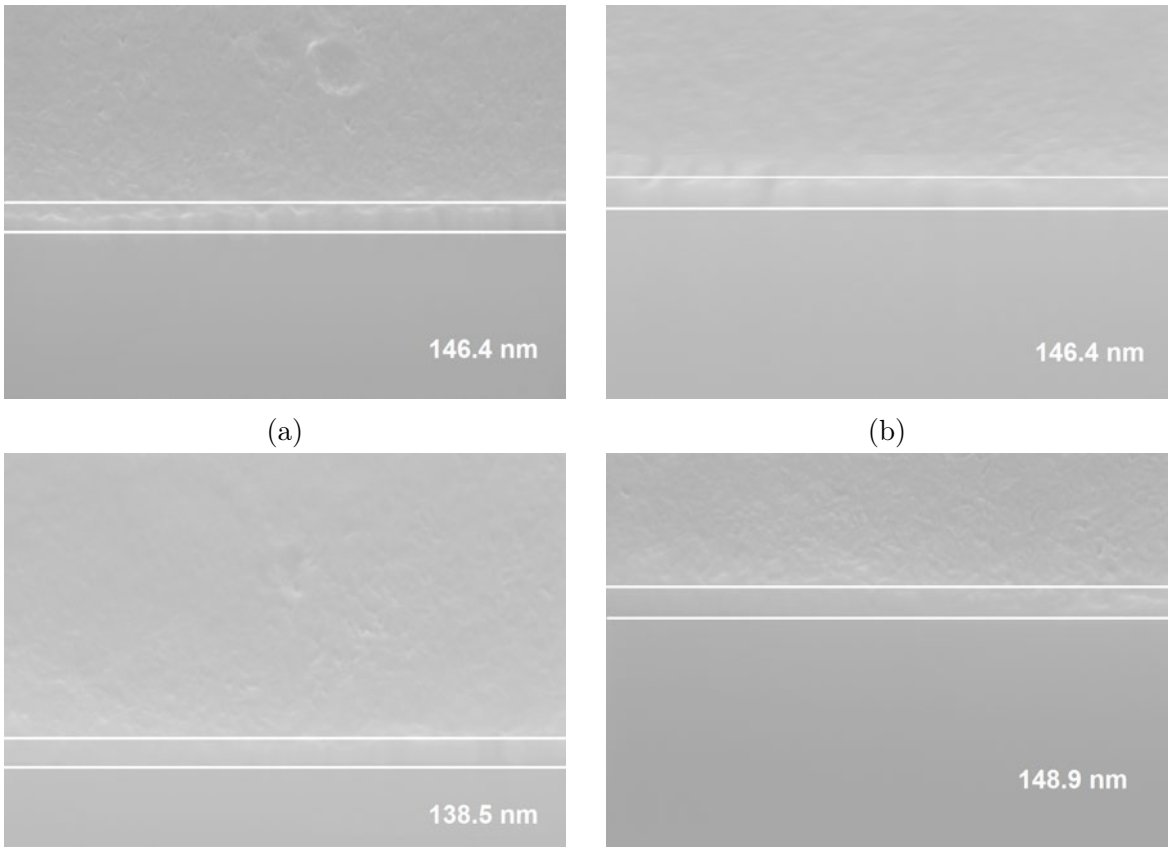

(a) (b)

(c) (d)

Figure 3.15: SEM cross-sectional thickness measurement for $VO_2/SiO_2/Si$. Note: The value labeled on these figures corresponds to the measurement between the white bars.

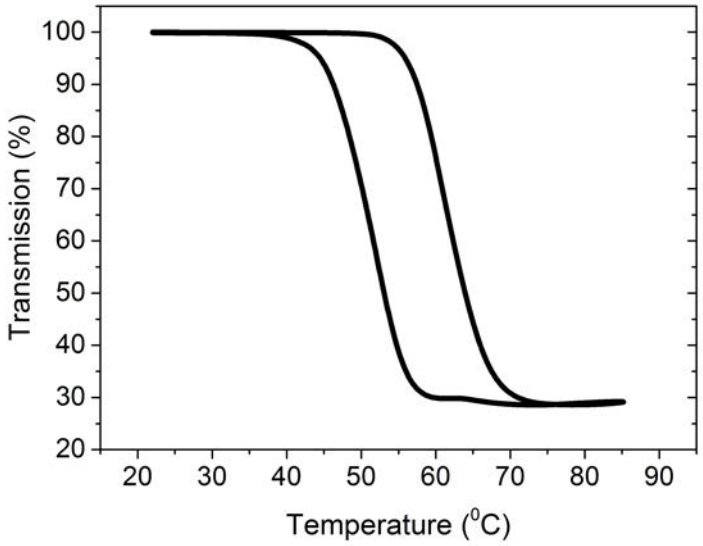

Figure 3.16: Transmission for VO_2 deposited by sol-gel method as a function of temperature (heat rate: $\sim$0.4 °C/s) for λ=1550 µm.

3.3 Pulsed Laser Deposition (PLD) Process

3.3.1 Deposition Conditions

PLD was used to deposit the VO_2 thin films used in the devices developed and described in this thesis. Table 3.2 summarize these conditions. More details about the deposition conditions can be found in following chapters.

Table 3.2: PLD deposition conditions

	Device 1	Devive 2	Device 3
Temperature ^{o}C	600	595	595
Ar Flux (sccm)	10	-	-
O_2 Flux (sccm)	15	20	15
Repetition Rate (Hz)	10	10	10
Deposition Time (min)	30	30	25
Annealing Time (min)	-	30	30

3.4 Crystallization of PLD growth VO_2 thin films assessed by XRD

XRD was used to characterized the VO_2 thin films grown by PLD. **Figure** 3.17 shows the spectrum on a VO_2 thin film deposited by PLD under Ar/O_2 gas mixture on SiO_2. The SiO_2 amorphous substrate broad peak centered around 21° is shown in this plot. Materials with no crystal structure (such as the amorphous fused silica used as substrate) produce these scattered reflections. **Figure** 3.18 shows the spectrum for VO_2 deposited by PLD on an oxygen atmosphere on a SiO_2 substrate. Thin films grown with only O_2 gas showed better orientation as evidenced by the stronger peak $\sim 28°$.

The XRD results for sol-gel deposited VO_2 is shown in **Figure** 3.19 for comparison purposes. A much weaker peak is observed $\sim 28°$ for this film. Sol-gel deposited VO_2 thin films show lower crystal orientation.

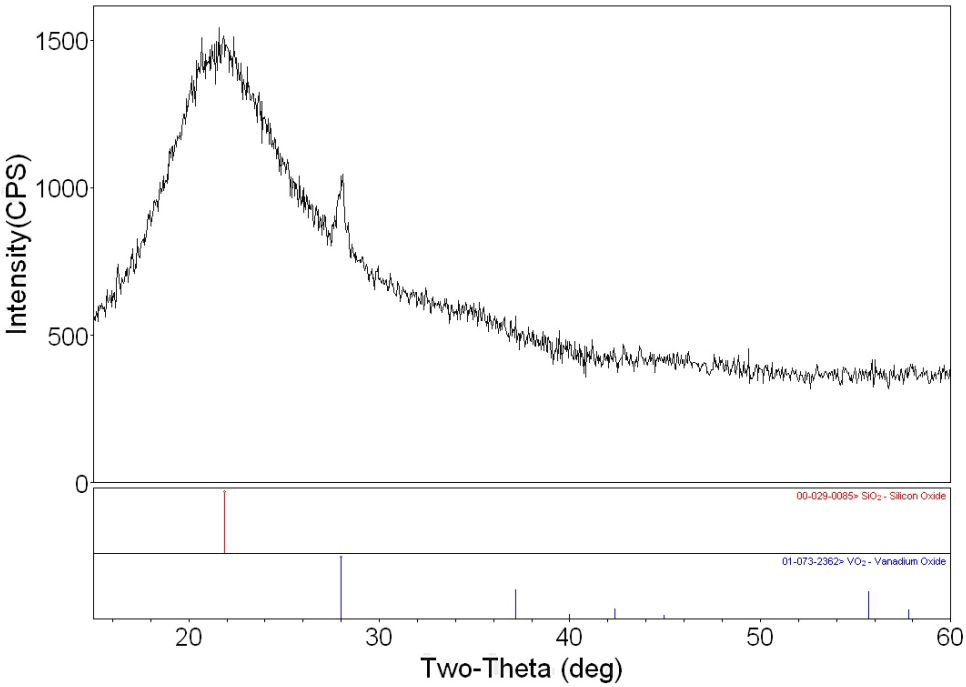

Figure 3.17: XRD characterization of a VO_2 thin film and SiO_2 substrate deposited under Ar/O_2 atmosphere.

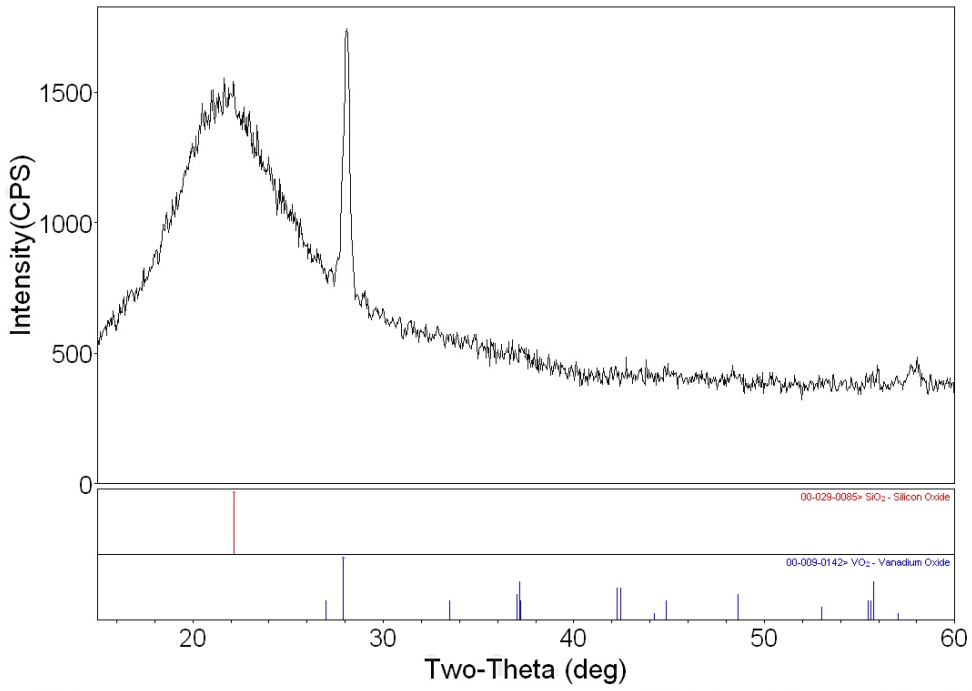

Figure 3.18: XRD characterization of VO_2 thin film and SiO_2 substrate deposited under O_2 atmosphere.

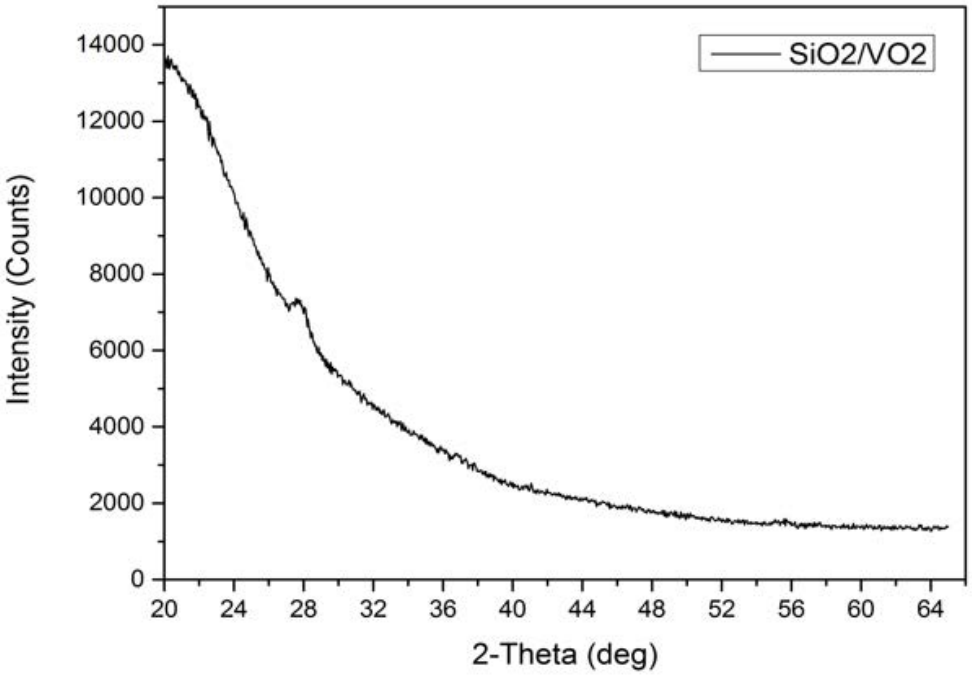

Figure 3.19: XRD results for SiO_2/VO_2 deposited by sol-gel.

3.5 Summary

In this chapter, two deposition processes were investigated for VO_2 thin film deposition. Sol-gel deposition process was used for SiO_2 and Si (100)/SiO_2 substrates. The sol-gel synthesis, gel deposition, and drying treatments were discussed. The annealing conditions (e.g. time pressure, and time) for this process were studied. Electrical characterization (resistance and a function of temperature curves) were used as a parameter to describe the quality of the VO_2 thin films. Optimum annealing conditions found for SiO_2 substrates were applied to Si/SiO_2 substrates. These VO_2 thin films were characterized by XRD, Raman spectroscopy, surface contact profiler, AFM, and SEM. Also the optical transition of these films was investigated for a wavelength of 1550 nm. VO_2 thin films deposited by PLD were characterized by XRD and compared with sol-gel results.

CHAPTER 4

NIR IMAGE PROJECTION BASED ON VO_2 OPTICAL MEMORY

In this chapter the hysteretic behavior of VO_2 is used for the projection of near-IR (NIR) images by programing multiple optical states on the VO_2 thin film. The optical states were programmed by photothermal actuation, scanning a focused red laser on localized regions of the VO_2 thin film. The abrupt change in transmission of NIR wavelengths across VO_2's solid-to-solid phase transition was used to reflect a diffused near-IR beam in the regions scanned by the red laser. The transmitted NIR beam was projected on a laser beam profiler. The results of a single scan from the red laser show images with a high contrast between the two phases of the material [144].

4.1 Sample Preparation

The VO_2 film was deposited on SiO_2 substrate by pulsed-laser deposition (PLD). The deposition was done by using a KrF laser at 10 Hz repetition rate with a pulse energy of 350 mJ into a rotating vanadium target while maintaining an O_2-Ar gas atmosphere (15 and 10 standard cubic centimeters per minute, respectively) at 20 mTorr. The substrate temperature was 550 °C. The substrate had width, height, and thickness of, respectively, 15, 11, and 1 mm. The deposited VO_2 film thickness was $\sim$ 300 nm âĂŞ as measured using a Veeco Dektak 6M Profiler âĂŞ and showed a resistance change close to two orders of magnitude when the temperature was cycled between 30 and 90 °C. The change in resistance showed hysteretic behavior, typical of VO_2.

4.2 VO_2 Optical Memory

The VO_2 optical memory for a wavelength of 1550 nm was investigated by measuring the transmittance as a function of temperature as the phase transition of VO_2 was induced by conductive heating using Peltier heaters. The temperature setpoint were cycled from 20 °C to 70 °C as shown in **Figure** 4.1. The major and minors transmittance hysteresis loops demonstrate the VO_2 material capability to store multiple optical states.

The VO_2 thin film has different transmittance values or optical states at the same temperature based on the previous thin film's temperature, which is known as 'memory'. Initially, the VO_2 thin film temperature increases from 20 °C to a temperature above its IMT following the heating curve in **Figure** 4.1 (e.g. 70 °C). As the film's temperature decreases, now following the cooling curve in **Figure** 4.1 the transmittance of the VO_2's film will be different from than it had before at certain temperature (e.g. 50 °C). Multiple optical states are obtained by cycling the temperature of the VO_2's thin film as shown in **Figure** 4.1, at 55 °C 7 optical states are shown.

4.3 Projection Setup

NIR image were programmed and projected using the optical set-ups shown in **Figure** 4.2 and **Figure** 4.3. An IR projecting laser beam (λ=1550 nm, 90 mW, spot size diameter ~1.5 mm, Thorlabs FPL1055T) was diffused into a square shape (7.25 mm × 7.25 mm) of uniform intensity on the VO_2 film. The optical diffuser was used to provide uniformity, in terms of optical power or intensity to the image plane. This optical diffuser with a diffusing angle = 6° (EDS-A RPC Photonics) was aligned between the IR laser and the VO_2 sample. The area of the VO_2 thin film illuminated by the diffused IR beam is the plane in which the NIR image to be projected will be programmed. A writing laser (λ=650 nm (red), power = 100 mW, spot size diameter ~ 600 µm) was focused on the VO_2 film. A scanning system (Thorlabs GVS002 - 2D Galvo System) was placed in the path of the writing laser. This

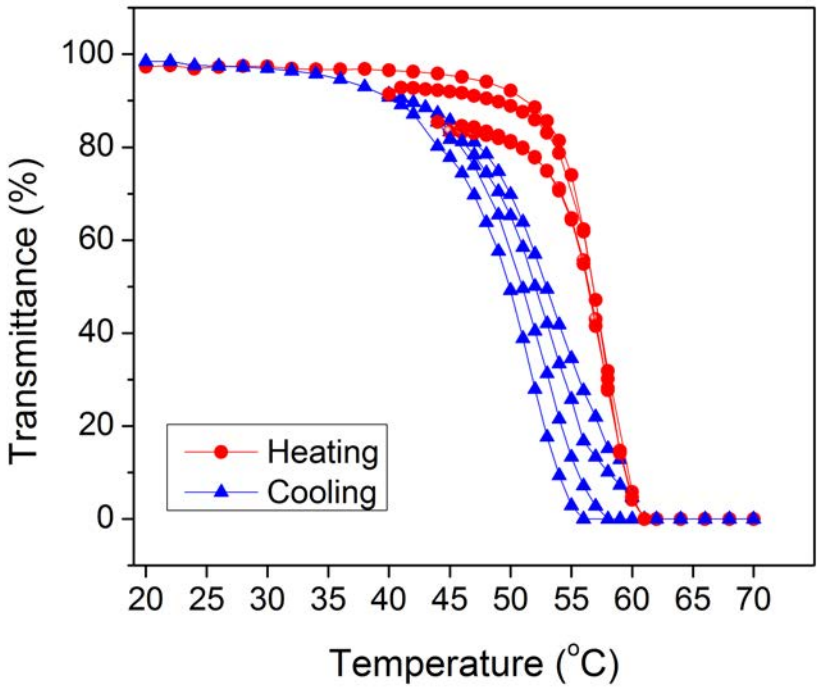

Figure 4.1: Optical transmittance of a ~300 nm thick VO_2 film deposited by PLD across the phase transition.

system has a pair of mirrors, which were computer-controlled using LabVIEW programming to write a pattern on the VO_2 film.

In order to use the memory capability of VO_2, it is necessary to operate within the

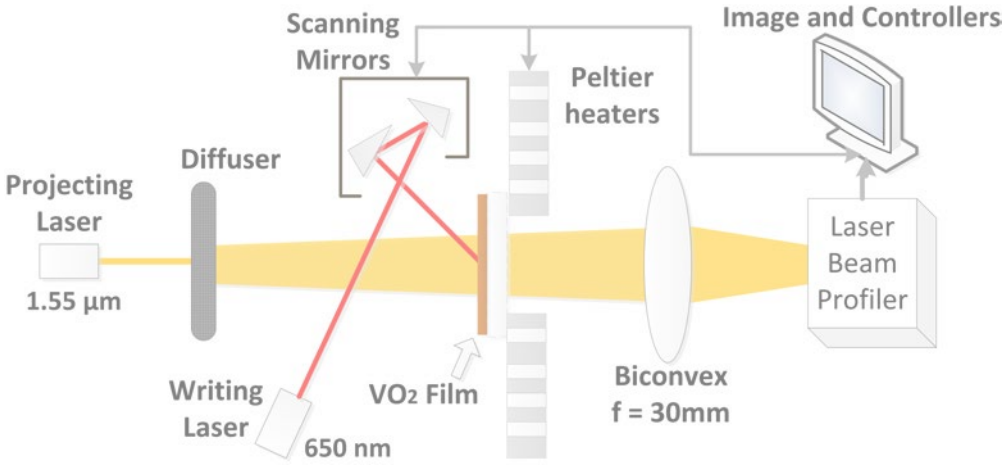

Figure 4.2: Experimental optical system with diffuser used to program an image onto a VO_2 thin film

hysteretic region [91]. Therefore, a pre-heating of the sample to a temperature close to the phase transition (hereinafter referred as the operating temperature (OT)) was done by using two Peltier heaters, which also served the purpose of holding the sample. The heaters were controlled in a feedback configuration by a temperature controller (Newport 350B).

The diffused IR beam transmitted through the VO_2/SiO_2 sample was focused into a detecting Laser Beam Profiler (LBP) image sensor (LBP-4 Newport, sensor area: 6.47 mm $\times$ 4.83 mm) by using a biconvex lens transparent to IR wavelengths with a focal length of 30 mm. A calibration process was performed to limit the writing laser scanning to a region inside the IR irradiated area, compensate for the image inversion due to the biconvex lens, and focus the IR diffused beam on the LPB image sensor.

A similar setup eliminating the diffuser was investigated. In this case a higher power laser was used and the laser beam was expanded to have a relatively uniform intensity at the image plane. If was found the diffuser coating introduce visible grains on the image. **Figure** 4.3 shows the experimental setup used for the experiments with no diffuser.

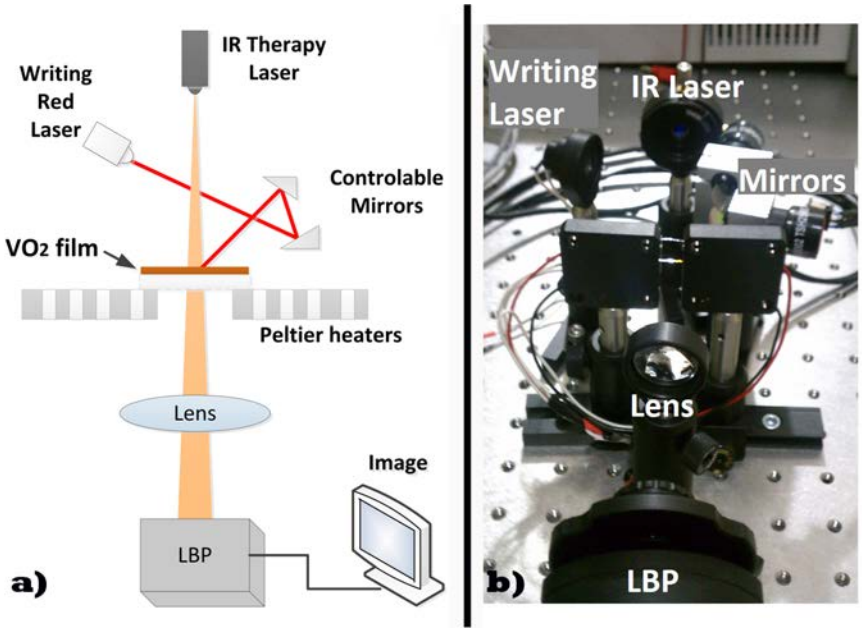

Figure 4.3: Experimental optical setup eliminating the diffuser used to program an image onto a VO_2 thin film, a)schematic diagram b) photograph of the setup.

4.4 Non-pixelated Image Calibration

A single scan of the writing laser will increase the temperature in the illuminated VO_2 thin film, locally inducing the phase transition and causing a significant drop in the transmittance of IR wavelengths. The scanning rate of the micro mirrors was calibrated to have a non-pixelated image as shown in **Figure** 4.4.

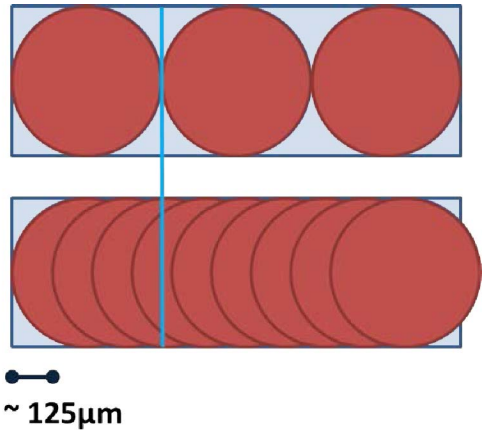

Figure 4.4: Pixels calibration by control of the micromirrors scanning speed.

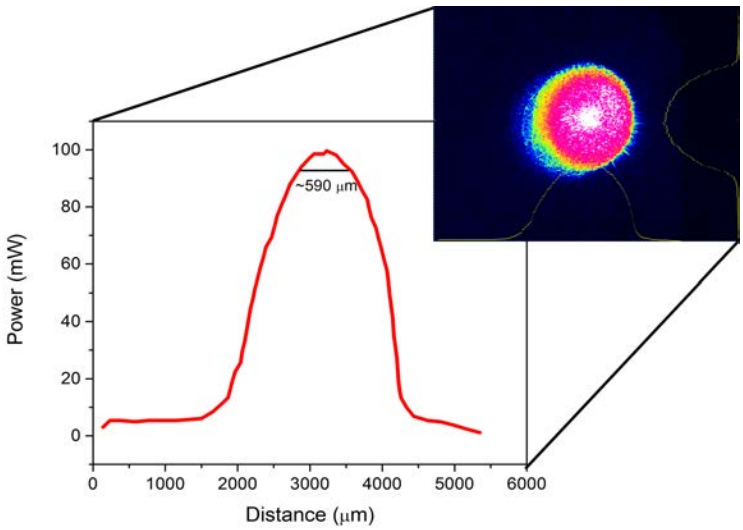

Figure 4.5: Red laser beam profile along the x-direction. Inset show the intensity contour.

The scanning rate was selected empirically to optimize uniformity, contrast, and image resolution. The scanning distance was chose to $\sim 125\,\mu m$ to uniformly heat the image path

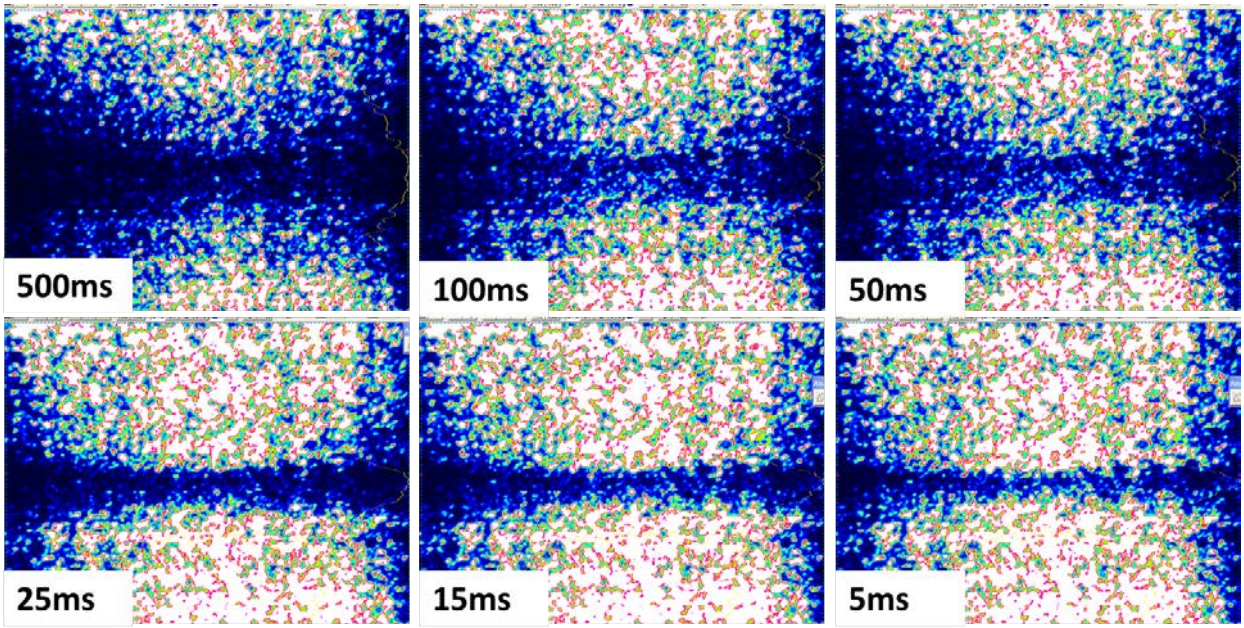

Figure 4.6: Micro-mirrors scanning speed calibration.

as the heating laser spot size was $\sim$ 590 µm as measure with the LBP as shown in **Figure** 4.5. Larger distances between the scanning movements introduced gaps within the writing path. The scanning speed was selected to 25 ms based on **Figure** 4.6. Lower scan speeds (e.g. 50 ms, 100 ms) affects the resolution of the image heating a large area. Faster scanning time was not enough to heat the film and induce the material transition. The writing laser was scanned a rate of approximately 5 mm/s within a continuous path - moving each 25 ms a distance of 125 µm.

4.5 Results

First, a proof-of-concept experiment was performed to determine the capability of near-IR projection and reflection through VO_2 as the material undergoes a phase transition. **Figure** 4.7 shows optical transition of the VO_2 thin film as temperature increases. For this experiment the IR laser λ=1550 nm was projected through VO_2/SiO_2 sample into a laser beam profiler (LBP). The IR laser was operated at lower power (4 mW) and focused to spot size of $\sim$ 3 mm, and the temperature was controlled by the Peltier heaters. As the

temperature increases the material transition is induced and the IR radiation transmission decreases.

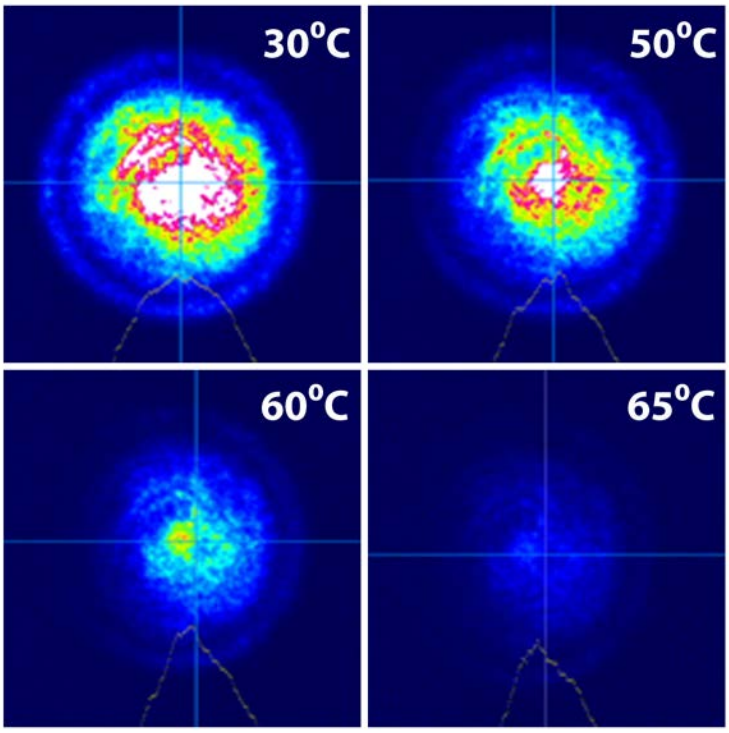

Figure 4.7: IR optical transmittance through VO_2/SiO_2 as film's temperature increases.

The transmittance curves (shown in **Figure** 4.8) were normalized with respect to the power measured by the LPB when no sample was placed between the diffused IR beam and the LBP (i.e. power of the diffused IR beam was 100 %). This transmittance (still at room temperature) decreased to 97 % when the VO_2/SiO_2 substrate was added (1 % due to the SiO_2 substrate, and 2 % due to the VO_2). The different loops shown in **Figure** 4.8 are the major and minor loops resulting from heating/cooling sequences of decreasing amplitude; from 20 °C up to 70 °C temperature range. This demonstrates that the presented IR image projection system could be programmed to have multiple optical states, which would translate into programmable contrast levels in the projected image. In this work, only one contrast level was used.

In order to increase the contrast of the projected IR image, it is necessary to increase the difference in transmittance of the VO_2 thin film. This will occur when the operating

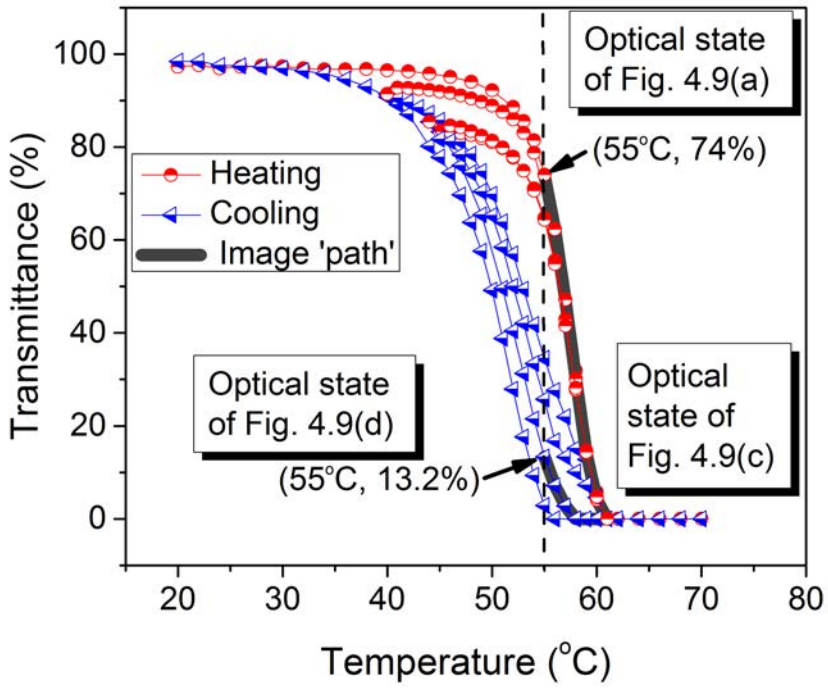

Figure 4.8: NIR $\lambda = 1.55\,\mu m$ transmittance through VO_2 during heating and cooling temperature cycles. The different optical states are identified as an image is programmed and projected. Only some minor loops are shown for clarity.

temperature corresponds to the largest separation between the heating and cooling curves. This operating temperature was determined to be 55 °C from the VO_2 optical transmittance characterization experiment. It should be mentioned that this temperature of 55 °C is the temperature as measured (and controlled) at the surface of the Peltier heaters, and it corresponds to a temperature of $\sim$ 52 °C at the center of the sample. The sample temperature was set to 55 °C and after it stabilized the actual temperature of the VO_2 films was measured using a thermocouple placed at the center of the sample.

The NIR transmittance at the operating temperature was found to be 74 % (see **Figure** 4.8). While the temperature at the surface of the Peltier heaters was maintained constant, the writing laser increased the temperature in the scanned regions above the transition temperature, following the major heating curve. After the writing process is over, the scanned region returns to the operating temperature, but now following one of the cooling curves,

which ends at a different transmittance value depending on the specific minor curve followed. Considering the temperature increase induced in the VO_2 by the writing laser (which was measured directly on the sample), it was confirmed that the temperature increases 6 °C above the operating temperature returning to a transmittance state of 13.2 % as pointed in **Figure** 4.8. A contrast ratio of approximately 6:1 was obtained between the two programmed and stored optical states.

IR images were programmed, stored, and projected by using the optical setups described in **Section 4.3**. **Figure** 4.9 shows different stages of the programming sequence of an image on the VO_2 film by using the projection setup in **Figure** 4.2. In this case, we chose the capital letter âĂŸSâĂŹ from our affiliation logo; but the pattern shape can actually be drawn in a graphic user interface that was created − any shape can be programmed and projected. **Figure** 4.10 shows the programming sequence of a square shape by using the projecting setup described in **Figure** 4.3, which eliminates the diffuser. These images demonstrated that the 'grainy' profile observed in **Figure** 4.9 is due to the optical diffuser used in **Figure** 4.2.

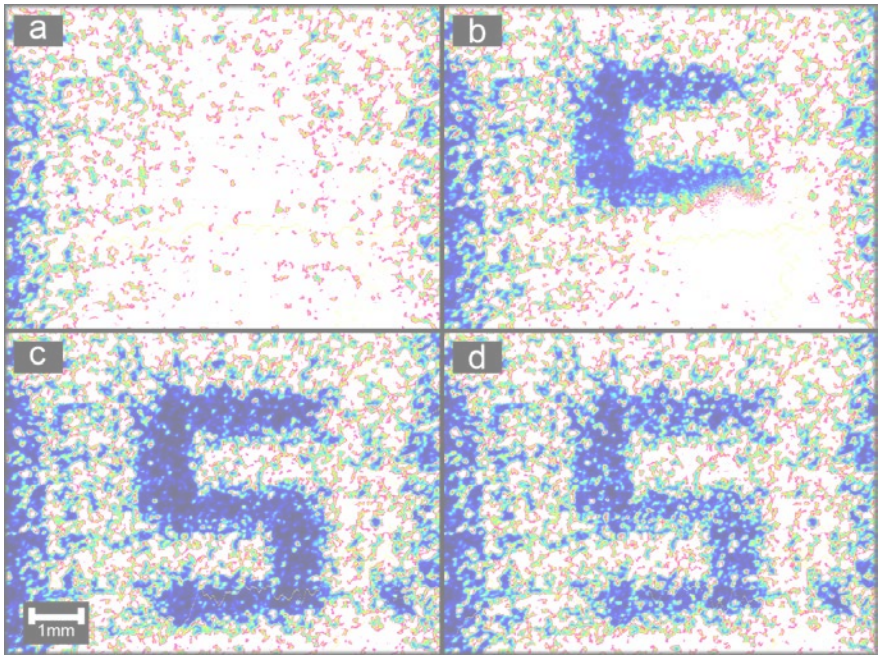

Figure 4.9: Programmed and projected NIR image: a) at 55 °C before laser scanning, b) during writing laser scanning, c) right after the writing laser scan finished, and d) programmed image 5 minutes after scanning. 'Grainy' profile was found to be characteristic of the diffuser.

During early experiments to develop this IR projector technology, a lower intensity laser was used. Expanding the laser beam was not enough to cover the projecting plane on the LBP and the use of the diffuser was necessary. In this case the diffuser was eliminated because a higher intensity laser was used and expanded to cover most of the projecting plane. However, non-uniform corners are observed in **Figure** 4.10 a. The pattern was mostly written inside the uniform intensity area.

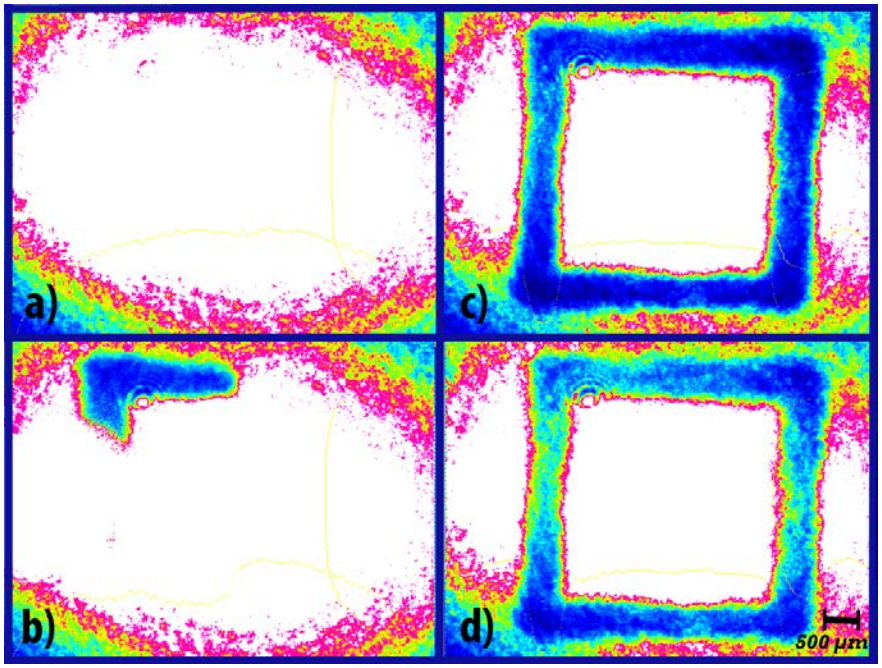

Figure 4.10: Square pattern programmed into the VO_2 and projected NIR image: a) at 55 °C before laser scanning, b) during writing laser scanning, c) right after the writing laser scan finished, and d) programmed image 5 minutes after scanning. 'Grainy' profile was eliminated by removing the diffuser.

The process of programming the VO_2 film started with the diffused NIR projecting laser illuminating the film. The image was programmed at the operating temperature of 55 °C (**Figure** 4.9-a and **Figure** 4.10-a). The writing laser was turned ON and a single writing laser scan, which took about 2 seconds to complete, was enough to program the image. This time limitation is due to the used scanning method and is independent from the material time response. When the writing laser is turned OFF the pattern is stored in the VO_2 thin film and projected simultaneously by the projecting laser.

4.6 Device Characterization

The minimum feature size of the pattern (i.e. pixel size) measured on the LBP was ∼600 µm, which corresponded to ∼860 µm in the VO_2 thin film plane. The diffused NIR beam was optimized to cover the largest area of the VO_2 thin film. The developed optical system was characterized assuming a pixel size of ∼600 µm (see **Figure** 4.5). It showed a resolution of ∼10 pixels in the x-direction and ∼8 pixels in the y-direction. Using the developed system the programmed image was completely erased by decreasing the operating temperature. The complete âĂIJresetâĂİ of the optical memory states in VO_2 was done by decreasing the operating temperature to room temperature.

The observed behavior was analyzed by the temperature change in the VO_2 film due to the writing laser radiation. This change in temperature was calculated by using the following equation:

$$\Delta T = \frac{Pt}{\rho V C_{\mathrm{p}} - \frac{\kappa A t}{d}}, \tag{4.1}$$

where ρ, C_p and κ are the density, specific heat, and thermal conductivity of VO_2, respectively; V is the film heated volume; A is the area of the VO_2 film illuminated by the writing laser; d is the film thickness, t is the irradiation time, and P is power absorbed by the VO_2 film. The power absorbed by the VO_2 was calculated to be 52.9 mW by using the Lambert-BeerâĂŹs Law. The material extinction coefficient for the insulating phase ($\sim$ 0.3) [[145]] and the angle of incidence, ($\sim 45^\circ$ were considered).

A simulation was performed using finite element method (FEM) analysis (COMSOL Multiphysics) to determine the temperature change and validate the calculation. The sample dimensions, parameters and all the boundaries conditions used in the simulation resembled the values used in the experiment. For a radiation exposure time of 25 ms, **Equation** (4.1) and the simulation gave a final temperature of 58.8 °C and 67 °C, respectively. **Figure** 4.11 shows the FEM simulation before and after 25 ms of red laser radiation.

The calculated value agrees with the film direct measurement of 59 °C, suggesting that

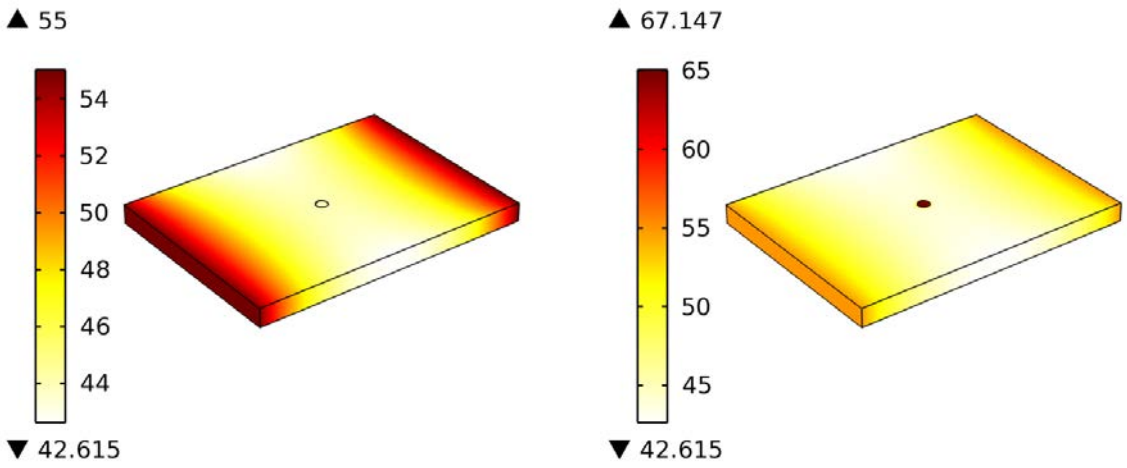

(a) (b)

Figure 4.11: Finite element method (FEM) simulation at (a) operating temperature, (b) after 25 ms of red laser radiation.

the programmed image followed a minor loop path (as shown in **Figure** 4.8). The simulation showed 67 °C as the highest temperature at the center of the spot; which covered a smaller diameter of ∼400 µm. A temperature difference of 12 °C was seen between the spot center and the boundary of the circle used to simulate the writing beam spot size (600 µm diameter). The difference between the FEM simulation and analytical methods is believed to be due to the non-uniform temperature distribution of the Peltier heaters configuration. The operating temperature used for the calculation was the direct measurement on the film, while the simulation calculates its own operating temperature after the system reaches steady state (43 °C).

4.7 Summary

In this chapter, a programmable NIR image projector was demonstrated by successfully using the optical hysteresis of VO_2 thin films across its phase transition and a relatively simple optical set-up and device. An optical diffuser for IR wavelengths was used in one projecting set-up resulting in a 'grainy' image projection. A grain free image was achieved using a similar optical set-up by removing this optical component. The minimum feature

size of the projected image was determined by the writing laser spot size. The system can erase an image and reach the operating temperature in ∼2 s. The images are programmed at a writing rate of 5 mm/s. In the next chapter, the optical transition of VO_2 is explored to develop a VOA optoelectronic device.

CHAPTER 5

VO_2-BASED VARIABLE OPTICAL ATTENUATOR

In this chapter, the correlation between the optical and electrical properties of VO_2 are presented for the development of a variable optical attenuator in the near-IR region (λ=1550 nm). This work introduces the VO_2 capability of electronic tunability for NIR applications, specifically in free space. A model to estimate optical transmission by sensing the electrical resistance of VO_2 is presented. This model is implemented with self-sensing and feedback control to attenuate an optical signal through VO_2.

5.1 Electro-optical VO_2 Properties Correlation

Recent studies suggest that the change in the the electrical and optical properties comes as the result of the first-order insulator-to-metal-transition (IMT) [68, 89]. While the change in both properties show hysteretic behavior (as shown in **Section 1**), the fact that both changes are strongly correlated can be used to reduce the hysteresis when one property is plotted against the other. A series of experiments are performed to confirm this correlation by measuring both properties simultaneously.

5.2 Self-Sensing Feedback

In this work, self-sensing refers to the estimation of the optical parameter (transmittance) based on the measurements of another correlated parameter (resistance) of the same material. Self-sensing of VO_2 thin film is used to control the transmittance across the material. The electrical resistance of VO_2 is measured while the optical transmission is estimated by a determined model and controlled by a close-loop feedback that includes the self-sensing model.

A proportional-integral (PI) controller configuration was designed and implemented. The controller gain values were determined from a set of performance specifications and the system dynamics (which are dominated by the thermal dynamics from the heater). Due to the relatively slow system response, which is characterized by an open-loop time constant of 18.5 s, the targeted response time for the closed-loop controlled transmittance is 10 s. The measurement setup described in **Section 5.4** is used to perform the VOA closed-loop tests with a configuration represented by the block diagram shown in **Figure** 5.1. The resistance of the VO_2 (R) is sensed and used in the model to calculate the correspondent transmission (T_c). This value (T_c) is then compared with the desired transmission (T_s). The error (E) goes to the PI, which controls the current (I) that is sent to the Peltier in order to change the temperature of the sample, therefore controlling the transmission percentage (T).

5.3 Device Fabrication

Although the phase transition in VO_2 has been demonstrated to occur at ultrafast time scales, most of the current VO_2-based devices are operated by heating the material above the transition temperature. The VO_2-based VOA reported in this letter was operated by conductive heating from a Peltier heater. The device consists of a VO_2 thin film with coplanar electrodes. The VO_2 thin film (200 nm thick) was grown on single crystal quartz

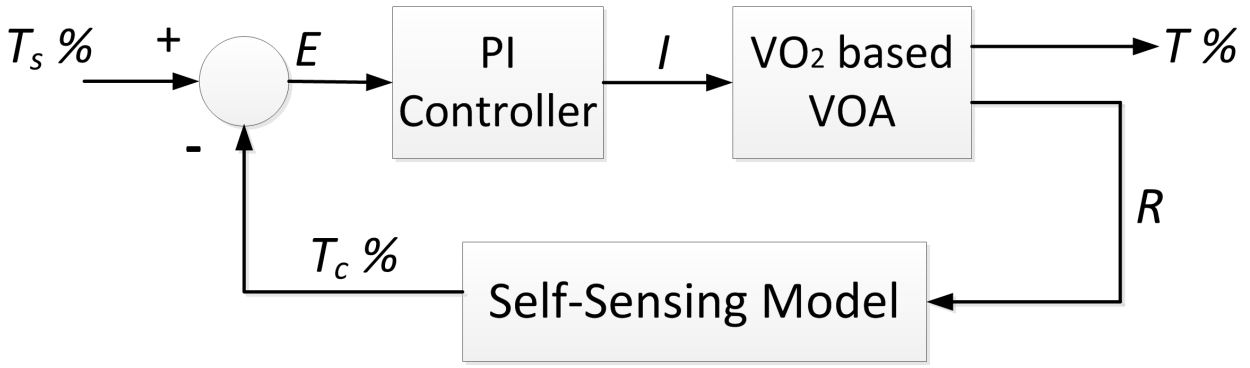

Figure 5.1: Schematic representation of the closed-loop control system for the VOA using self-sensing.

(SiO_2) substrate (12 mm wide, 11 mm long, and 250 µm thick) by pulsed laser deposition (PLD) at 600 °C. A KrF excimer laser was used with a fluence of $\sim 2\,J/cm^2$ at 10 Hz repetition rate on a vanadium target. During VO_2 deposition, the backside of the sample was covered by a single crystal silicon wafer piece. This was done to avoid the deposition of material residue on the backside of the substrate, which was observed in previous depositions and experimentally verified to have an impact on the optical transmittance behavior of the sample. Also during deposition, a shadow mask was used on the sample front side with a 5 mm opening, which allowed for the deposition of a VO_2 rectangular patch that extended the substrate width of 12 mm. The film was deposited for 30 min under 20 mTorr of oxygen pressure. The deposition was followed with an annealing step of 30 min at the same temperature and pressure conditions used during deposition. After the VO_2 deposition, the sample was taken to a custom-built evaporator for the deposition of aluminum, where another shadow mask was used to form the two coplanar electrodes on the VO_2 film. The device was then mounted on a Peltier heater with a centered hole (Thorlabs, TEC1.4-6). The inset on **Figure** 5.2 shows the final assembly of the device with the patterned VO_2 centered on the heater.

5.4 Electro-thermo-optical Setup

The device was mounted in the electro-optical setup shown in **Figure** 5.2. A NIR diode laser with wavelength of 1.55 µm and a spot size of $\sim$ 5 mm (Thorlabs, FPL1055T), an optical power sensor (Thorlabs, S144C), and a power meter (Thorlabs, PM100D) were used for the optical measurements. Before the experiments, it was necessary to verify that the phase transition of the VO_2 film was not induced by the absorption of IR radiation coming from the laser. To this end, the laser power was initially set at its minimum (12 mW). Then, the power was increased to 150 mW and the spot size reduced in order to increase the radiation intensity on the sample, while the film was kept at room temperature and its resistance was being monitored. No noticeable change in resistance was measured in the process, which

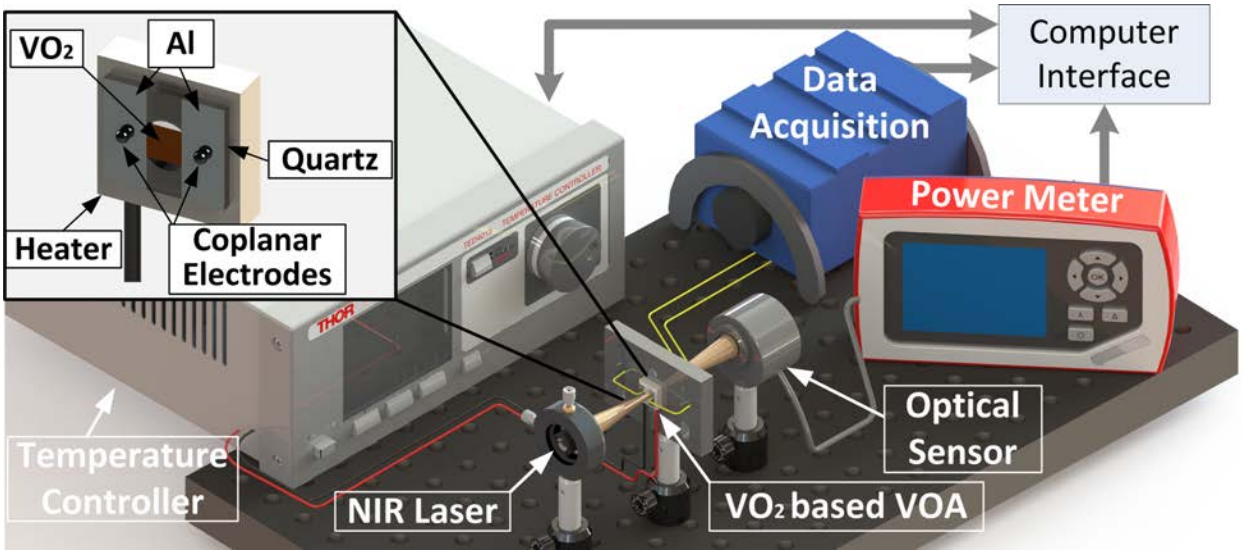

Figure 5.2: Setup used for performing optical transmission and electrical resistance characterization of the VOA. The setup is also used for controlling the VOA in closed-loop using the self-sensing technique.

indicated that the phase change was not being induced photothermally.

For the experiments, a laser power of 12 mW was used. The electrical measurements were recorded using a data acquisition system (National Instruments, cRIO), which was constantly measuring the VO_2's resistance through connections to the Al coplanar electrodes. A temperature controller (Thorlabs, TED4015) was employed to control the Peltier heater and trigger the material transition in the VO_2. A computer interface (using a virtual instrument in Labview software) was used to monitor the output of the data acquisition system, the power meter, and to input the temperature (for open-loop experiments) or desired transmittance (for closed-loop experiments).

5.5 Results

The VO_2 film was characterized by measuring its electrical resistance and optical transmittance as a function of temperature. Both measurements were done simultaneously, as the temperature was varied. The film's resistance across the phase transition showed a drop of almost three orders of magnitude; which evidences the good quality and orientation of the

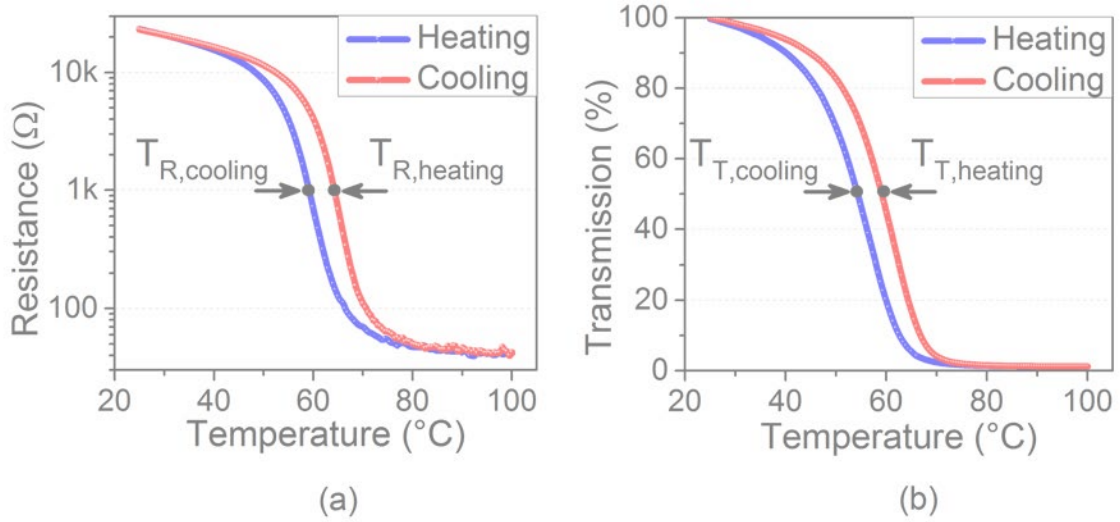

Figure 5.3: a) Electrical characterization for VO_2 thin film as function of temperature; b) Optical characterization of the VO_2-based VOA for 1.55 µm.

film (see **Figure** 5.3-a). The drop in the optical transmission across the phase transition was normalized using as reference the transmissivity at room temperature (1.6 mW). After this normalization the transmission drop was from 100 % to 2 % (see **Figure** 5.3-b).

It can be noticed that the widths of the resistance and transmittance hysteretic curves are very similar. However, the midpoints of the heating and cooling curves for the resistance and transmission curves (labeled in **Figure** 5.3) are different. Perhaps the most intuitive explanation for this would be the temperature gradient across the film and the different probing locations for both properties (i.e. electrical resistance and optical transmittance) –the optical transmittance of the VO_2 was measured at the center of the film, while the resistance was measured across the film's width through the coplanar electrodes. However, it was verified that the difference in temperature across the sample is only $\sim 1\,°C$, as measured with a thermocouple. Furthermore, the temperature is lower at the center of the sample (like it was measured previously on a similar set-up [144]), and this would have resulted in T_Ts greater than T_Rs, which is not what was observed.

Typically, the response of VO_2-based devices, shows hysteretic behavior between the

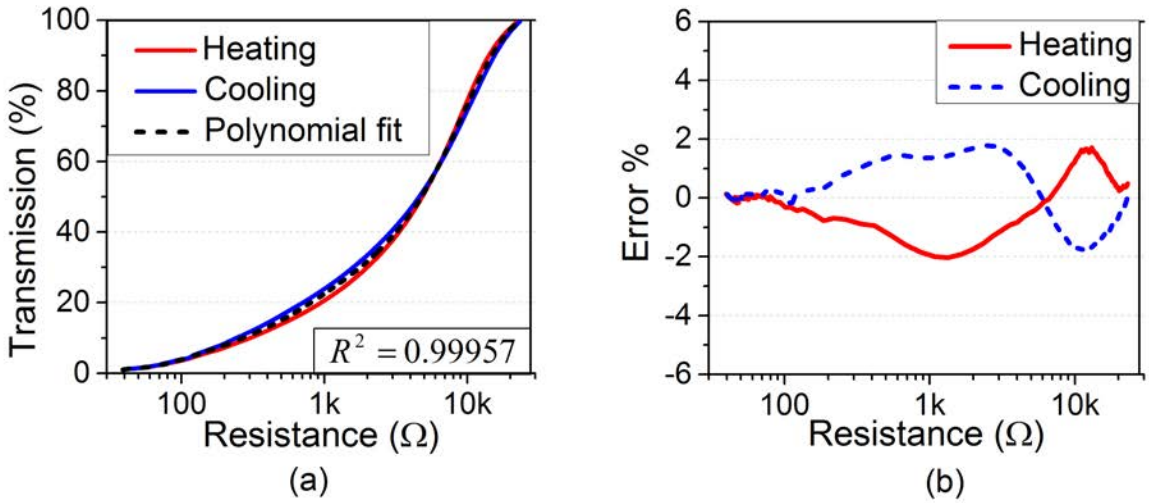

a_0= -0.124	a_2= -0.767x10^{-5}	a_4= -9.126x10^{-13}	a_6= -6.016x10^{-21}	a_8= -4.833x10^{-30}
a_1= 0.036	a_3= 5.306x10^{-9}	a_5= 9.456x10^{-17}	a_7= 2.298x10^{-25}	a_9= 4.301x10^{-35}

Figure 5.4: a) Transmission as a function of resistance and polynomial fit model; b) Error between the polynomial model and actual transmission percentage. The table shows the coefficients for the model.

input (usually temperature) and the output. However, if two strongly correlated properties are used, the relationship between them shows significant reduction of the hysteresis. **Figure** 5.4-a shows the plot of the two different responses of the VO_2 film (optical transmissivity vs. electrical resistance). The largest separation between the heating and cooling curves occurs at the 1 kΩ/20 % region, which corresponds to temperatures near the transition. This separation is greatly influenced by the difference in the transition temperature for both properties. This nearly one-to-one correspondence between electrical resistance and optical transmittance allows for the implementation of a self-sensing approach that would eliminate the need for complicated hysteresis compensation or inversion algorithms for controlling the device.

A ninth order polynomial fit was used to model the experimental data as shown in **Figure** 5.4-a by using the least square method. The polynomial coefficients are shown in **Figure** 5.4. The error between the model and the measurements of the actual transmission data was calculated in terms of transmission percent. **Figure** 5.4(b) shows a maximum error of $\pm 2\,\%$. The curve fit was used as feedback in the implementation of a simple (yet, effective) closed-loop control configuration. The complete system forms a fully electrically tunable VO_2-based VOA for NIR as described in **Section 5.2**

5.6 Device Characterization

In terms of decibels, the attenuation increased from 0 dB to 19.24 dB as shown in **Figure** 5.5. This results in a dynamic range of 19.24 dB, which is comparable with the typical range of 25 dB for commercially available VOAs.

A sequence of input steps (T_s) was used to validate the performance of the presented VOA in terms of transient and steady state error. **Figure** 5.6-a shows the response of the system to such sequence. The duration of each setpoint was 60 s. An average error of 0.55 % was calculated for the measured transmission with respect to the setpoint in steady state. Also, a complete error range of $\pm 2\,\%$ is shown in **Figure** 5.6-b, which also shows switching noise. These results show the efficient use of the self-sensing mechanism proposed in terms of transient and steady state performance. Accurate transmittance values were obtained using the self-sensing method proposed considering the average error value.

Figure 5.7 shows the response to a sinusoidal input signal consisting of the sum of three sinusoidal waveforms with frequencies of 0.5 mHz, 1 mHz, and 5 mHz; all with an amplitude of T=44%. The model and the measured signal followed the continuously changing setpoint with an average error of 1.15 %. The error range for the sinusoidal response is shown in **Figure** 5.7-b. This experiment demonstrates how the significantly reduced hysteresis allows for the accurate attenuation control of the VO_2-based VOA device, even during the transition region. The measured optical transmission from **Figure** 5.7 is also shown in **Figure** 5.8(a-b)

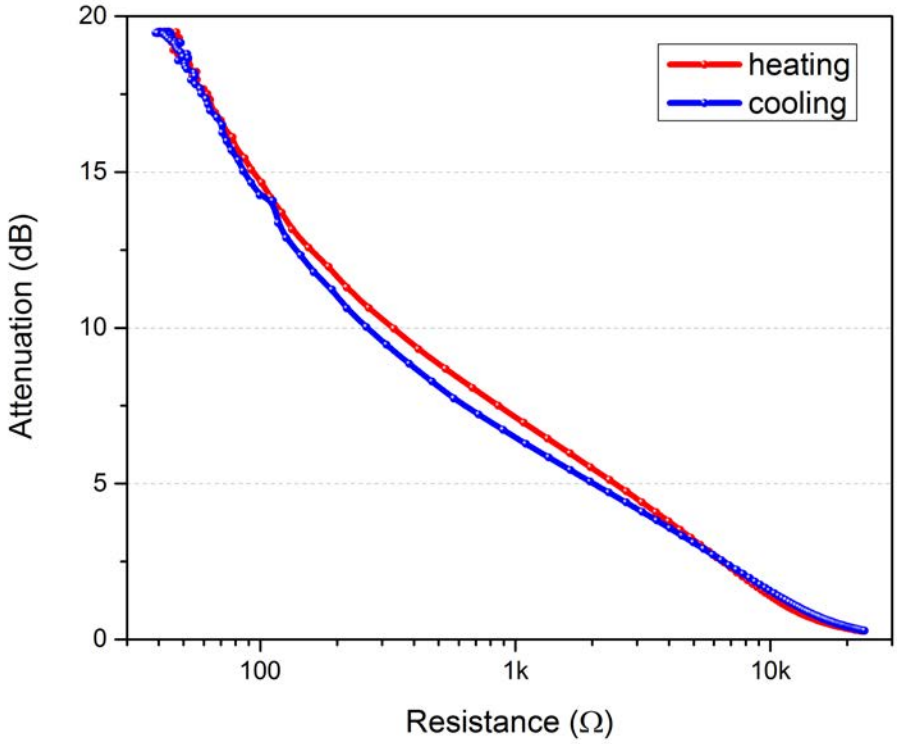

Figure 5.5: VO_2-based VOA attenuation response.

as a function of temperature and resistance, respectively. It can be noticed that the minor hysteretic curves are significantly reduced in **Figure** 5.8-b due to the strong properties correlation of the VO_2 film.

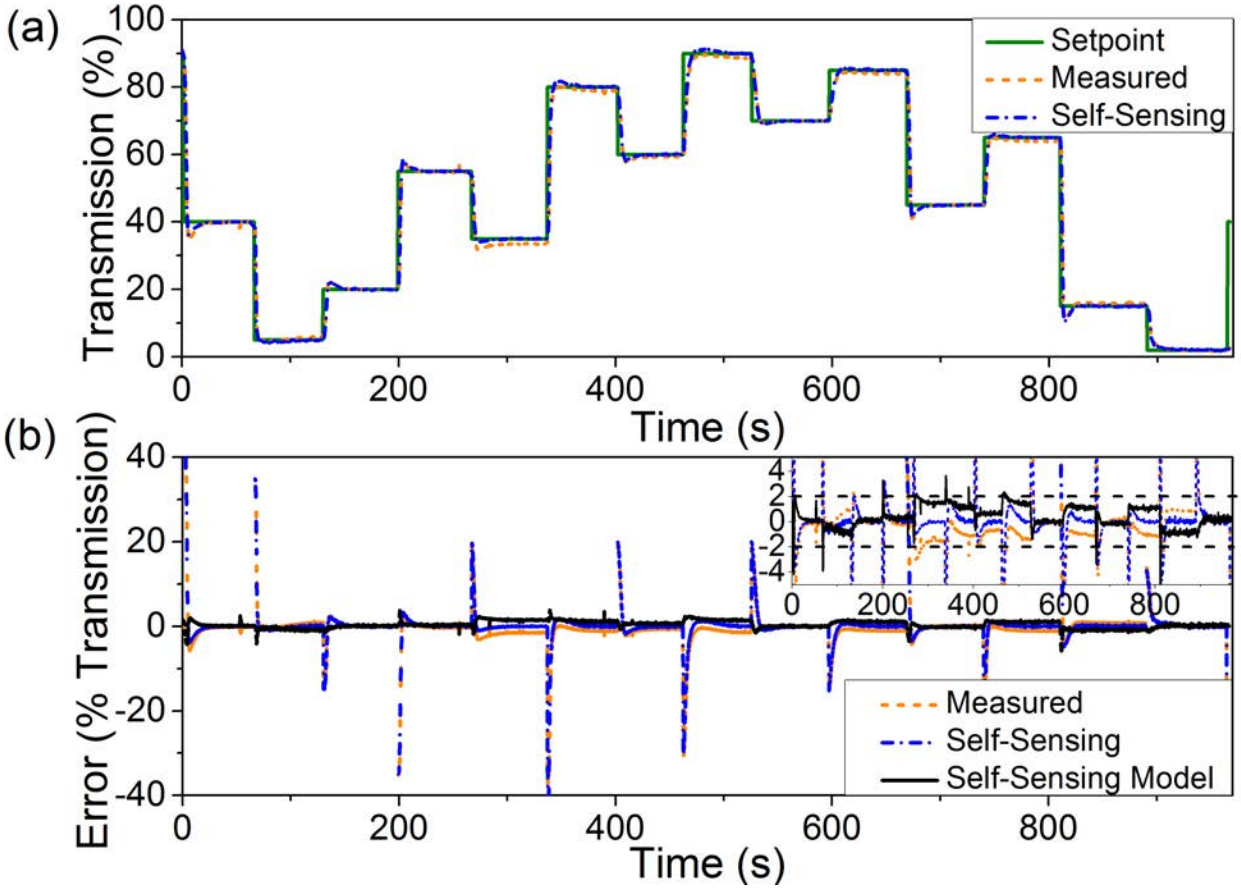

Figure 5.6: a) Step response for variable optical attenuator with self-sensing feedback control. b) Error calculation among the setpoint, measured and self-sensing signals. The inset shows a smaller scale for the error (y-axis).

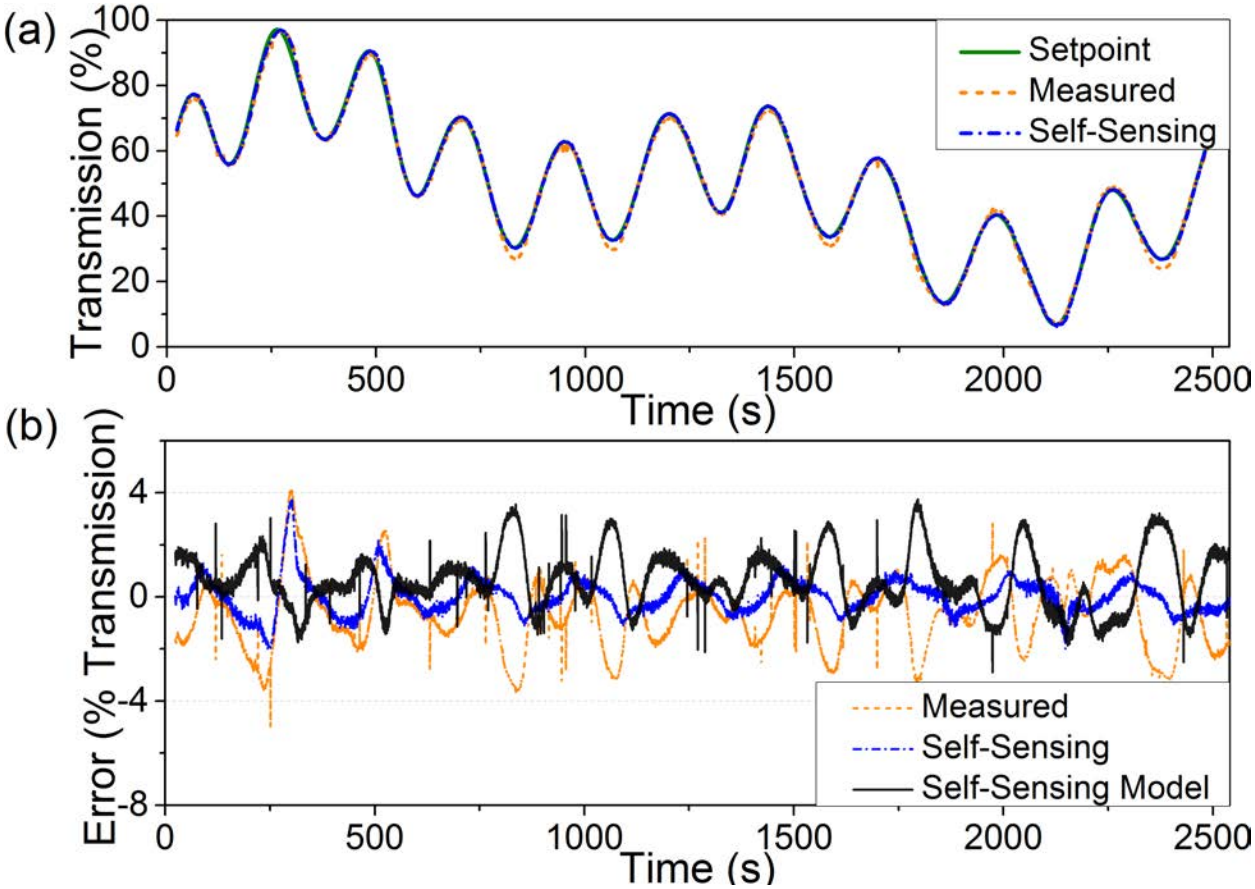

Figure 5.7: a) Sinusoidal response for a variable optical attenuator with self-sensing feedback control during the VO_2 transition. b) Error between the setpoint, measured and self-sensing signals.

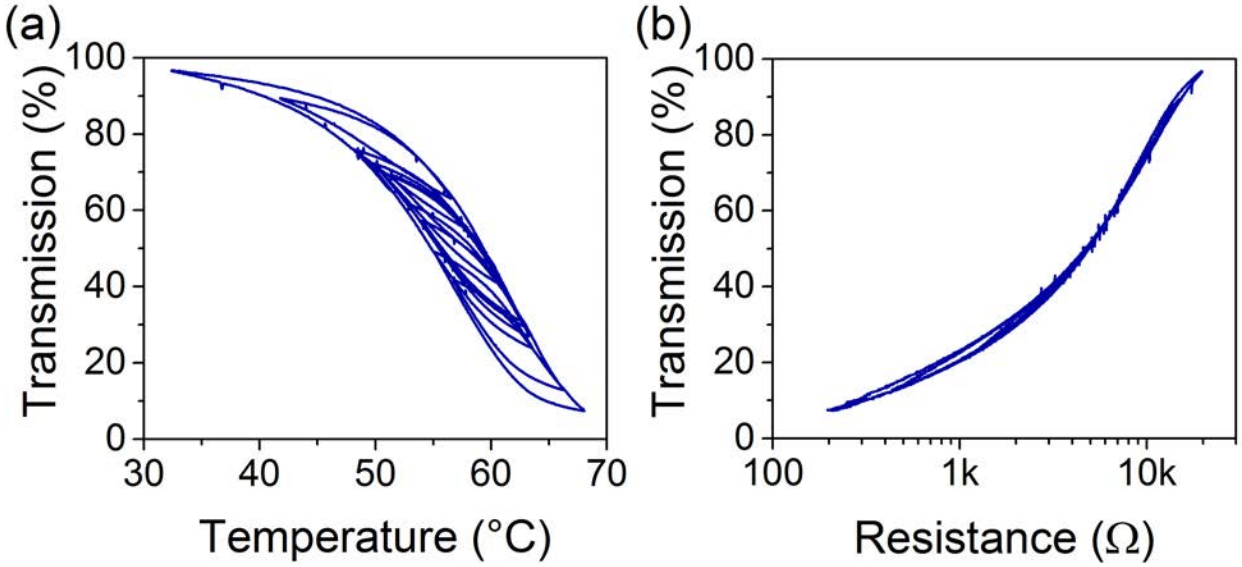

Figure 5.8: a) Optical transition as a function of temperature. b) Optical transition as a function of resistance.

5.7 Summary

This chapter presented the development of a variable optical attenuator (VOA) for near-IR wavelengths that is completely electrically tunable and does not require sampling or monitoring the optical beam for controlling the attenuation level. The VO_2-based VOA fundamental operation is based on the strong correlation of the electrical and optical properties of VO_2 across its IMT. The main contribution is the demonstration of a new VOA technology, which relies on the use of self-sensing techniques to control the attenuation of VOAs on a feedback configuration that also results in temperature stability. A highly accurate closed-loop control of the attenuation is achieved using the self-sensing technique shown.

CHAPTER 6

SCALING OF MICRO VARIABLE OPTICAL ATTENUATOR DEVICE

In this chapter an electronically controlled monolithic integrated micro VOA (μVOA) based on VO_2 thin film is presented. This μVOA device is an extension of the previously presented millimeter VOA. The size of the VO_2-based VOA is reduced to micrometer devices to minimize its thermal mass, which reduce the time response of the device.

Here the transmittance attenuation for NIR wavelengths and the scaling down of VO_2-based VOA devices is investigated. The devices consist on micro meter size square windows of 400, 300, 200 and 100 μm^2. These devices were designed, modeled and fabricated with an integrated heater and electrodes for self-sensing of VO_2.

6.1 Device Design and Structure

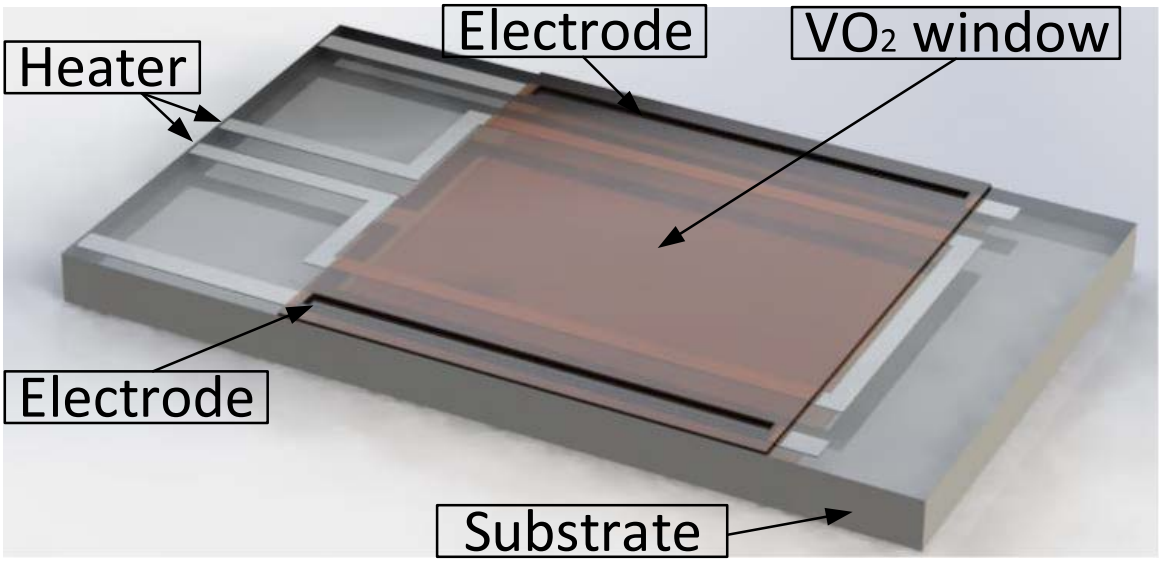

Figure 6.1: Schematic structure of the monolithic integrated μVOA design.

The monolithic μVOA design integrates electro-thermal actuation and sensing of VO_2

thin film material by using a resistive heater loop and electrodes as shown in **Figure** 6.1. This design aims to make this technology compatible with optical interconnects and decrease the response time by reducing the thermal mass. A SiO_2 (fused silica, double sided polished) substrate was selected based on its transmission for NIR (1550 nm) wavelengths. Platinum (Pt) metallization material was selected to sustain the VO_2 deposition temperature. The heater loop is used to induce the optical transition in the VO_2 window electro-thermally (i.e. using Joule heating). A temperature above the VO_2 transition temperature ($T_c \sim 68\,^{\circ}C$) is required inside the VO_2 window to complete the IMT. Finite element method (FEM) simulations were performed in Comsol Multiphysics to confirm the temperature distribution inside the window. VO_2 square windows of 400, 300, 200 and 100 μm^2 were considered for this design. **Figure** 6.2 shows the temperature distribution using the Joule heating module with a current of 35 mA. The non-uniformity of the temperature distribution increased with the size of the window, but a current of 35 mA resulted in a temperature higher than 68 °C at the center of all the four VO_2 windows.

The temperature was evaluated at the center of the VO_2 windows for comparing the different device sizes. **Figure** 6.3 shows this temperature as a function of the power input to the device. Power (I^2R) instead of current was compared because the heater resistance is different for each device. These results demonstrate lower power consumption for the smaller devices, as expected.

A die of 4 mm × 4.5 mm contained all four windows as shown in **Figure** 6.4. The four masks layers are: 1) metal (yellow), 2) SiO_2 etch (blue), 3) VO_2 pattern (purple), and 4) SiO_2 etch for contacts (green). (See **Figure** 6.4.)

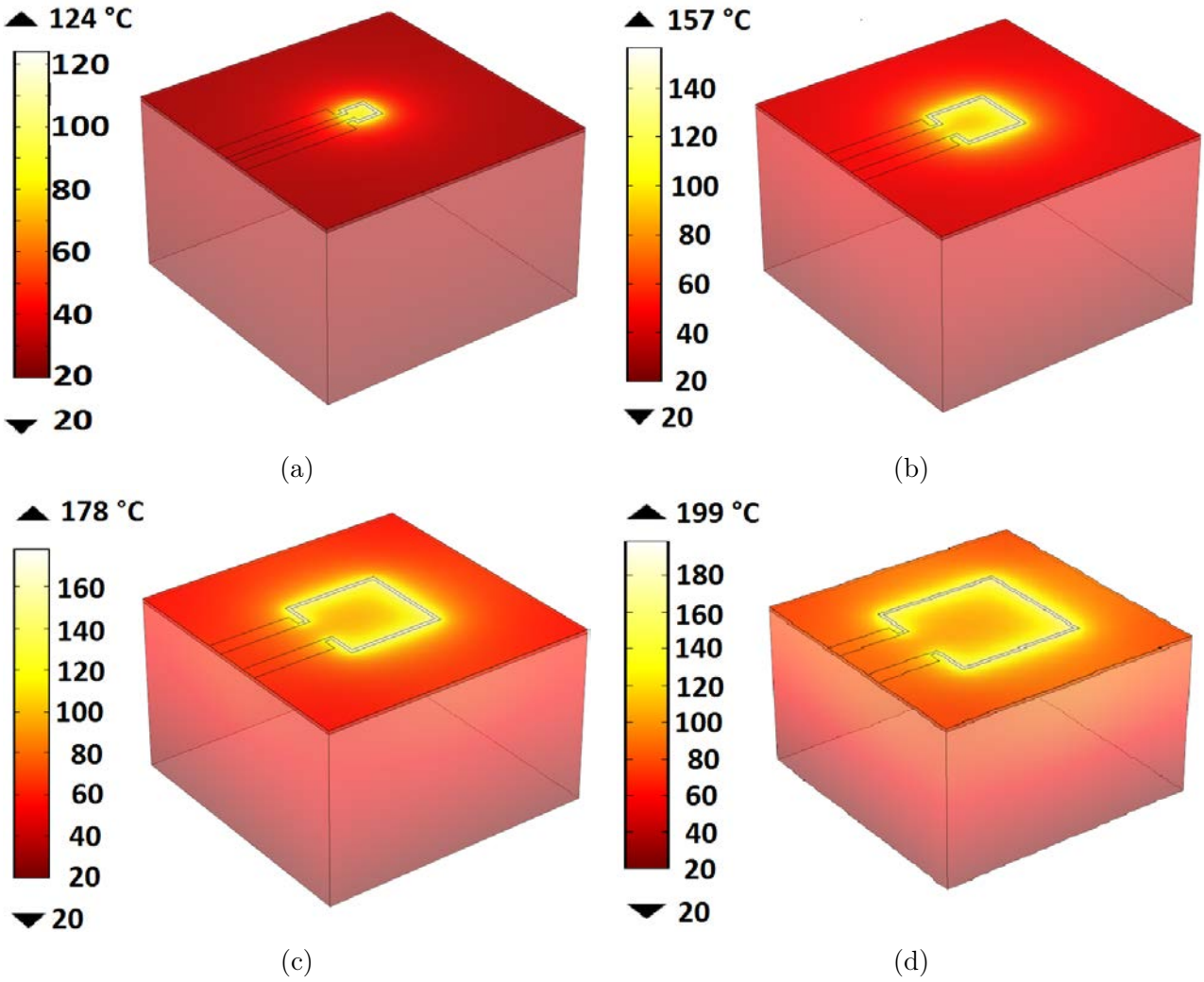

Figure 6.2: Temperature distributions for VO_2 square windows of a) 100 x 100 μm^2, b) 200 x 200 μm^2, c) 300 x 300 μm^2, and d) 400 x 400 μm^2 as simulated using Joule heating with a heater input current of 35 mA.

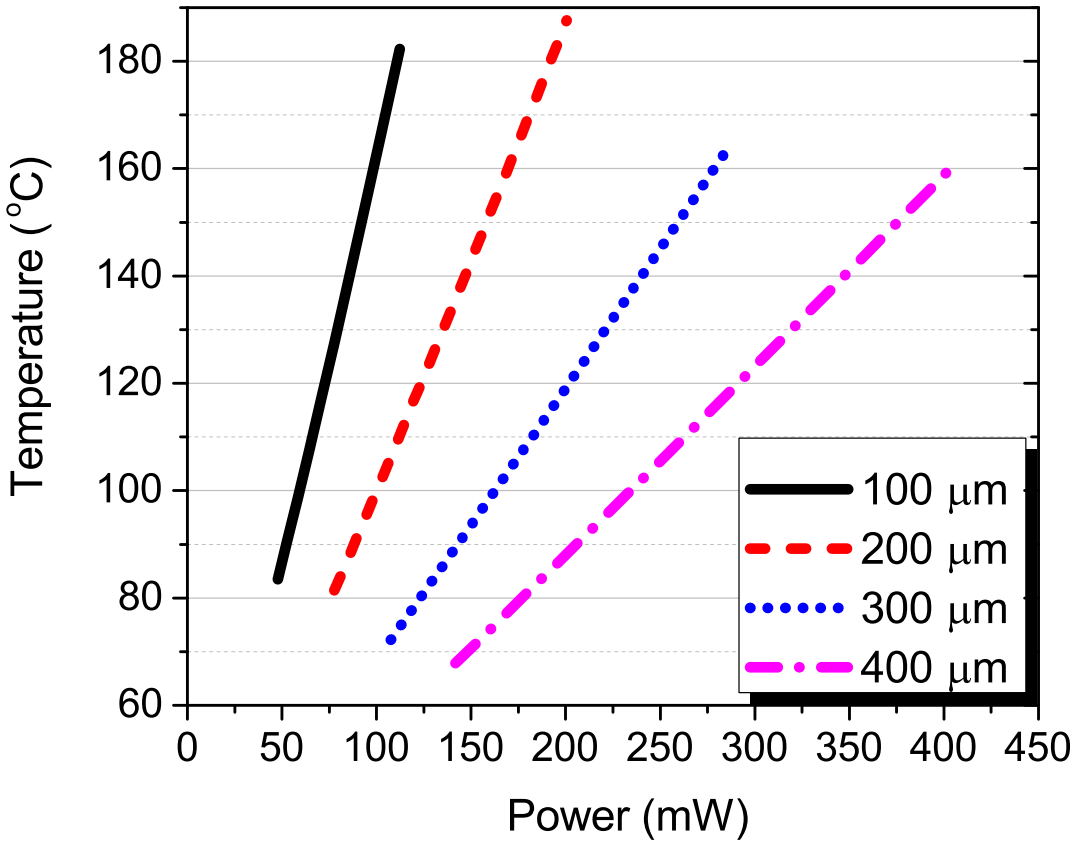

Figure 6.3: Simulated temperature at the center of the VO_2 window for all four devices. The electrodes were included in the simulation.

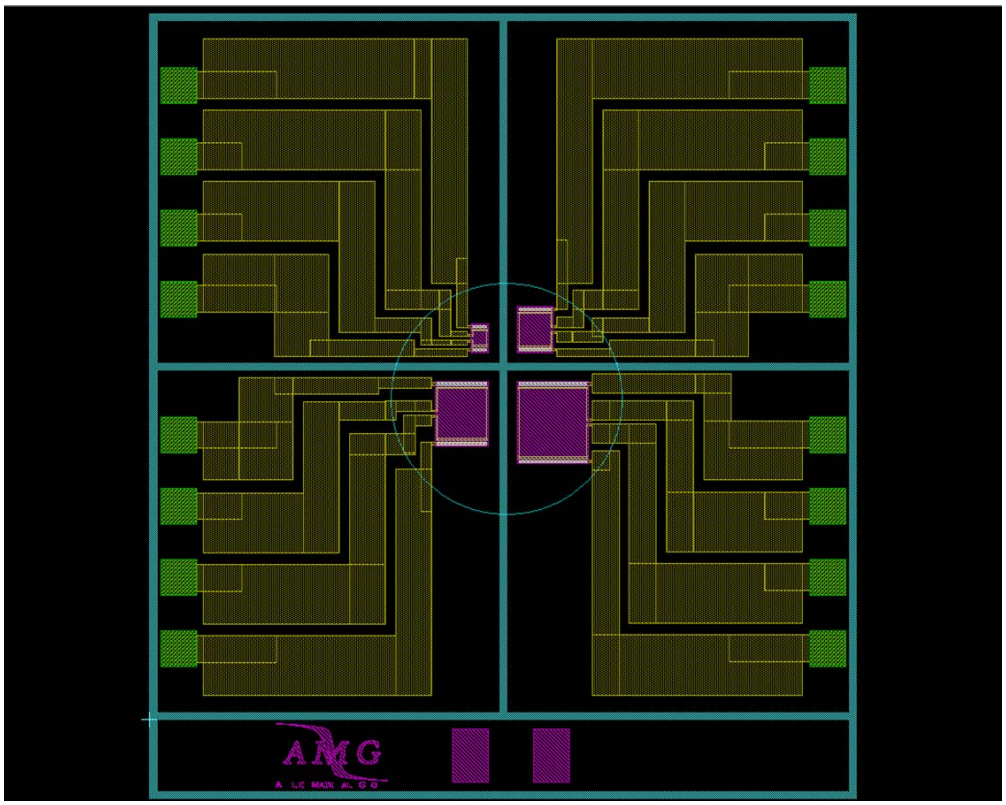

Figure 6.4: Mask design for the monolithic VOA micro device.

6.2 Device Fabrication

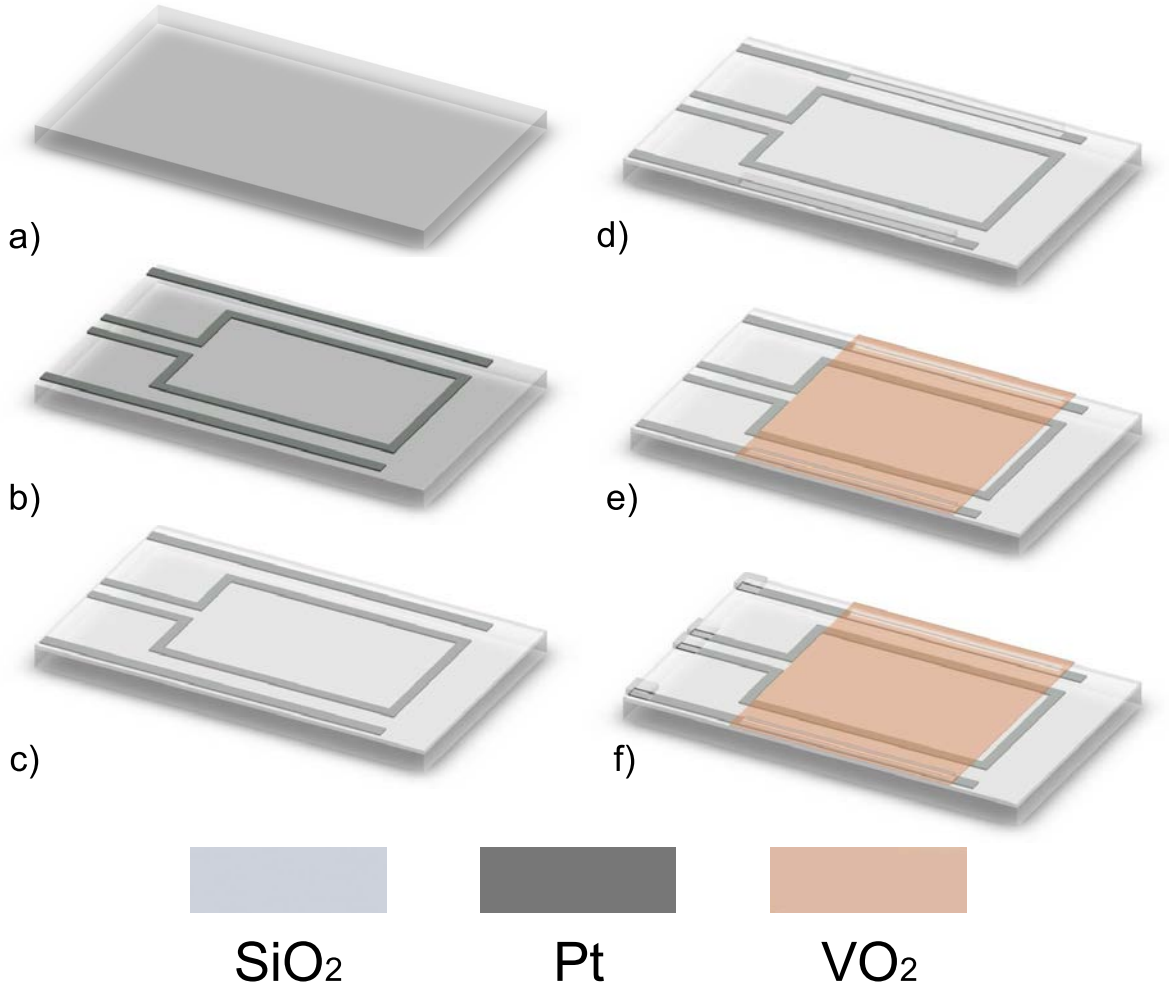

Figure 6.5: Fabrication process for the VO_2-based μVOA a) SiO_2 substrate, b) heater and electrodes metallization, c) SiO_2 insulating layer, d) opening to the electrodes, e) SiO_2 deposition and window patterning, and f) opening to contact pads for electrical connections.

The fabrication process for the μVOA devices is summarized in the steps shown in **Figure** 6.5. Four photomasks were required in the process. A double-sided polished $2''$ SiO_2 wafer (SOF50D05C2, MTI), 500 μm thick was used (step a). Metal evaporation and lift-off processes were used for the heater and electrodes Ti/Pt metallization with thicknesses of 400 Å/1500 Å, respectively (step b). The heater loop width and the gap between the heater and electrode is 10 µm. The electrodes width is 10 µm for 200 μm and 100 μm devices and

15 µm for the 400 μm and 300 μm devices.

An insulating layer of SiO_2 (∼400 nm thick) was deposited by plasma enhanced chemical vapor deposition (PECVD) in three consecutive steps of 133 nm each to prevent possible voids propagation through the SiO_2 thickness (step c). The SiO_2 layer was etched by reactive ion etching (RIE) to open electrical contact paths from the Pt electrodes to the VO_2 thin film (step d). A VO_2 layer, ∼170 nm thick, was deposited by PLD using a KrF laser operated at 10 Hz with ∼2 J/cm^2 fluence for 25 minutes (step e). The substrate was maintained at 595 °C under 15 mTorr O_2 pressure. This deposition step was followed by an annealing step under same pressure and temperature conditions for 30 minutes. The backside of the wafer was covered during the deposition to prevent undesired residuals accumulation on the substrate, which could have affected optical transmission experiments. VO_2 square windows were patterned by photolithography process and RIE (step e). Another SiO_2 etching step (f) was done to open contacts pads to the heater and electrodes. Finally, the 2" wafer was diced into dies of approximately 4 x 4 mm^2.

Figure 6.6 and **Figure** 6.7 show scanning electron microscope (SEM) images and optical microscope (Keyence VHX-S15) images of the fabricated devices.

6.3 Experimental Setup

The electro-optical setup shown in **Figure** 6.8 was used to test the μVOA devices by using a free-space configuration, similar to that described in [45]. The die containing the μVOAs was mounted and wire-bonded into a circular package with a centered-hole, as shown in the **Figure** 6.8 inset. A custom made PCB with a centered-hole was build to fit the circular package, route the electrical connections, and act as a sample holder. The PCB was mounted on a X-Y-Z translational stage to align the NIR laser beam with normal incidence on the VO_2 windows. The NIR diode laser (λ = 1550 nm, FPL1055T) was operated at its minimum stable power of ∼25 mW and focused by a lens (f =15 mm) on the VO_2 window. A minimum diameter of ∼70 µm was achieved as shown in **Appendix B: Additional testing for VO_2-**

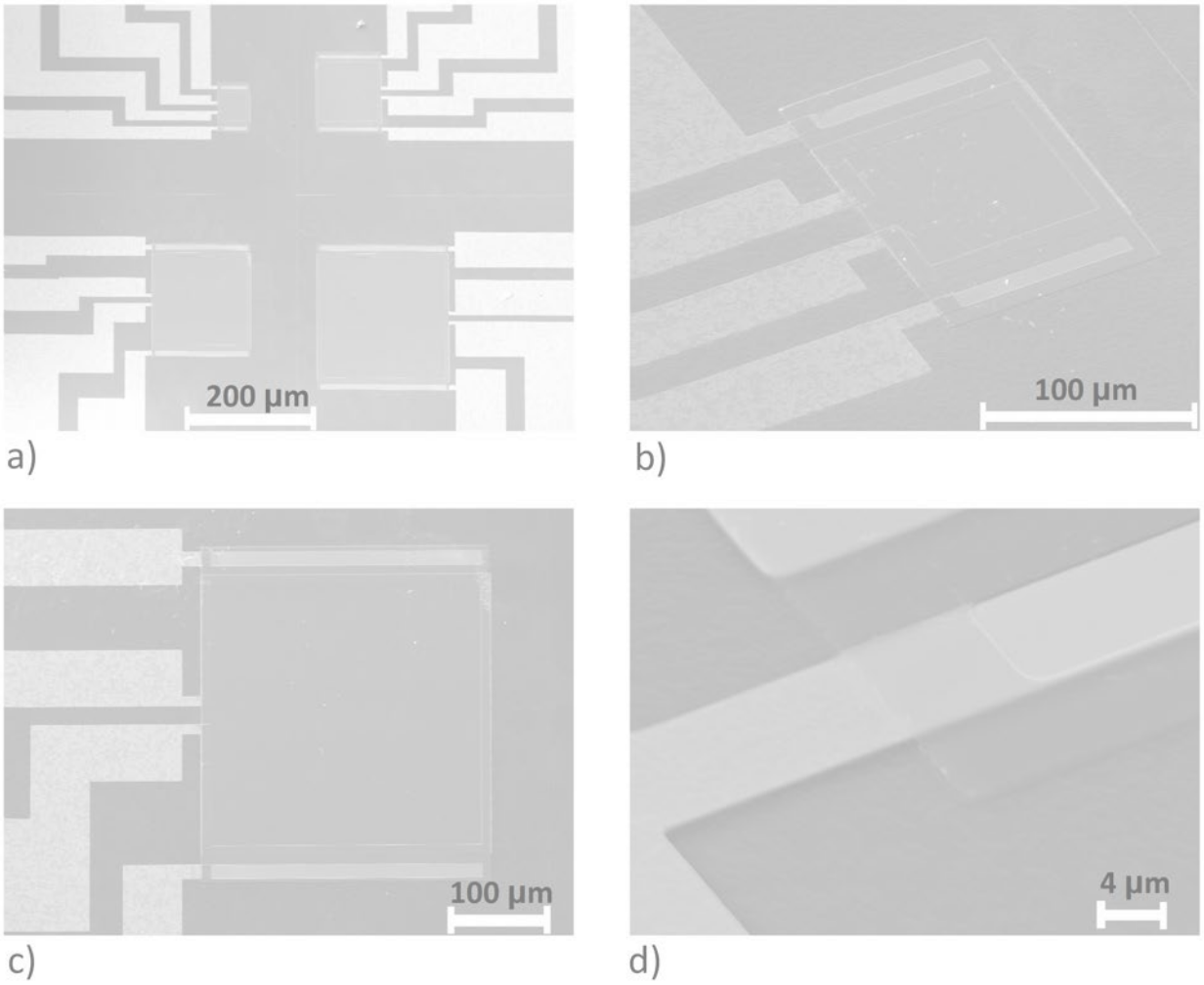

Figure 6.6: SEM images of the fabricated VO_2 devices

based μVOA. The lens was mounted on a micro positioner to manipulate the distance between the μVOA and the focusing lens, thus, allowing control of the beam diameters on each window. A neutral density (ND) filter between the lens and the laser was used to further reduce the laser intensity. The transmission curves were measured for different NDs (see **Appendix B: Additional testing for VO_2-based μVOA**). The filter was adjusted to 2 optical density (OD) for the 100 μm and 200 μm devices measurements, 1 OD for 300 μm and to 0.6 OD for 400 μm device. A laser beam profiler (LBP) was used to assist in the alignment of the focused laser beam. After this alignment the LBP was replaced by an optical sensor (S144C, Thorlabs) connected to a power meter (PM100D, Thorlabs), which

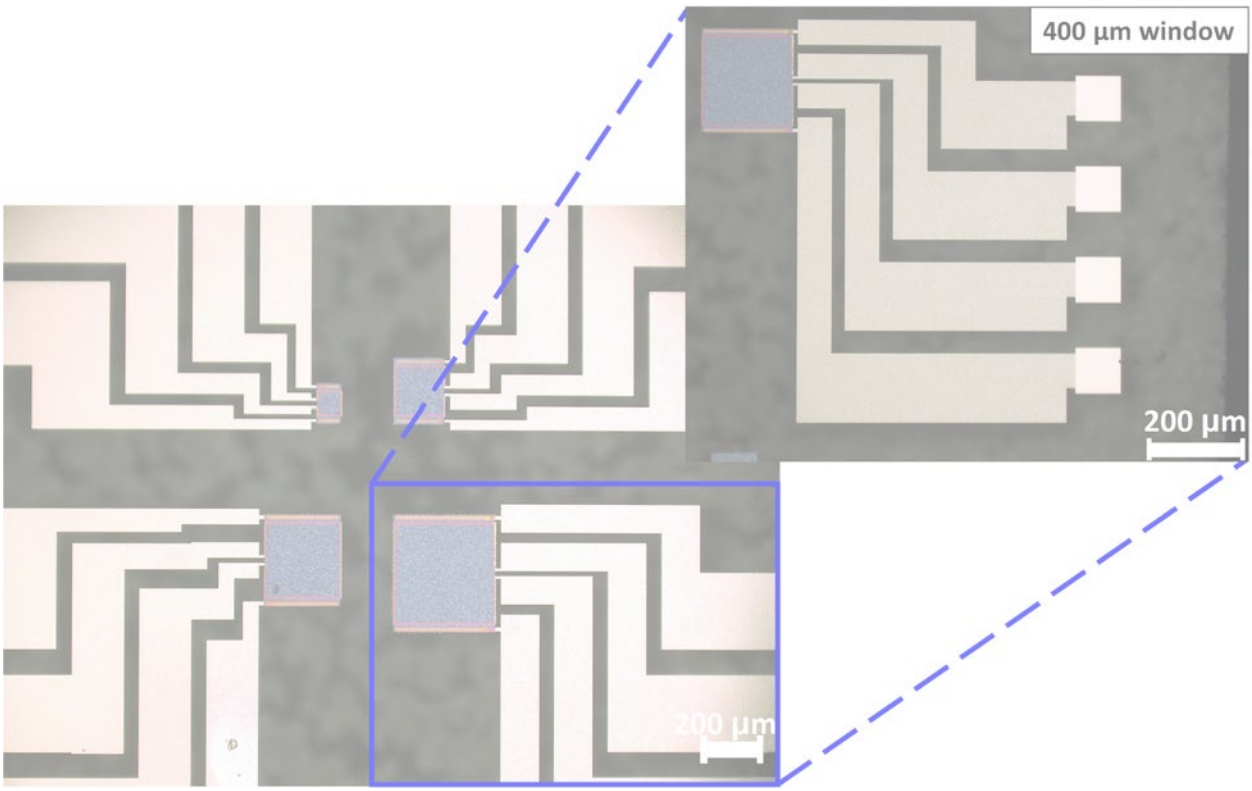

Figure 6.7: Optical microscope images of the fabricated VO_2 devices

communicates with a Labview computer interface during the measurements.

Electrical contacts on the PCB were used for data acquisition and control (cRIO, National Instruments). The heater current (I_H) drives the device while the voltage across the VO_2 (V_R) was measured. V_R was used to calculate the VO_2 resistance (R_{VO2}) by using a voltage divider as shown in **Figure** 6.8. A series resistor of $R_s = 22\,\text{k}\Omega$ and supply voltage of $V_C = 2\,\text{V}$ were selected to measure the VO_2 resistance and prevent self-heating on the VO_2 thin film. This setup allowed to sense the VO_2 resistance change and drive the device heater simultaneously in a closed-loop configuration. This allows to electronically control the transmission for NIR wavelengths through a VO_2 window. The sampling rate for electrical measurements and actuation was set to 50 µs (which is much faster than the system response time), while the optical sensing was limited to 50 ms due to the sensor bandwidth.

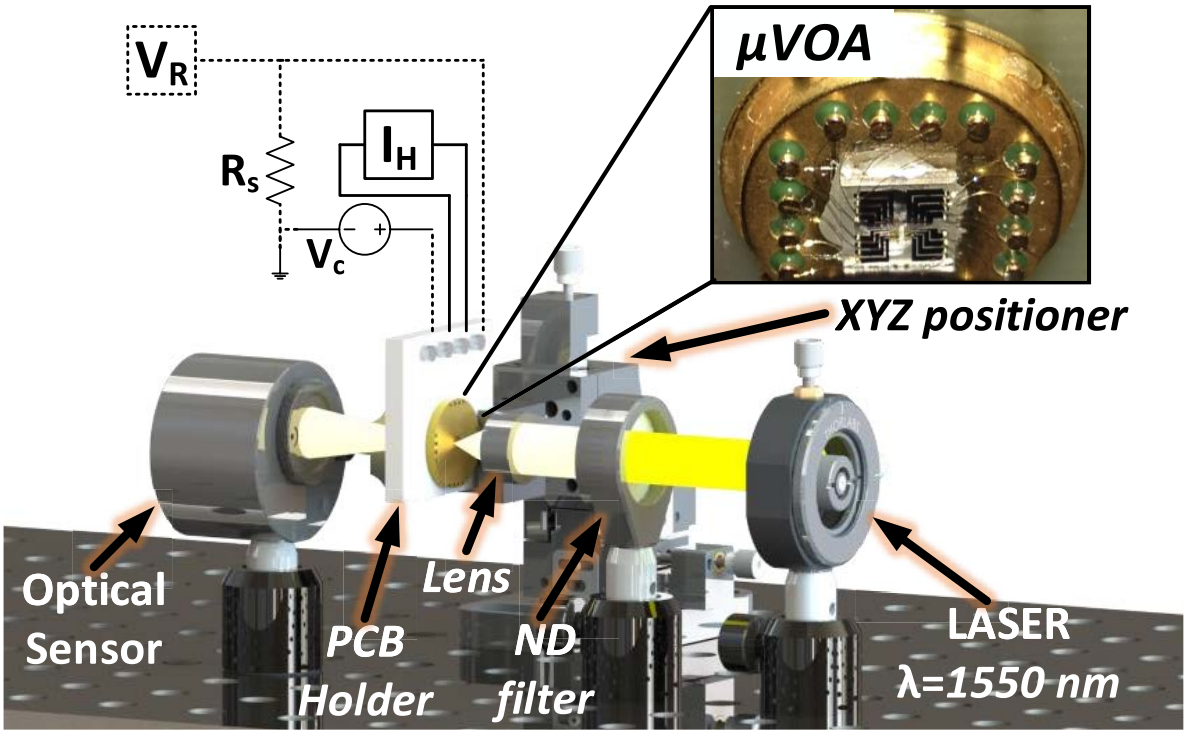

Figure 6.8: Electro-optical setup used for testing the μVOAs devices.

6.4 Results and Discussion

The electrical time constant of the devices was measured to determine the required sampling rate for further experiments. The time constant was calculated by measuring V_R for each device for a current step input (I_H) (refer to **Figure** 6.8). **Figure** 6.9 a shows the response for the 100 μm device. Similar step responses were obtained for the other devices.

We considered the time constant after the step impulse (when the device is 'ON', τ_{ON}) and when the step is released (τ_{OFF}).Due to limitations in the experimental setup, we only measured the electrical time constant, τ. However, we anticipate the electrical and optical time constants to be very similar, since the optical and electrical transitions in VO_2 are strongly correlated. **Figure** 6.9.b shows how both time constants (τ_{ON} and τ_{OFF}) decrease with device size. The values for τ_{OFF} and τ_{ON} decrease from 524 ms to 71.4 ms, and from 160 ms to 16.8 ms, respectively. The larger τ_{OFF} indicates that the response of electro-

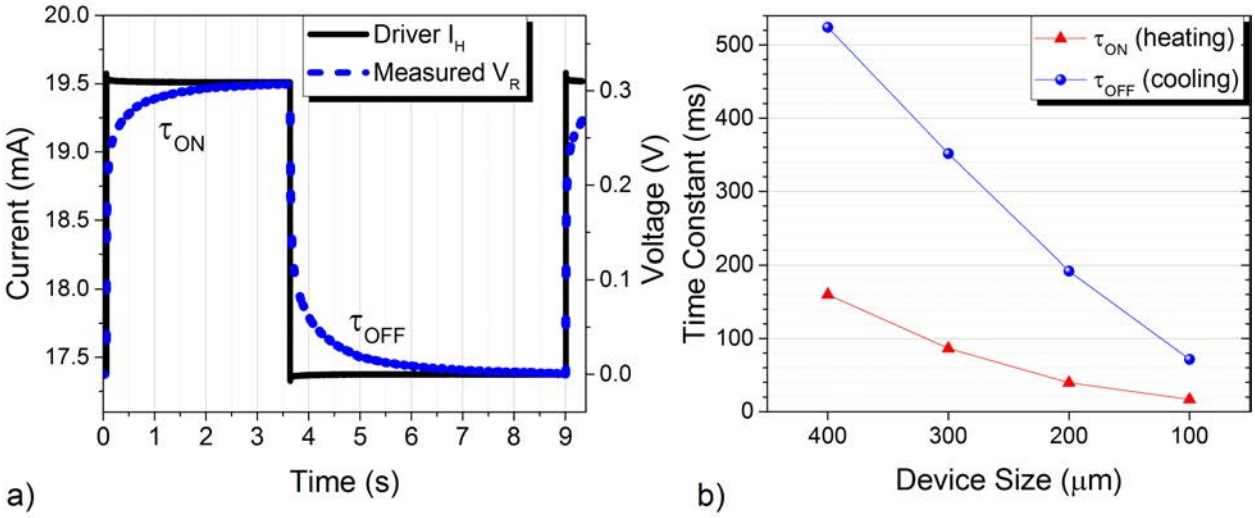

Figure 6.9: Time constant measurements: a) 100 µm device response (V_R) to a step input (I_H) and b) time constant for the scaling down of the μm devices.

thermal actuation in these devices is dominated by heat dissipation during cooling.

The electro-thermal actuation and temperature distribution was investigated by IR thermal imaging (OptoTherm, InfraSight MI320). The devices were actuated electro-thermally to their maximum current limit (I_H) as determined by IMT characterization experiments. **Figure** 6.10 shows the temperature of the four devices as a function of the heater current (I_H). This temperature is an average of a region outside the VO_2 window (labeled as #2 on the inset in **Figure** 6.10). Evaluating the temperature inside the VO_2 window will give an incorrect value since VO_2 emits less thermal radiation for temperatures above the IMT [146]. The maximum temperature was 108.4 °C, 101.6 °C, 102.7 °C and 104.8 °C for 400 μm, 300 μm, 200 μm and 100 μm device, respectively.

The VO_2 thin film was characterized by simultaneously measuring its optical and electrical transition as shown in **Figure** 6.11. The VO_2 resistance drops more than 3 orders of magnitude for all devices, resulting in a resistance ON/OFF ratio ($R_{25\,°C}/R_{100\,°C}$) of 2.22k, 2.16k, 1.56k and 1.76k for the 400 μm, 300 μm, 200 μm and 100 μm device, respectively. The average resistance drop is from 685 kΩ to 367 Ω having an average resistance ON/OFF ratio of $\sim$ 1.9k.

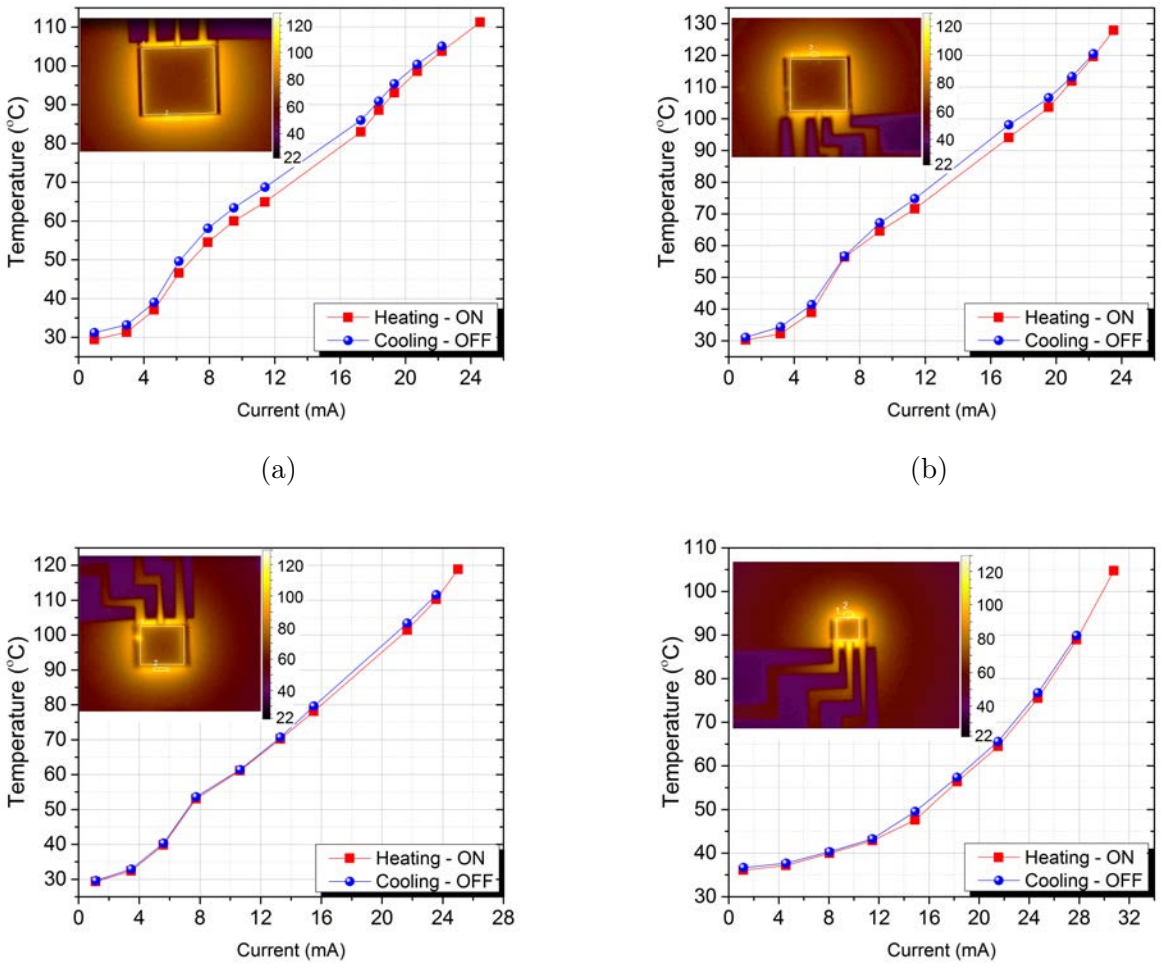

Figure 6.10: Temperature as a function of current for electro-thermal actuation in the VO_2 device of a) 400 μm, b) 300 μm, C) 200 μm, and d) 100 μm. Inset shows IR image during actuation at ~30 mA.

During these measurements the maximum current applied to the device was limited to 29.7, 28.7, 22 and 32.7 mA for the 400, 300, 200 and 100 μm device, respectively.

The intensity of the NIR laser on each device was adjusted by changing the neutral density filter OD and the lens position. The filter OD was selected by measuring the VO_2 resistance before and after turning on the NIR laser until no change was detected. The transmitted power at 25 °C were 11.94 mW/mm^2, 20.37 mW/mm^2, 3.31 mW/mm^2 and 9.93 mW/mm^2 for the 400 μm, 300 μm, 200 μm and 100 μm, respectively.

The transmission in **Figure** 6.11 was normalized with respect to the transmitted power at 25 °C to demonstrate the transmission drop due to the device. The insertion losses (before the IMT) of -3.6 dB, -3.9 dB, -3.4 dB and -4.6 dB were measured for the 400, 300, 200 and 100 μm devices, respectively. The highest insertion losses were measured for the 100 μm device. The irradiated power on the 100 μm device was not reduced any further by a ND filter since the power readings from the sensor would have been near its resolution limit. It can be noticed in **Figure** 6.11 that the performance in terms of minimum transmission and total transmission drop was similar between the two larger and the two smaller devices.

The strong correlation between the electrical and optical transition in VO_2 is observed

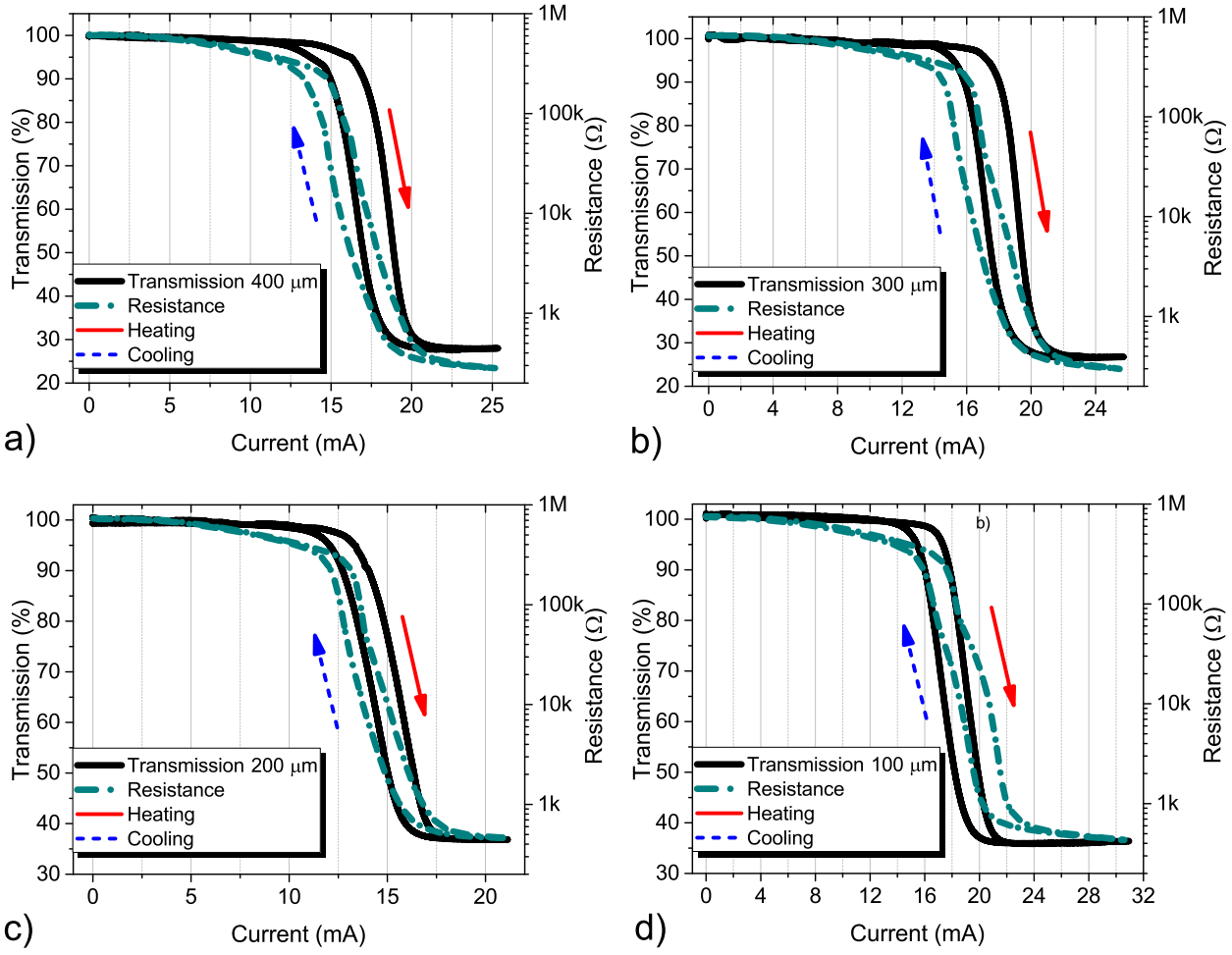

Figure 6.11: Simultaneous measurement of the electrical and optical transition in VO_2 windows for a) 400 μm, b) 300 μm, c) 200 μm, and d) 100 μm device.

by plotting the transmission percentage (%T) as a function of its resistance. **Figure** 6.12 shows this correlation for the devices using the same results presented on **Figure** 6.11. This data was fitted into a correlation model (sigmoidal, bidose model) with an $R^2 \geq 0.99$ for each device. The %T is calculated using the bidose equation from Origin Lab Software,

$$\%\mathrm{T} = A_1 + \left(\frac{p(A_2 - A_1)}{1 + 10^{[X_1 - \mathrm{Log(R)}]h_1}} + \frac{(1-p)(A_2 - A_1)}{1 + 10^{[X_2 - \mathrm{Log(R)}]h_2}} \right) \tag{6.1}$$

where R is the VO_2 resistance, A_1, A_2, X_1, X_2, h_1, h_2 and p are fitting parameters. Matlab curve fitting was used to determine the best fitting parameters for each device. These parameters are shown in **Figure** 6.12 for each device. It can be observed from **Figure** 6.12 that the shape of the correlation curves changes as the device scales down in size.

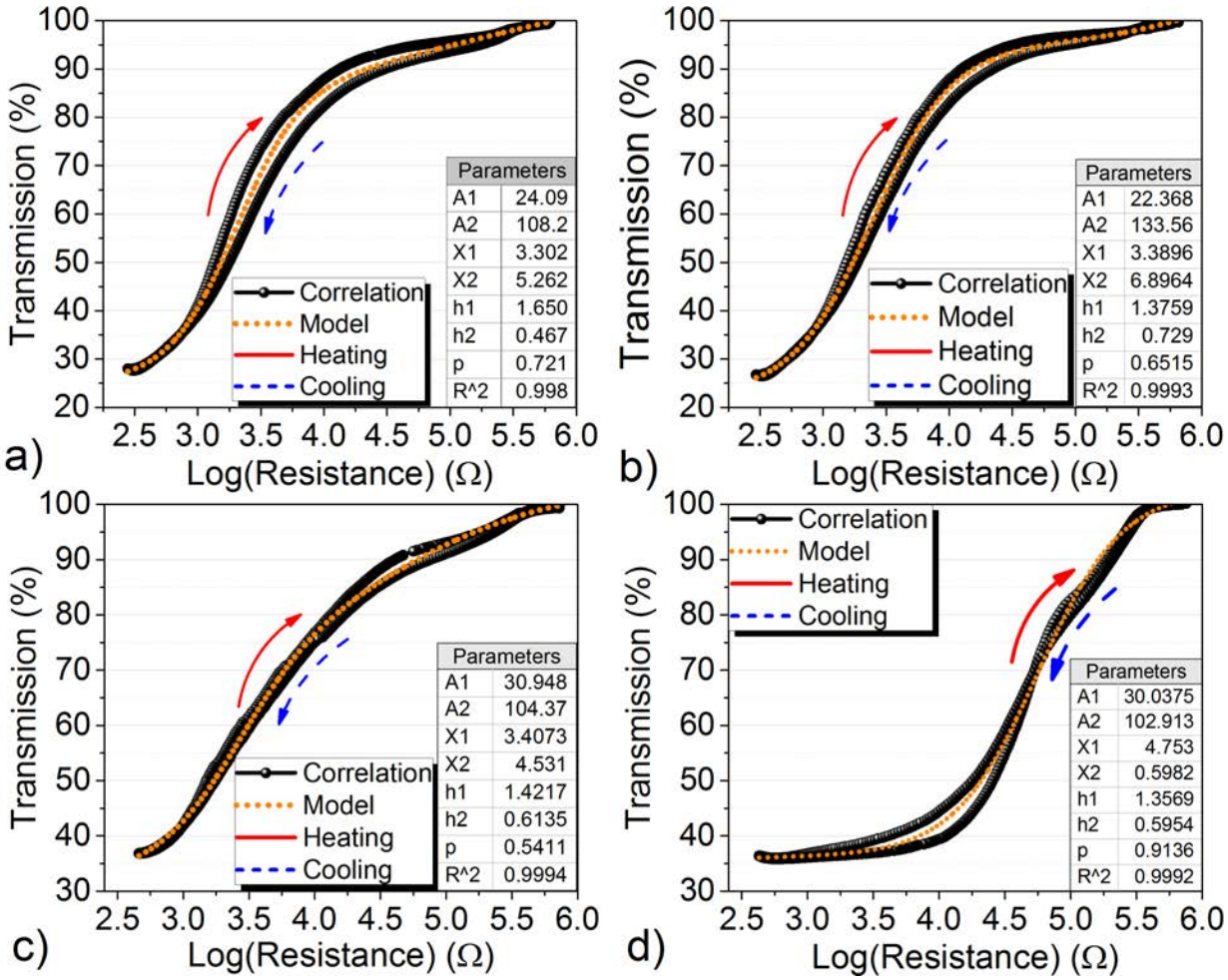

Figure 6.12: Electro-optical VO_2 correlation and bidose self-sensing model.

The bidose model was chosen based on the function implementation in the data acquisition system. Other sigmoid functions such as the double Boltzmann equation can be use to fit this data. However, the bidose model produced the best fit for the measured data in these experiments.

This correlation model allows for the estimation of the measured transmission % ($\%T_m$) by sensing the VO_2 resistance (R_{VO2}) thus allowing for self-sensing model. The difference between the measured data and the self-sensing model is shown in **Figure** 6.13. Table 6.1 shows a summary for these correlation errors. The 400 μm device has the higher errors while the 200 μm device has the lowest. The 300μm and 100 μm devices have a similar behavior,

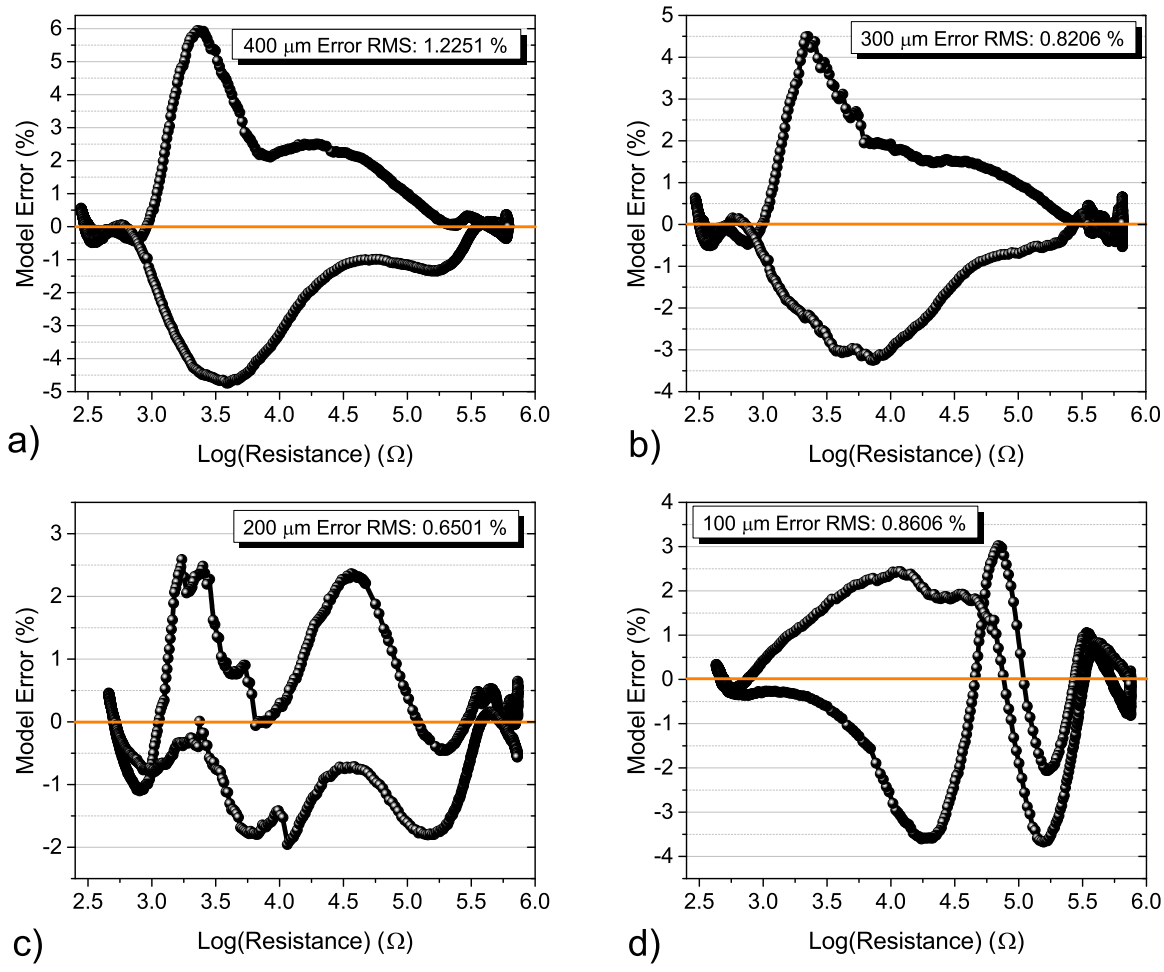

Figure 6.13: Correlation model error between calculated transmission % (zero line) and measured data.

both with a RMS error of ~ 0.8 %.

Table 6.1: Correlation Error for all devices

Device Size (μm)	Maximum Error (%)	Minimum Error (%)	RMS Error (%)	Average Error (%)
400	5.9	-4.7	1.22	-6.9×10^{-6}
300	4.5	-3.3	0.82	2.2×10^{-5}
200	2.5	-1.96	0.65	3.1×10^{-8}
100	3	-3.7	0.86	-3.3×10^{-3}

This self-sensing model was used to estimate the transmission $\%T_{ss}$ by measuring R_{VO2} in the μVOA and complete a closed-loop (CL) system as shown in **Figure** 6.14 block diagram.

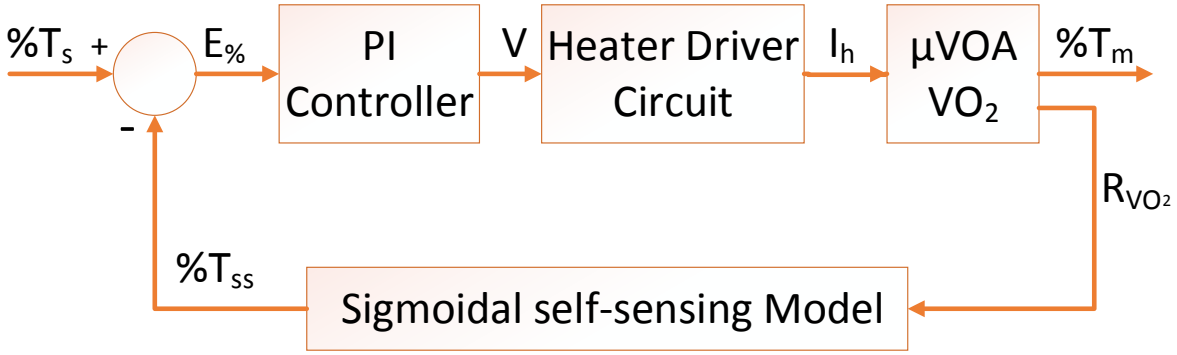

Figure 6.14: Transmission closed-loop control block diagram.

The error between the transmission set point ($\%T_s$) and $\%T_{ss}$ was minimized by a proportional-integral (PI) controller. The PI gains were obtained experimentally for each device size. The output voltage (V) from the PI controller was converted into a current (I_H) by an external circuit, which drives the integrated heater of the μVOA. Using this control technique, $\%T_m$ was electronically controlled as its transmission % and the resistance changed as a function of I_H.

The CL results for the μVOAs are shown in **Figure** 6.15. $\%T_s$ changes in 1 s steps from 100 % to 40 %. **Figure** 6.16 shows the error for the measured signal and the self-sensed

signal. The self-sensed signal follows the setpoint for all devices minimizing the steady-state error. Table 6.2 shows the closed-loop errors for all devices.

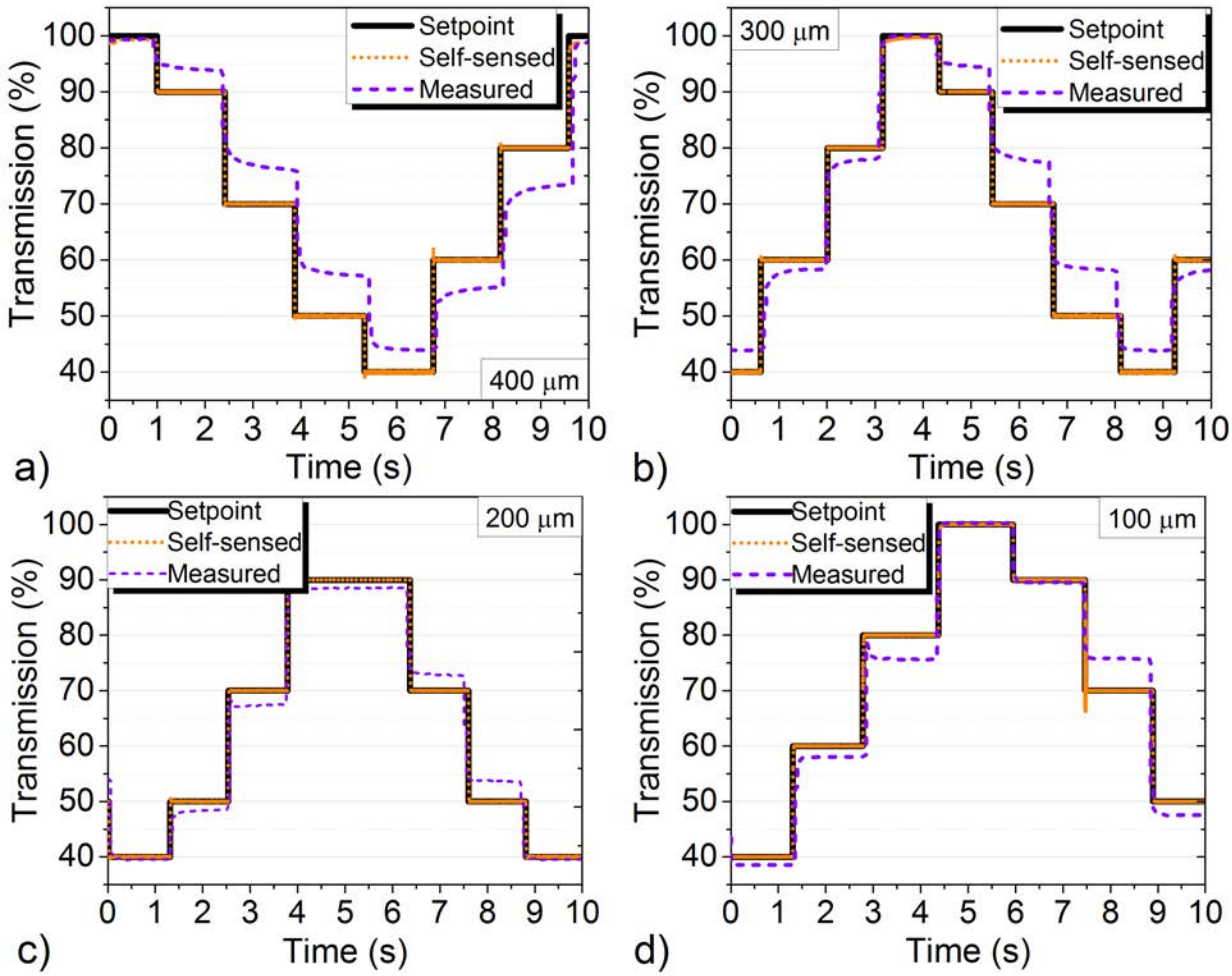

Figure 6.15: Closed-loop results for: a) 400 μm, b) 300 μm, c) 200 μm and d) 100 μm device.

Table 6.2: Closed−loop Error

Device Size (μm)	Maximum Error (%T)	Steady-state Error (%T)	Average Error (%T)
400	7	1.63	1.32
300	8	3.01	3.53
200	4	0.03	-0.23
100	6	0.71	-0.39

The 300 μm device shows a maximum CL error of ∼8 % and a maximum average error of 3.53 %. However the 400 μm device has a slightly higher RMS error. The transmission

for these devices (400 and 300 μm) was stable within 1 s (difficult to see from these results). The 400 μm device and the 300 μm were tested with 1.5 s switching intervals to allow more time for stabilization due to their slower time constants. These showed results similar to those presented. The results for the 200 μm device shows the lowest RMS and average errors of 3.15 % and -0.23 %, respectively. The 400 μm and 300 μm devices resulted in higher error $\sim$7-8 % during CL control. The 100 μm device showed $\sim$6 % of error during CL.

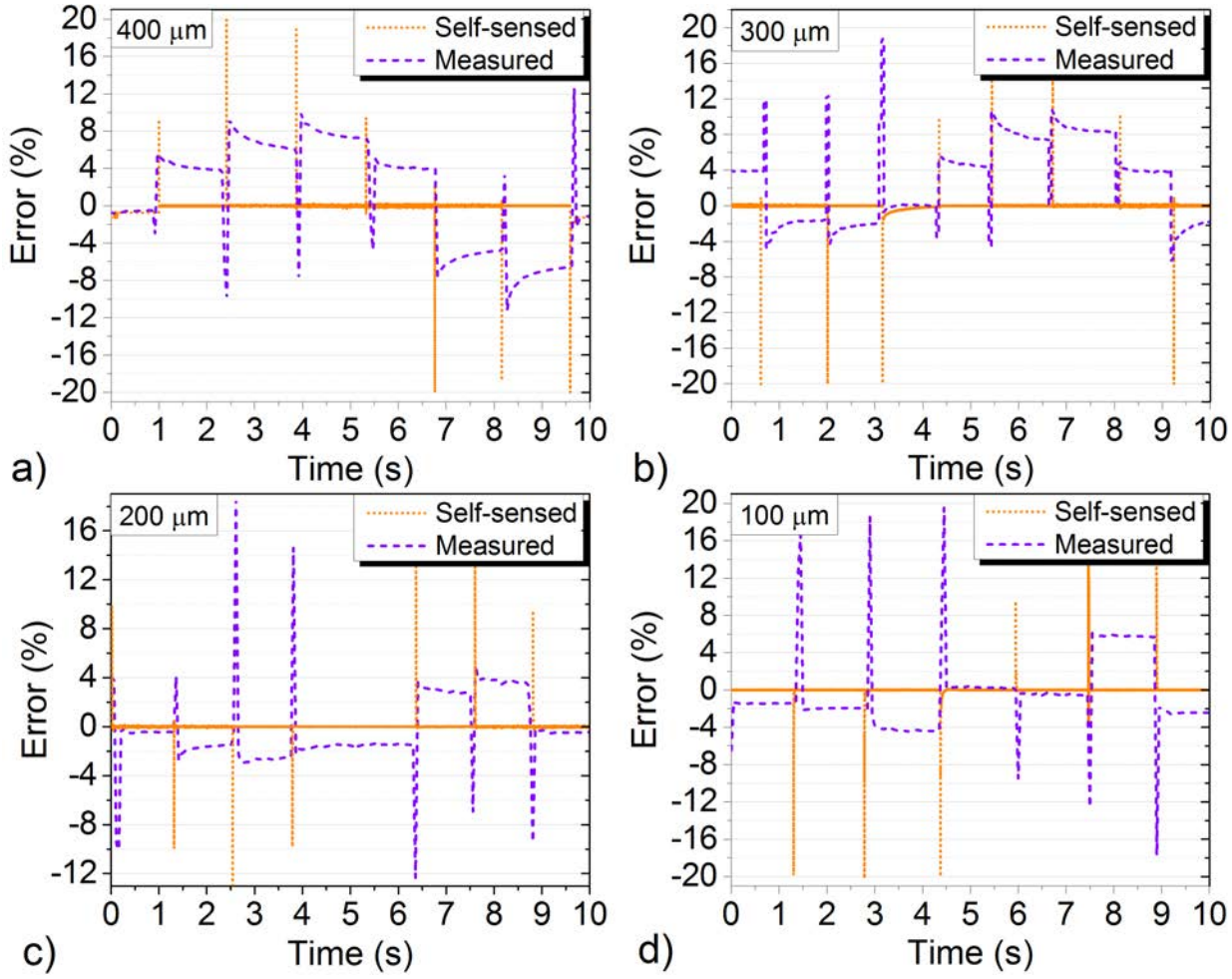

Figure 6.16: Self-sensed and measured signal errors with respect to the setpoint during closed-loop experiments for a) 400 μm, b) 300 μm, c) 200 μm and d) 100 μm devices.

6.4.1 Power consumption

The power consumption was compared for these μVOA devices shown in Table 6.3. The heater resistance was measured across the heater contact pads at room temperature. The current value used in the calculation was that of the intersection point of the heating and cooling curves after the IMT, which was obtained from **Figure** 6.11 for the four VOAs. The results show a lower power consumption as the device gets smaller, with the exception of the 200 μVOA device.

Table 6.3: Power Consumption

Device Size (μm)	Heater resistance (Ω)	Current (mA)	Consumed Power (mW)
400	165.5	21.63	77.43
300	132.1	22.25	65.40
200	97.8	18.4	33.11
100	66.2	23.5	36.56

6.5 Summary

Four monolithically integrated VO_2-based μVOAs of 400, 300, 200 and 100 μm^2 windows were investigated. The strong correlation between the electrical and optical transition in VO_2 was used to determine a self-sensing model with specific fitting parameters for each device size. Similar fitting parameters were used for the 400, 300 and 200 μm devices. However the 100 μm device correlation curve showed a sharp positive slope requiring different parameters. The 200 μm device showed the lowest self-sensing model error of 2.5 % and a steady state error of 0.03 %.

This self-sensing model enabled the electronically control of the transmission % for a NIR laser (1550 nm) through a VO_2 window for all devices. These VO_2-based μVOAs can be calibrated for different laser intensities as demonstrated in this work, with better transmission % control at low intensities ($\sim$3.31 mW/mm^2). These can be calibrated for a range of near-IR wavelengths from 900 nm to 2500 nm including fiber optics transmission bands O-band, C-band and L-band. Furthermore, this small scale devices could be extended into a large scale VOA array similar to MEMS-based VOA array but reducing the complexity of the fabrication process [147].

Closed-loop (CL) control of the transmission % was achieved for all devices. However, the 200 μm device showed a better performance during CL control with the lowest average CL error of 0.23 %. The transmission % drop of the VO_2 thin film (up to $\sim$30 %) could be affected by the optical quality of the SiO_2 substrate (fused silica), the VO_2's optical quality as grown on SiO_2 insulating layer deposited by PECVD or interface reflections of the SiO_2/VO_2/air device layers. Especially, the VO_2 thin film thickness has a direct impact in these reflections [148].

CHAPTER 7

SUMMARY

7.1 Summary of Contributions

VO_2 sol-gel deposition process was investigated for growing VO_2 thin films on 4 inches wafers. Films growth by this process were compared with pulsed laser deposition (PLD) process. Two devices were developed using PLD grown VO_2 thin films.

The development of a near-IR (NIR) image projector and a NIR variable optical attenuator (VOA) are presented in this work. VO_2 thin film material was used to store an image in form of localized induced transition by photo-thermal actuation. The reversible nature of the optical transition in VO_2 allows to consecutively program images into the VO_2 thin film and project them in the NIR region (λ=1550 nm). The image programming speed, resolution and optical contrast were characterized for this projector.

The simultaneous measurement of the optical and electrical properties of VO_2 demonstrated the strong correlation between these two properties, which enable the hysteresis reduction by sensing its electrical resistance. A relatively simple self-sensing model was used control the optical transmission through the VO_2 thin film. A monolithic VOA compatible with optical fiber systems was developed.

7.2 List of Problems Solved in this thesis

This dissertation addresses the following:

1. Characterize the composition, crystallization, topography, electrical, and optical transitions of VO_2 thin films deposited by sol-gel process in 4 inches wafers.

2. Use of photo-thermal actuation to program, store and project a NIR image.

3. Characterize the contrast, programming speed and resolution of the developed VO_2-based image projector.

4. Demonstrate hysteresis reduction in the optical transmission of VO_2 by sensing its electrical resistance, enabled by the material's strong correlation.

5. Developed a monolithic variable optical attenuator (VOA).

6. Demonstrate self-sensing feedback control in the developed VO_2-based VOA.

7. Characterize the VO_2-based VOA based on its attenuation performance.

APPENDICES

Appendix A: Composition study for VO_2 thin films by sol-gel

The composition of the VO_2 sol gel deposited thin films was studied by Raman spectroscopy. Samples were analyzed for SiO_2 and SiO_2/Si substrates near the presented optimum temperature. The spectrum was measures for different ranges 100-800 $(1/cm)$ and 100-1100 $(1/cm)$. This data was obtained using a wavelength of 532 nm.

Figure A.1 shows the Raman spectrum of VO_2 deposited on a SiO_2 substrate at 417 °C. The spectrum shown in **Figure** A.2 corresponds to a sample annealed at a slightly higher temperature of 428 °C. Peaks from the V_2O_5 spectrum [149] were observed for this sample. **Figure** A.3 shows the spectrum for mixed phases of Vanadium-Oxides, having peaks from V_2O_3 and V_2O_5. This sample was annealed at 450 °C.

The results for thin films on SiO_2/Si substrates show the reduction process as the temperature increases. **Figure** A.4 shows V_2O_5 mixed peaks for a sample annealed at 406 °C. **Figure** A.5 also shows a V_2O_5 mixed phase peaks for an annealing temperature of 439 °C. **Figure** A.6 shows the VO_2 spectrum over SiO_2/Si substrates when annealed at 439 °C. At T $\geq$ 439 °C VO_2 thin film will degrade.

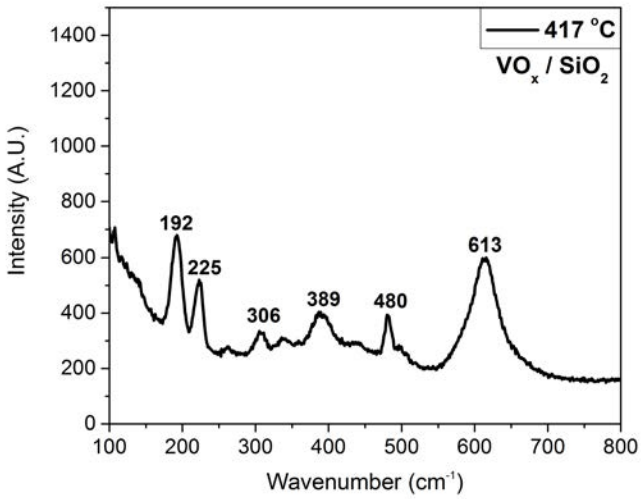

Figure A.1: Raman spectrum for VO_x/SiO_2 deposited samples by sol-gel annealed at 417 °C for 2 hrs under a pressure of 37 mTorr.

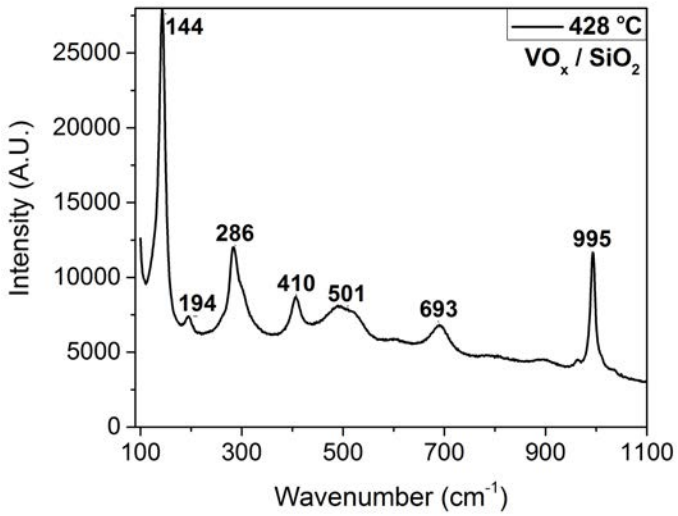

Figure A.2: Raman spectrum for VO_x/SiO_2 deposited samples by sol-gel annealed at 428 °C for 2 hrs under a pressure of 37 mTorr.

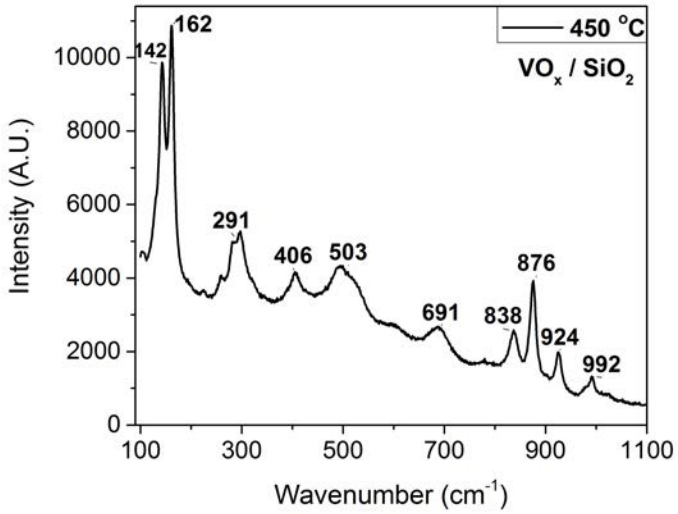

Figure A.3: Raman spectrum for VO_x/SiO_2 deposited samples by sol-gel annealed at 450 °C for 2 hrs under a pressure of 37 mTorr.

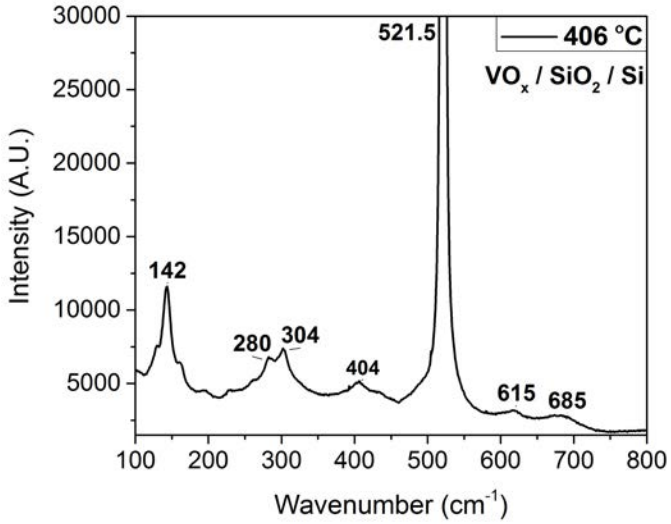

Figure A.4: Raman spectrum for $VO_x/SiO_2/Si$ deposited samples by sol-gel annealed at 406 °C for 2 hrs under a pressure of 15 mTorr.

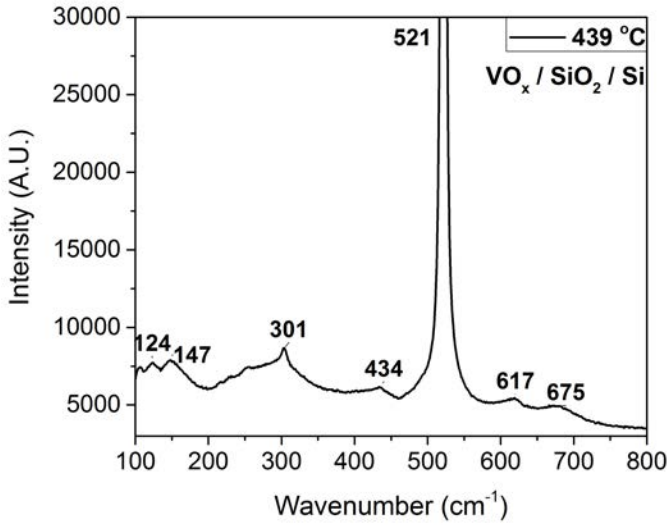

Figure A.5: Raman spectrum for $VO_x/SiO_2/Si$ deposited samples by sol-gel annealed at 439 °C for 2 hrs under a pressure of 15 mTorr.

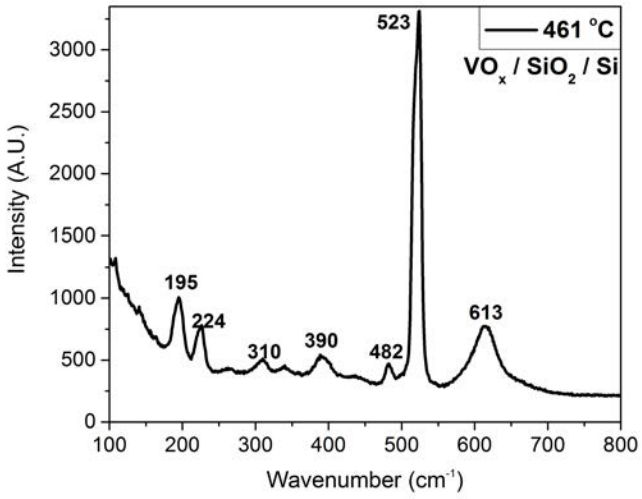

Figure A.6: Raman spectrum for $VO_x/SiO_2/Si$ deposited samples by sol-gel annealed at 461 °C for 2 hrs under a pressure of 15 mTorr.

Appendix B: Additional testing for VO_2-based μVOA

Smallest ($\sim$70 μm) laser spot size achieved for testing the μVOA device in shown in **Figure** B.1.

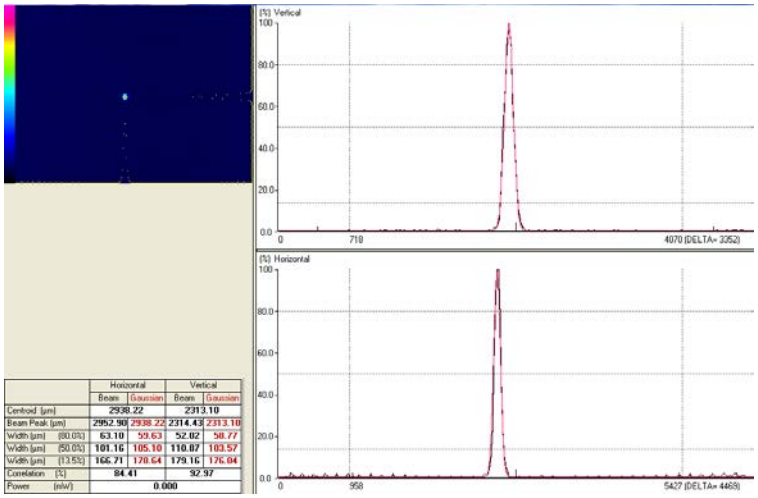

Figure B.1: Minimum spot size diameter (70 µm) achieved by the electro-optical setup.

The transmission through the 200 μm VO_2 window for different ND filters is shown in **Figure** B.2.

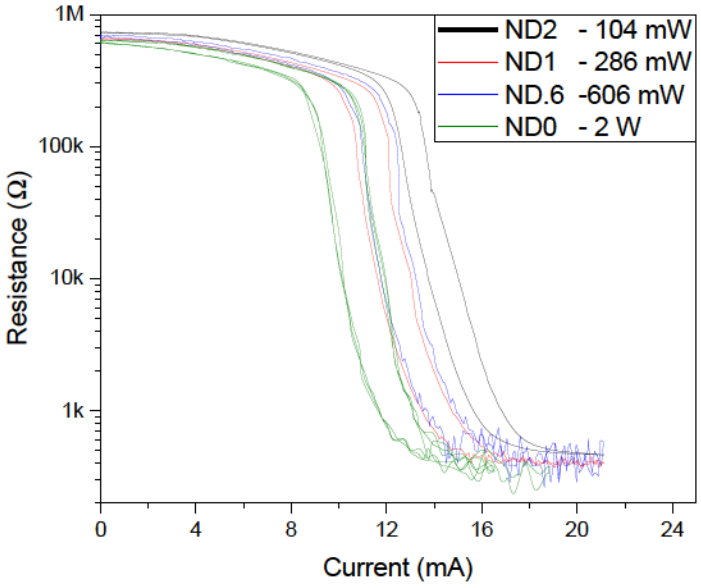

Figure B.2: VO_2 resistance as a function of heater driven current for different irradiated optical power on the 200 μm device

BIBLIOGRAPHY

BIBLIOGRAPHY

[1] F. Morin, "Oxides which show a metal-to-insulator transition at the neel temperature," *Physical Review Letters*, vol. 3, no. 1, pp. 34–36, 1959.

[2] X. Yi, S. Chen, Y. Wang, B. Xiong, and H. Wang, "VO_2-based infrared microbolometer array," *International Journal of Infrared and Millimeter Waves*, vol. 23, no. 12, pp. 1699–1704, 2002.

[3] J. C. C. Fan, H. R. Fetterman, F. J. Bachner, P. M. Zavracky, and C. D. Parker, "Thin film VO_2 submillimeter wave modulators and polarizers," *Applied Physics Letters*, vol. 31, no. 1, pp. 11–13, 1977.

[4] A. Rúa, F. E. Fernández, and N. Sepúlveda, "Bending in VO_2-coated microcantilevers suitable for thermally activated actuators," *Journal of Applied Physics*, vol. 107, no. 7, pp. 074506–1–074506–4, 2010.

[5] R. Cabrera, E. Merced, and N. Sepúlveda, "A micro-electro-mechanical memory based on the structural phase transition of VO_2," *Physica Status Solidi (A)*, vol. 210, no. 9, pp. 1704–1711, 2013.

[6] M. A. Richardson and J. A. Coath, "Infrared optical modulators for missile testing," *Optics and Laser Technology*, vol. 30, no. 2, pp. 137–140, 1998.

[7] M. Soltani, M. Chaker, E. Haddad, R. Kruzelecky, J. Margot, P. Laou, and S. Paradis, "Fabrication of stationary micro-optical shutter based on semiconductor-to-metallic phase transition of w-doped VO_2 active layer driven by an external voltage," *Journal of Vacuum Science & Technology A*, vol. 26, no. 4, pp. 763–767, 2008.

[8] H. Kakiuchida, P. Jin, S. Nakao, and M. Tazawa, "Optical properties of vanadium dioxide film during semiconductiveâĂŞmetallic phase transition," *Japanese Journal of Applied Physics*, vol. 46, no. 5, pp. 113–116, 2007.

[9] J. Barker, A. S., H. W. Verleur, and H. J. Guggenheim, "Infrared optical properties of vanadium dioxide above and below the transition temperature," *Physical Review Letters*, vol. 17, no. 26, pp. 1286–1289, 1966.

[10] M. Seo, J. Kyoung, H. Park, S. Koo, H.-s. Kim, H. Bernien, B. J. Kim, J. H. Choe, Y. H. Ahn, H.-T. Kim, N. Park, Q.-H. Park, K. Ahn, and D.-s. Kim, "Active terahertz nanoantennas based on VO_2 phase transition," *Nano Letters*, vol. 10, no. 6, pp. 2064–2068, 2010.

[11] K. A. Khan and C. G. Granqvist, "Thermochromic sputter-deposited vanadium oxyfluoride coatings with low luminous absorptance," *Applied Physics Letters*, vol. 55, no. 1, pp. 4–6, 1989.

[12] R. G. Driggers, K. J. Barnard, E. Burroughs, Jr., R. G. Deep, and O. M. Williams, "Review of infrared scene projector technology-1993," *Optical Engineering*, vol. 33, no. 7, pp. 2408–2417, 1994.

[13] M. B. Prince, "Silicon solar energy converters," *Journal of Applied Physics*, vol. 26, no. 5, pp. 534–540, 1955.

[14] H. Holloway, "Unconventional thin film ivâĂŞvi photodiode structures," *Thin Solid Films*, vol. 58, no. 1, pp. 73 – 78, 1979.

[15] R. Korde and J. Geist, "Quantum efficiency stability of silicon photodiodes," *Applied Optics*, vol. 26, pp. 5284–5290, Dec 1987.

[16] A. J. Steckl, R. D. Nelson, B. French, R. Gudmundsen, and D. Schechter, "Application of charge-coupled devices to infrared detection and imaging," *Proceedings of the IEEE*, vol. 63, no. 1, pp. 67–74, 1975.

[17] R. Johnson, D. Bitzer, and H. Slottow, "The device characteristics of the plasma display element," *Electron Devices, IEEE Transactions on*, vol. 18, pp. 642–649, Sep 1971.

[18] Y. Oana, "Technical developments and trends in a-si tft-lcds," *Journal of Non-Crystalline Solids*, vol. 115, no. 1âĂŞ3, pp. 27–32, 1989.

[19] G. F. Weston, "Plasma panel displays," *Journal of Physics E: Scientific Instruments*, vol. 8, no. 12, pp. 981–991, 1975.

[20] O. M. Williams, "Dynamic infrared scene projection: a review," *Infrared Physics and Technology*, vol. 39, no. 7, pp. 473 – 486, 1998.

[21] V. T. Bly, "Passive visible to infrared transducer for dynamic infrared image simulation," *Optical Engineering*, vol. 21, no. 6, pp. 216079–1–216079–9, 1982.

[22] V. K. Malyutenko, O. Y. Malyutenko, V. Leonov, and C. Van Hoof, "Micromachined single-level nonplanar polycrystalline sige thermal microemitters for infrared dynamic scene projection," *Applied Physics Letters*, vol. 94, no. 21, pp. 213514–1–213514–3, 2009.

[23] *IR Image Generation By Thermoelectric Elements*, vol. 0765, 1987.

[24] J. James, J. LaVeigne, J. Oleson, G. Matis, J. Lannon, S. Goodwin, A. Huffman, S. Solomon, and P. Bryant, "Oasis: cryogenically optimized resistive arrays and irsp subsystems for space-background ir simulation," in *Technologies for Synthetic Environments: Hardware-in-the-Loop Testing XII*, vol. 6544, pp. 654405–1–654405–10, 2007.

[25] D. B. Beasley, M. W. Bender, J. Crosby, T. Messer, and D. A. Saylor, "Dynamic ir scene projector based upon the digital micromirror device," in *Dynamic IR scene projector based upon the digital micromirror device*, vol. 4366, pp. 96–102, 2001.

[26] R. A. Forber, A. Au, U. Efron, K. Sayyah, S.-T. Wu, and G. C. Goldsmith II, "Dynamic ir scene projection using the hughes liquid crystal light valve," in *Liquid Crystal Materials, Devices, and Applications*, vol. 1665, pp. 259–273, 1992.

[27] V. Malyutenko, V. Bogatyrenko, and O. Malyutenko, "Bulk silicon as photonic dynamic infrared scene projector," *Applied Physics Letters*, vol. 102, pp. 131109–1–131109–3, Apr 2013.

[28] S. Solomon, M. Hawkins, and N. Mastronardi, "Plasma display technology for scene projector application," in *Technologies for Synthetic Environments: Hardware-in-the-Loop Testing X*, vol. 5785, pp. 24–35, 2005.

[29] T. N. Horsky, C. M. Schiller, G. J. Genetti, D. M. O'Mara, W. S. Hamnett, and C. Warde, "Electron-beam-addressed membrane light modulator for ir scene projection," in *Infrared Technology XVII*, vol. 1540, pp. 527–532, 1991.

[30] V. K. Malyutenko, V. V. Bogatyrenko, and O. Y. Malyutenko, "Radiative cooling of bulk si by optical down-conversion," *Journal of Applied Physics*, vol. 108, no. 7, pp. 073104–1–073104–4, 2010.

[31] H. Jiang, Y. K. Zou, Q. Chen, K. K. Li, R. Zhang, Y. Wang, H. Ming, and Z. Zheng, "Transparent electro-optic ceramics and devices," vol. 5644, pp. 380–394, 2005.

[32] H. Cai, X. M. Zhang, C. Lu, A. Q. Liu, and E. H. Khoo, "Linear MEMS variable optical attenuator using reflective elliptical mirror," *IEEE Photonics Technology Letters*, vol. 17, no. 2, pp. 402–404, 2005.

[33] C. H. Kim and Y. K. Kim, "MEMS variable optical attenuator using a translation motion of 45 degrees tilted vertical mirror," *Journal of Micromechanics and Microengineering*, vol. 15, no. 8, pp. 1466–1475, 2005.

[34] C. Lee, "Arrayed variable optical attenuator using retro-reflective MEMS mirrors," *IEEE Photonics Technology Letters*, vol. 17, no. 12, pp. 2640–2642, 2005.

[35] L. Zhu, Y. Huang, and A. Yariv, "Integrated microfluidic variable optical attenuator," *Optics Express*, vol. 13, no. 24, pp. 9916–9921, 2005.

[36] M. I. Lapsley, S. C. S. Lin, X. L. Mao, and T. J. Huang, "An in-plane, variable optical attenuator using a fluid-based tunable reflective interface," *Applied Physics Letters*, vol. 95, no. 8, pp. 083507–1–083507–3, 2009.

[37] A. Duduś, R. Blue, and D. Uttamchandani, "Miniaturized ferrofluid actuated single mode fiber variable optical attenuator (voa)," in *Optical MEMS and Nanophotonics (OMN), 2014 International Conference on*, pp. 123–124, Aug 2014.

[38] C. Lee, F. L. Hsiao, T. Kobayashi, K. H. Koh, P. V. Ramana, W. F. Xiang, B. Yang, C. W. Tan, and D. Pinjala, "A 1-V operated MEMS variable optical attenuator using piezoelectric PZT thin-film actuators," *IEEE Journal of Selected Topics in Quantum Electronics*, vol. 15, no. 5, pp. 1529–1536, 2009.

[39] J. P. Guo, J. H. Zhu, W. Zhou, and X. G. Huang, "A plasmonic electro-optical variable optical attenuator based on side-coupled metal-dielectric-metal structure," *Optics Communications*, vol. 294, pp. 405–408, 2013.

[40] K. Leosson, T. Rosenzveig, P. G. Hermannsson, and A. Boltasseva, "Compact plasmonic variable optical attenuator," *Optics Express*, vol. 16, no. 20, pp. 15546–15552, 2008.

[41] D. C. Zografopoulos and R. Beccherelli, "Plasmonic variable optical attenuator based on liquid-crystal tunable stripe waveguides," *Plasmonics*, vol. 8, no. 2, pp. 599–604, 2013.

[42] G. Zhu, B. yan Wei, L. yu Shi, X. wen Lin, W. Hu, Z. di Huang, and Y. qing Lu, "A fast response variable optical attenuator based on blue phase liquid crystal," *Optical Express*, vol. 21, pp. 5332–5337, Mar 2013.

[43] J. L. Benítez and D. Mendoza, "Modulation of the optical transmittance in multilayer graphene by an electrical signal," *Applied Physics Letters*, vol. 103, no. 8, pp. 083116–1–083116–4, 2013.

[44] C. Chen, C. Lee, and Y.-J. Lai, "Novel voa using in-plane reflective micromirror and off-axis light attenuation," *Communications Magazine, IEEE*, vol. 41, pp. 16–20, Aug 2003.

[45] C. Giles, V. Aksyuk, B. Barber, R. Ruel, L. Stulz, and D. Bishop, "A silicon mems optical switch attenuator and its use in lightwave subsystems," *Selected Topics in Quantum Electronics, IEEE Journal of*, vol. 5, pp. 18–25, Jan 1999.

[46] S. A. Reza and N. A. Riza, "A liquid lens-based broadband variable fiber optical attenuator," *Optics Communications*, vol. 282, no. 7, pp. 1298–1303, 2009.

[47] F. Mugele and J.-C. Baret, "Electrowetting: from basics to applications," *Journal of Physics: Condensed Matter*, vol. 17, no. 28, pp. R705–R774, 2005.

[48] A. J. Chung and D. Erickson, "Optofluidic waveguides for reconfigurable photonic systems," *Optics Express*, vol. 19, pp. 8602–8609, Apr 2011.

[49] S. de Pedro, V. Cadarso, X. MuÃśoz-Berbel, J. Plaza, J. Sort, J. Brugger, S. BÃijttgenbach, and A. Llobera, "Pdms-based, magnetically actuated variable optical attenuators obtained by soft lithography and inkjet printing technologies," *Sensors and Actuators A: Physical*, vol. 215, no. 0, pp. 30–35, 2014.

[50] Z. Y. Wang, J. Zhang, X. Wu, M. Birau, G. Yu, H. Yu, Y. Qi, P. Desjardins, X. Meng, J. P. Gao, E. Todd, N. Song, Y. Bai, A. M. R. Beaudin, and G. LeClair, "Near-infrared absorbing materials," *Pure and Applied Chemistry*, vol. 76, no. 7-8, pp. 1435–1443, 2004.

[51] I. Schwendeman, J. Hwang, D. M. Welsh, D. B. Tanner, and J. R. Reynolds, "Combined visible and infrared electrochromism using dual polymer devices," *Advanced Materials*, vol. 13, no. 9, pp. 634–637, 2001.

[52] A. Dyer, C. Grenier, and J. Reynolds, "A poly(3,4-alkylenedioxythiophene) electrochromic variable optical attenuator with near-infrared reflectivity tuned independently of the visible region," *Advanced Functional Materials*, vol. 17, no. 9, pp. 1480–1486, 2007.

[53] J. Zheng, Y.-j. Zheng, and X.-h. Wan, "Near infrared electrochromic variable optical attenuator fabricated by layer-by-layer assembly," *Chinese Journal of Polymer Science*, vol. 29, no. 1, pp. 117–123, 2011.

[54] A. M. McDonagh, S. R. Bayly, D. J. Riley, M. D. Ward, J. A. McCleverty, M. A. Cowin, C. N. Morgan, R. Varrazza, R. V. Penty, and I. H. White, "A variable optical attenuator operating in the near-infrared region based on an electrochromic molybdenum complex," *Chemistry of Materials*, vol. 12, no. 9, pp. 2523–2524, 2000.

[55] A. Duduś, R. Blue, M. Zagnoni, G. Stewart, and D. Uttamchandani, "In-line single-mode fiber variable optical attenuator based on electrically addressable microdroplets," *Applied Physics Letters*, vol. 105, no. 2, pp. 021105–1–021105–4, 2014.

[56] R. R. A. Syms, H. Zou, J. Stagg, and H. Veladi, "Sliding-blade mems iris and variable optical attenuator," *Journal of Micromechanics and Microengineering*, vol. 14, no. 12, pp. 1700–1710, 2004.

[57] C.-H. Li, H.-T. Hsieh, and G.-D. Su, "A fiber variable optical attenuator made by a large-stroke polymeric deformable mirror," *Photonics Technology Letters, IEEE*, vol. 21, pp. 1432–1434, Oct 2009.

[58] K. Isamoto, K. Kato, A. Morosawa, C. Chong, H. Fujita, and H. Toshiyoshi, "A 5-v operated mems variable optical attenuator by soi bulk micromachining," *Selected Topics in Quantum Electronics, IEEE Journal of*, vol. 10, pp. 570–578, May 2004.

[59] E. Nicolescu, C. Mao, A. Fardad, and M. Escuti, "Polarization-insensitive variable optical attenuator and wavelength blocker using liquid crystal polarization gratings," *Lightwave Technology, Journal of*, vol. 28, pp. 3121–3127, Nov 2010.

[60] B. Borovic, A. Q. Liu, D. Popa, H. Cai, and F. L. Lewis, "Light-intensity-feedback-waveform generator based on MEMS variable optical attenuator," *IEEE Transactions on Industrial Electronics*, vol. 55, no. 1, pp. 417–426, 2008.

[61] S. Li, X. Jin, X. Zhang, and Y. K. Zou, "Digitally controlled programmable high-speed variable optical attenuator," *Microwave and Optical Technology Letters*, vol. 48, no. 6, pp. 1019–1021, 2006.

[62] R. Cao, K.-S. Low, A. Liu, and C. Hong, "A mems based variable optical attenuator," in *Industrial Electronics Society, 2004. IECON 2004. 30th Annual Conference of IEEE*, vol. 2, pp. 1945–1950, Nov 2004.

[63] P. Winzer and R. Essiambre, "Advanced optical modulation formats," *Proceedings of the IEEE*, vol. 94, pp. 952–985, May 2006.

[64] C. Chen, X. Niu, C. Han, Z. Shi, X. Wang, X. Sun, F. Wang, Z. Cui, and D. Zhang, "Monolithic multi-functional integration of roadm modules based on polymer photonic lightwave circuit," *Optics Express*, vol. 22, pp. 10716–10727, May 2014.

[65] Y.-T. Han, J.-U. Shin, S.-H. Park, S.-P. Han, Y. Baek, C.-H. Lee, Y.-O. Noh, H.-J. Lee, and H.-H. Park, "Fabrication of 10-channel polymer thermo-optic digital optical switch array," *Photonics Technology Letters, IEEE*, vol. 21, pp. 1556–1558, Oct 2009.

[66] A. V. Tran, W. D. Zhong, R. Tucker, and K. Song, "Reconfigurable multichannel optical add-drop multiplexers incorporating eight-port optical circulators and fiber bragg gratings," *Photonics Technology Letters, IEEE*, vol. 13, pp. 1100–1102, Oct 2001.

[67] Q. Fang, J. Song, G. Zhang, M. Yu, Y. Liu, G.-Q. Lo, and D.-L. Kwong, "Monolithic integration of a multiplexer/demultiplexer with a thermo-optic voa array on an soi platform," *Photonics Technology Letters, IEEE*, vol. 21, pp. 319–321, March 2009.

[68] M. Kang, S. Kim, J. Ryu, and T. Noh, "Optical properties for the mott transition in VO_2," *AIP Advances*, vol. 2, pp. 012168–1–012168–6, March 2012.

[69] A. Rúa, F. E. Fernández, and N. Sepúlveda, "Bending in VO_2-coated microcantilevers suitable for thermally activated actuators," *Journal of Applied Physics*, vol. 107, no. 7, pp. 074506–1–074506–4, 2010.

[70] A. L. Pergament, G. B. Stefanovich, N. A. Kuldin, and A. A. Velichko, "On the problem of metal-insulator transitions in vanadium oxides," *ISRN Condensed Matter Physics*, vol. 2013, p. 6, 2013.

[71] K. Kosuge, "The phase diagram and phase transition of the V_2O_3-V_2O_5, system," *Journal of Physics and Chemistry of Solids*, vol. 28, no. 8, pp. 1613–1621, 1967.

[72] W. Burkhardt, T. Christmann, B. Meyer, W. Niessner, D. Schalch, and A. Scharmann, "W- and F-doped VO_2 films studied by photoelectron spectrometry," *Thin Solid Films*, vol. 345, no. 2, pp. 229–235, 1999.

[73] S. Kabashima, T. Goto, K. Nishimura, and T. Kawakubo, "Impurity conduction in Ti-doped VO_2 studied by microwave frequency conductivity," *Journal of the Physical Society of Japan*, vol. 32, no. 1, pp. 158–163, 1972.

[74] M. Marezio, D. B. McWhan, J. P. Remeika, and P. D. Dernier, "Structural aspects of the metal-insulator transitions in Cr-doped VO_2," *Physical Review B*, vol. 5, pp. 2541–2551, 1972.

[75] T. Phillips, R. Murphy, and T. Poehler, "Electrical studies of reactively sputtered Fe-doped VO_2 thin films," *Materials Research Bulletin*, vol. 22, no. 8, pp. 1113–1123, 1987.

[76] J. Laverock, A. R. H. Preston, D. Newby, K. E. Smith, S. Sallis, L. F. J. Piper, S. Kittiwatanakul, J. W. Lu, S. A. Wolf, M. Leandersson, and T. Balasubramanian, "Photoemission evidence for crossover from Peierls-like to Mott-like transition in highly strained VO_2," *Physical Review B*, vol. 86, pp. 195124–1–195124–5, 2012.

[77] S. Biermann, A. Poteryaev, A. I. Lichtenstein, and A. Georges, "Dynamical singlets and correlation-assisted Peierls transition in VO_2," *Physical Review Letters*, vol. 94, no. 2, pp. 026404–1–026404–4, 2005.

[78] R. M. Wentzcovitch, W. W. Schulz, and P. B. Allen, "VO_2 - Peierls or Mott-Hubbard - a view from band theory," *Physical Review Letters*, vol. 72, no. 21, pp. 3389–3392, 1994.

[79] H. T. Kim, B. J. Kim, Y. W. Lee, B. G. Chae, and S. J. Yun, "Switching of the mott transition based on hole-driven MIT theory," *Physica B-Condensed Matter*, vol. 403, no. 5-9, pp. 1434–1436, 2008.

[80] A. Pergament, "Metal-insulator transition: the Mott criterion and coherence length," *Journal of Physics-Condensed Matter*, vol. 15, no. 19, pp. 3217–3223, 2003.

[81] A. Cavalleri, T. Dekorsy, H. H. W. Chong, J. C. Kieffer, and R. W. Schoenlein, "Evidence for a structurally-driven insulator-to-metal transition in VO_2: A view from the ultrafast timescale," *Physical Review B*, vol. 70, no. 16, pp. 161102–1–161102–4, 2004.

[82] A. Cavalleri, C. Toth, C. W. Siders, J. A. Squier, F. Raksi, P. Forget, and J. C. Kieffer, "Femtosecond structural dynamics in VO_2 during an ultrafast solid-solid phase transition," *Physical Review Letters*, vol. 87, no. 23, pp. 237401–1–237401–4, 2001.

[83] Y. Zhou, X. Chen, C. Ko, Z. Yang, C. Mouli, and S. Ramanathan, "Voltage-triggered ultrafast phase transition in vanadium dioxide switches," *Electron Device Letters, IEEE*, vol. 34, pp. 220–222, Feb 2013.

[84] V. Eyert, "The metal-insulator transitions of VO_2: A band theoretical approach," *Annalen der Physik*, vol. 11, no. 9, pp. 650–704, 2002.

[85] J. B. Goodenough, "The two components of the crystallographic transition in VO_2," *Journal of Solid State Chemistry*, vol. 3, no. 4, pp. 490–500, 1971.

[86] C. N. R. Rao, "Transition metal oxides," *Annual Review of Physical Chemistry*, vol. 40, no. 1, pp. 291–326, 1989.

[87] N. B. Aetukuri, A. X. Gray, M. Drouard, M. Cossale, L. Gao, A. H. Reid, R. Kukreja, H. Ohldag, C. A. Jenkins, E. Arenholz, K. P. Roche, H. A. Durr, M. G. Samant, and S. S. P. Parkin, "Control of the metal-insulator transition in vanadium dioxide by modifying orbital occupancy," *Nature Physics*, vol. 9, pp. 661–666, 2013.

[88] A. Cavalleri, M. Rini, H. H. W. Chong, S. Fourmaux, T. E. Glover, P. A. Heimann, J. C. Kieffer, and R. W. Schoenlein, "Band-selective measurements of electron dynamics in VO_2 using femtosecond near-edge x-ray absorption," *Physical Review Letters*, vol. 95, pp. 067405–1–067405–4, Aug 2005.

[89] S. Kumar, M. D. Pickett, J. P. Strachan, G. Gibson, Y. Nishi, and R. S. Williams, "Local temperature redistribution and structural transition during joule-heating-driven conductance switching in VO_2," *Advanced Materials*, vol. 25, no. 42, pp. 6128–6132, 2013.

[90] S. Bonora, U. Bortolozzo, S. Residori, R. Balu, and P. V. Ashrit, "Mid-ir to near-ir image conversion by thermally induced optical switching in vanadium dioxide," *Optics Letters*, vol. 35, no. 2, pp. 103–105, 2010.

[91] H. Coy, R. Cabrera, N. Sepulveda, and F. E. Fernandez, "Optoelectronic and all-optical multiple memory states in vanadium dioxide," *Journal of Applied Physics*, vol. 108, no. 11, pp. 113115–1–113115–6, 2010.

[92] H. Obloh, W. Muller-Sebert, D. Brink, W. Fehrenbach, C. Nebel, C. Wild, and E. Worner, "Matrix-addressable infrared filters for the protection of highly sensitive detectors," in *Defense Science Research Conference and Expo (DSR), 2011*, pp. 1–5, 2011.

[93] L. d'Auria, J. P. Huignard, C. Slezak, and E. Spitz, "Experimental holographic read-write memory using 3-d storage," *Applied Optics*, vol. 13, pp. 808–818, Apr 1974.

[94] T. D. Rossing, "The compact disc digital audio system," *The Physics Teacher*, vol. 25, no. 9, pp. 556–563, 1987.

[95] J. A. Cope, "The physics of the compact disc," *Physics Education*, vol. 28, no. 1, p. 15, 1993.

[96] A. S. Matharu, S. Jeeva, and P. S. Ramanujam, "Liquid crystals for holographic optical data storage," *Chemistry Society Review*, vol. 36, pp. 1868–1880, 2007.

[97] D. Day, M. Gu, and A. Smallridge, "Review of optical data storage," in *Infrared Holography for Optical Communications* (P. Boffi, D. Piccinin, and M. Ubaldi, eds.), vol. 86 of *Topics in Applied Physics*, pp. 1–22, Springer Berlin Heidelberg, 2003.

[98] E. Glezer, M. Milosavljevic, L. Huang, R. Finlay, T.-H. Her, J. Callan, and E. Mazur, "3-d optical storage and engraving inside transparent materials," in *Ultrafast Phenomena X* (P. Barbara, J. Fujimoto, W. Knox, and W. Zinth, eds.), vol. 62 of *Springer Series in Chemical Physics*, pp. 157–158, Springer Berlin Heidelberg, 1996.

[99] B. S. Ham, "Ultralong quantum optical data storage using an optical locking technique," *Nature Photonics*, vol. 3, no. 7090, pp. 518–522, 2009.

[100] Y. Yokoyama, "Fulgides for memories and switches," *Chemical Reviews*, vol. 100, no. 5, pp. 1717–1740, 2000.

[101] V. G. Kravets, "Using electron trapping materials for optical memory," *Optical Materials*, vol. 16, no. 3, pp. 369–375, 2001.

[102] S. Kozyukhin, A. Sherchenkov, V. Novotortsev, and S. Timoshenkov, "Phase-change-memory materials based on system chalcogenides and their application in phase-change random-access memory," *Nanotechnologies in Russia*, vol. 6, no. 3-4, pp. 227–236, 2011.

[103] N. Yamada, R. Kojima, K. Hisada, T. Mihara, A. Tsuchino, N. Fujinoki, M. Birukawa, T. Matsunaga, N. Yasuda, Y. Fukuyama, K. Ito, Y. Tanaka, S. Kimura, and M. Takata, "Phase-change nanodot material for an optical memory," *Advanced Optical Materials*, vol. 1, no. 11, pp. 820–826, 2013.

[104] N. C. Cédric Clévy, Micky Rakotondrabe, *Signal Measurement and Estimation Techniques for Micro and Nanotechnology*. Springer Science & Business Media, 2011.

[105] J. Ouyang and Y. Zhu, "Z-shaped mems thermal actuators: Piezoresistive self-sensing and preliminary results for feedback control," *Microelectromechanical Systems, Journal of*, vol. 21, pp. 596–604, June 2012.

[106] C. K. Pang, G. Guo, B. Chen, and T. H. Lee, "Self-sensing actuation for nanopositioning and active-mode damping in dual-stage hdds," *Mechatronics, IEEE/ASME Transactions on*, vol. 11, pp. 328–338, June 2006.

[107] A. Punning, M. Kruusmaa, and A. Aabloo, "A self-sensing ion conducting polymer metal composite (ipmc) actuator," *Sensors and Actuators A: Physical*, vol. 136, no. 2, pp. 656 – 664, 2007.

[108] C.-C. Lan, C.-M. Lin, and C.-H. Fan, "A self-sensing microgripper module with wide handling ranges," *Mechatronics, IEEE/ASME Transactions on*, vol. 16, pp. 141–150, Feb 2011.

[109] N. Ma, G. Song, and H.-J. Lee, "Position control of shape memory alloy actuators with internal electrical resistance feedback using neural networks," *Smart Materials and Structures*, vol. 13, no. 4, p. 777, 2004.

[110] E. Merced, J. Zhang, X. Tan, and N. Sepulveda, "Robust control of VO_2-coated microbenders using self-sensing feedback," *Mechatronics, IEEE/ASME Transactions on*, vol. 19, pp. 1583–1592, Oct 2014.

[111] E. Merced, D. Torres, X. Tan, and N. Sepulveda, "An electrothermally actuated VO_2-based mems using self-sensing feedback control," *Microelectromechanical Systems, Journal of*, vol. 24, pp. 100–107, Feb 2015.

[112] Z. Yang, C. Ko, and S. Ramanathan, "Oxide electronics utilizing ultrafast metal-insulator transitions," *Annual Review of Materials Research*, vol. 41, no. 1, pp. 337–367, 2011.

[113] R. E. Marvel, R. R. Harl, V. Craciun, B. R. Rogers, and R. F. H. Jr., "Influence of deposition process and substrate on the phase transition of vanadium dioxide thin films," *Acta Materialia*, vol. 91, no. 0, pp. 217–226, 2015.

[114] P. Boriskov, A. Velichko, A. Pergament, G. Stefanovich, and D. Stefanovich, "The effect of electric field on metal-insulator phase transition in vanadium dioxide," *Technical Physics Letters*, vol. 28, no. 5, pp. 406–408, 2002.

[115] Z. Yang, C. Ko, and S. Ramanathan, "Metal-insulator transition characteristics of VO_2 thin films grown on ge(100) single crystals," *Journal of Applied Physics*, vol. 108, no. 7, pp. 073708–1–073708–6, 2010.

[116] G. Golan, A. Axelevitch, B. Sigalov, and B. Gorenstein, "MetalâĂŞinsulator phase transition in vanadium oxides films," *Microelectronics Journal*, vol. 34, no. 4, pp. 255–258, 2003.

[117] G. Beydaghyan, V. Basque, and P. Ashrit, "High contrast thermochromic switching in vanadium dioxide VO_2 thin films deposited on indium tin oxide substrates," *Thin Solid Films*, vol. 522, pp. 204–207, 2012.

[118] J. Nag and R. F. H. Jr, "Synthesis of vanadium dioxide thin films and nanoparticles," *Journal of Physics: Condensed Matter*, vol. 20, no. 26, pp. 264016–1–264016–14, 2008.

[119] L. A. Ryabova, I. A. Serbinov, and A. S. Darevsky, "Preparation and properties of pyrolysis of vanadium oxide films," *Journal of The Electrochemical Society*, vol. 119, no. 4, pp. 427–429, 1972.

[120] T. D. Manning and I. P. Parkin, "Atmospheric pressure chemical vapour deposition of tungsten doped vanadium(iv) oxide from $vocl_3$, water and wcl_6," *Journal of Materials Chemistry*, vol. 14, pp. 2554–2559, 2004.

[121] M. Tangirala, K. Zhang, D. Nminibapiel, V. Pallem, C. Dussarrat, W. Cao, T. N. Adam, C. S. Johnson, H. E. Elsayed-Ali, and H. Baumgart, "Physical analysis of VO_2 films grown by atomic layer deposition and rf magnetron sputtering," *ECS Journal of Solid State Science and Technology*, vol. 3, no. 6, pp. 89–94, 2014.

[122] G. Rampelberg, M. Schaekers, K. Martens, Q. Xie, D. Deduytsche, B. De Schutter, N. Blasco, J. Kittl, and C. Detavernier, "Semiconductor-metal transition in thin VO_2 films grown by ozone based atomic layer deposition," *Applied Physics Letters*, vol. 98, no. 16, pp. 162902–1–162902–3, 2011.

[123] P. Dagur, A. U. Mane, and S. Shivashankar, "Thin films of VO_2 on glass by atomic layer deposition: microstructure and electrical properties," *Journal of Crystal Growth*, vol. 275, no. 1âĂŞ2, pp. e1223–e1228, 2005. Proceedings of the 14th International Conference on Crystal Growth and the 12th International Conference on Vapor Growth and Epitaxy.

[124] S. Chen, J. Lai, J. Dai, H. Ma, H. Wang, and X. Yi, "Characterization of nanostructured VO_2 thin films grown by magnetron controlled sputtering deposition and post annealing method," *Optical Express*, vol. 17, pp. 24153–24161, Dec 2009.

[125] D. Ruzmetov, K. T. Zawilski, V. Narayanamurti, and S. Ramanathan, "Structure-functional property relationships in rf-sputtered vanadium dioxide thin films," *Journal of Applied Physics*, vol. 102, no. 11, pp. 113715–1–113715–7, 2007.

[126] F. C. Case, "Influence of ion beam parameters on the electrical and optical properties of ionâĂŘassisted reactively evaporated vanadium dioxide thin films," *Journal of Vacuum Science & Technology A*, vol. 5, no. 4, pp. 1762–1766, 1987.

[127] G. Golan, A. Axelevitch, B. Sigalov, and B. Gorenstein, "Investigation of phase transition mechanism in vanadium oxide thin films," *Journal of Optoelectronics Advanced Materials*, vol. 6, no. 1, pp. 189–195, 2004.

[128] D. Vinichenko, V. Zlomanov, V. VasilâĂŹev, D. Seregin, and O. Berezina, "Synthesis of vanadium dioxide films by a modified sol-gel process," *Inorganic Materials*, vol. 47, no. 3, pp. 279–284, 2011. triethoxyvanadyl.

[129] M. Pan, H. Zhong, S. Wang, J. Liu, Z. Li, X. Chen, and W. Lu, "Properties of VO_2 thin film prepared with precursor $VO(acac)_2$," *Journal of Crystal Growth*, vol. 265, no. 1âĂŞ2, pp. 121–126, 2004.

[130] D. P. Partlow, S. R. Gurkovich, K. C. Radford, and L. J. Denes, "Switchable vanadium oxide films by a solâĂŘgel process," *Journal of Applied Physics*, vol. 70, no. 1, pp. 443–452, 1991.

[131] Y. Dachuan, X. Niankan, Z. Jingyu, and Z. Xiulin, "Vanadium dioxide films with good electrical switching property," *Journal of Physics D: Applied Physics*, vol. 29, no. 4, pp. 1051–1057, 1996. V2O5 powder.

[132] I. Takahashi, M. Hibino, and T. Kudo, "Thermochromic properties of double-doped VO_2 thin films prepared by a wet coating method using polyvanadate-based sols containing w and mo or w and ti," *Japanese Journal of Applied Physics*, vol. 40, no. 3R, pp. 1391–1395, 2001. V-powder and H2O2.

[133] J. Livage, G. Guzman, F. Beteille, and P. Davidson, "Optical properties of sol-gel derived vanadium oxide films," *Journal of Sol-Gel Science and Technology*, vol. 8, no. 1-3, pp. 857–865, 1997.

[134] G. Guzman, R. Morineau, and J. Livage, "Synthesis of vanadium dioxide thin films from vanadium alkoxides," *Materials Research Bulletin*, vol. 29, no. 5, pp. 509 – 515, 1994.

[135] K. Speck, H.-W. Hu, M. Sherwin, and R. Potember, "Vanadium dioxide films grown from vanadium tetra-isopropoxide by the sol-gel process," *Thin Solid Films*, vol. 165, no. 1, pp. 317–322, 1988. They started with VCL4.

[136] S. Attia, J. Wang, G. Wu, J. Shen, and J. Ma, "Review on sol-gel derived coatings: Process, techniques and optical applications," *Journal of Materials Sciences and Technology*, vol. 18, no. 03, pp. 211–218, 2002.

[137] Q. Shi, W. Huang, J. Yan, Y. Zhang, M. Mao, Y. Zhang, Y. Xu, and Y. Zhang, "Preparation and phase transition characterization of VO_2 thin film on single crystal si (100) substrate by solâĂŞgel process," *Journal of Sol-Gel Science and Technology*, vol. 59, no. 3, pp. 591–597, 2011.

[138] Y. F. Wu, L. L. Fan, S. M. Chen, S. Chen, C. W. Zou, and Z. Y. Wu, "Spectroscopic analysis of phase constitution of high quality VO_2 thin film prepared by facile sol-gel method," *AIP Advances*, vol. 3, no. 4, pp. 042132–1–042132–10, 2013.

[139] D. H. Kim and H. S. Kwok, "Pulsed laser deposition of VO_2 thin films," *Applied Physics Letters*, vol. 65, no. 25, pp. 3188–3190, 1994.

[140] M. Borek, F. Qian, V. Nagabushnam, and R. K. Singh, "Pulsed laser deposition of oriented VO_2 thin films on râĂŘcut sapphire substrates," *Applied Physics Letters*, vol. 63, no. 24, pp. 3288–3290, 1993.

[141] M. Soltani, M. Chaker, E. Haddad, R. V. Kruzelecky, and D. Nikanpour, "Optical switching of vanadium dioxide thin films deposited by reactive pulsed laser deposition," *Journal of Vacuum Science & Technology A*, vol. 22, no. 3, pp. 859–864, 2004.

[142] M. Maaza, K. Bouziane, J. Maritz, D. McLachlan, R. Swanepool, J. Frigerio, and M. Every, "Direct production of thermochromic VO_2 thin film coatings by pulsed laser ablation," *Optical Materials*, vol. 15, no. 1, pp. 41–45, 2000.

[143] G. J. Fang, Z. L. Liu, Y. Wang, Y. H. Liu, and K. L. Yao, "Synthesis and structural, electrochromic characterization of pulsed laser deposited vanadium oxide thin films," *Journal of Vacuum Science & Technology A*, vol. 19, no. 3, pp. 887–892, 2001. deposition 100-400 degC.

[144] N. Dávila, R. Cabrera, and N. Sepúlveda, "Programming and projection of near IR images using VO_2 films," *IEEE Photonics Technology Letters*, vol. 24, no. 20, pp. 1830–1833, 2012.

[145] M. Tazawa, P. Jin, and S. Tanemura, "Optical constants of $V_{1-x}W_xO_2$ films," *Applied Optics*, vol. 37, no. 10, pp. 1858–1861, 1998.

[146] M. A. Kats, R. Blanchard, S. Zhang, P. Genevet, C. Ko, S. Ramanathan, and F. Capasso, "Vanadium dioxide as a natural disordered metamaterial: Perfect thermal emission and large broadband negative differential thermal emittance," *Physical Review X*, vol. 3, pp. 041004–1–041004–7, Oct 2013.

[147] L. Schares, X. Zhang, R. Wagle, D. Rajan, P. Selo, S. Chang, J. Giles, K. Hildrum, D. Kuchta, J. Wolf, and E. Schenfeld, "A reconfigurable interconnect fabric with optical circuit switch and software optimizer for stream computing systems," in *Optical Fiber Communication - incudes post deadline papers, 2009. OFC 2009. Conference on*, pp. 1–3, March 2009.

[148] T. Son, K. Zongo, C. Ba, G. Beydaghyan, and A. HachÃľ, "Pure optical phase control with vanadium dioxide thin films," *Optics Communications*, vol. 320, no. 0, pp. 151–155, 2014.

[149] S.-H. Lee, H. M. Cheong, M. J. Seong, P. Liu, C. Tracy, A. Mascarenhas, J. Pitts, and S. K. Deb, "Raman spectroscopic studies of amorphous vanadium oxide thin films," *Solid State Ionics*, vol. 165, no. 1âĂŞ4, pp. 111 – 116, 2003. Fifth International Meeting on Electrochromism.